Performance Characterization of a Low Power Magnetic Nozzle

by

Timothy A. Collard

A dissertation submitted in partial fulfillment
of the requirements for the degree of
Doctor of Philosophy
(Aerospace Engineering)
in The University of Michigan
2019

Doctoral Committee:

Professor Alec D. Gallimore, Co-Chair
Assistant Professor Benjamin A. Jorns, Co-Chair
Professor John E. Foster
Professor Mark J. Kushner
Assistant Professor Justin M. Little, University of Washington

Timothy A. Collard
collardt@umich.edu
ORCID iD: 0000 − 0002 − 0723 − 4868

For Amalie and Ben.

Thank you for your love, patience, and support.

ACKNOWLEDGEMENTS

There are a many individuals I would like to acknowledge who have helped me as I have progressed towards completing this milestone. Firstly, I would like to thank my co-advisors Dr. Gallimore and Dr. Jorns. Dr. Gallimore, I am eternally grateful for your continued support through the rotation of advisors under whom I have studied during my tenure at PEPL. Your patience and insightful suggestions as my dissertation has evolved at each transition to a new co-advisor has been invaluable. Dr. Jorns, as the last of my rotating co-advisors, I am grateful for how your perspective has helped shape my work into this final form and for instilling within me a respect for first-principles approaches to research.

My other committee members have also all left an impression on me and this dissertation work. Dr. Foster, thank you for the many impromptu insightful conversations concerning this research. I often walked away from these discussions with new avenues to consider. Likewise, I am grateful for similar conversations with Dr. Kushner, particularly pertaining to RF plasma effects that I had not yet considered, and for efforts at laying the foundation for my plasma-related intuition; I often recalled your classroom lectures when I encountered numbers in my analyses that seemed a bit off. Dr. Little, your work on magnetic nozzles as an electric propulsion option has been a valuable resource throughout, and in many ways acted as a springboard for aspects of my research.

To my former co-advisors, Dr. Longmier and Dr. Sheehan, thank you for providing me with an opportunity to dive into an interesting project with the CubeSat

Ambipolar Thruster and setting me on the path to this milestone. Additionally, I would like to acknowledge Dr. Smith for critiquing my methods and suggesting new research avenues. Our conversations often led to improvements in my experimental setup and data analysis. The experimental work in this dissertation would not have been possible without the help of Eric Viges. Your work on upgrading the Junior Test Facility to include a cryogenic pump enabled this research. Your ability to come up with creative engineering designs for aspects of my experiments, and help me implement them, also made this research possible.

I was fortunate to interact with numerous colleagues during my time at PEPL. To Mike, Frans, Kim, Chris, and Scott thank you for showing me the ropes at the lab and providing me with a working knowledge of electric thrusters, plasma diagnostics, and vacuum technology. Scott, Ethan, Sarah, and Marcel, thank you for soundboarding as I was working through parts of this research and for improving my lab experience by balancing serious research with light-hearted moments. Special thanks to Shad, Ben, and Matt for the help setting up my experiments and for bearing with my extended hours in the lab. To Zach, Josh, Angela, Leanne, and Chris thank for further broadening my exposure to plasma-related applications by sharing your progress on your respective projects with all of us at the lab. Keep up the exciting work.

To the many friends that I have made outside of the lab during my graduate career, thank you for being an integral part of my support network. You have provided invaluable perspective throughout my graduate journey and have always been there, whether I needed someone to share a hobby with or simply listen. I am truly grateful for time that each of you have invested in cultivating our friendship; I am excited to continue growing these friendships as I move into the post-graduate phase of my career. I would not have reached this milestone with my sanity intact without you.

To my family, thank you for being ever-supportive as I pursued my dreams and for always having faith in me. I appreciate all of the sacrifices that you have made and

all of the opportunities that you have afforded me. It is because of the foundation that you have provided that I am have been able to fulfill this dream and begin to foster my career.

Finally, a special acknowledgement for my wife, Amalie. You and I made the bold decision to start dating as I moved to Michigan to start my graduate career. While I entered this graduate program expecting to learn and grow, you have taught me so much more than I could ever learn at the University of Michigan. I cannot adequately express how much your love and support through this entire process has meant to me. Your support has kept me going during the periods of trial and hardship, and celebrating the times of accomplishment with you has made this all worth it. Thank you.

This research is based upon work supported by the National Science Foundation Graduate Research Fellowship Program under Grant No. DGE 1256260.

TABLE OF CONTENTS

LIST OF FIGURES

Figure

LIST OF TABLES

Table

LIST OF ABBREVIATIONS

A_0	Nozzle throat area
A_d	Detachment area
A_e	Nozzle exit area
A_p	Probe collection area
C	Effective exhaust velocity
c	Speed of light
c_s	Bohm speed
g_0	Gravitational acceleration at Earth's surface
e	Charge of an electron
f	Distribution function
I	Probe current
i	State index
I_i	Ion current
I_{plume}	Plume current
I_∞	Probe saturation current
j	Current density
j_{11}	Thick-sheath double probe correction factor
j_{12}	Thick-sheath double probe correction factor
k	Boltzmann constant
K_{exc}	Volumetric excitation rate
K_{iz}	Volumetric ionization rate
ℓ_p	Probe characteristic length
M	Ion Mach number
$\dot{m}$	Propellant mass flow rate
M_e	Propellant Mach number at the nozzle exit plane
m_i	Ion mass
$\dot{m}_{ion}$	Ion mass flow rate
m_g	Neutral gas mass
n_e	Plasma density
$n_{e,0}$	Plasma density at the throat
n_i	Ion density
P_0	Total input power
p_a	Ambient pressure
P_{bw}	Power incident on the back wall

P_c	Power trapped in ion production costs
P_{dep}	Power deposited into the plasma
$\bar{p}_e$	Average electron pressure at the detachment plane
p_e	Pressure at the nozzle exit plane
P_{in}	Input power
P_{jet}	Jet power
P_{noz}	Power entering the nozzle
P_p	Power trapped in electron pressure
P_Q	Power due to electron heat conduction
P_r	Power incident on the radial walls
P_v	Power due to directed ion motion
q	Fundamental charge
r	Radial coordinate
R_s	Source radius
$\vec{s}$	Surface normal vector
S	Linear regression slope
T	Thrust
T_e	Electron temperature
T_e^{est}	Estimated electron temperature
$T_{e,0}$	Electron temperature at the nozzle throat
$T_{e,d}$	Electron temperature at the detachment plane
T_g	Neutral gas temperature
T_i	Ion temperature
$\vec{u}$	Propellant velocity vector
u_0	Axial ion speed at the nozzle throat
u_d	Axial ion speed at the detachment plane
u_e	Axial speed at the nozzle exit
V	Probe potential
V_f^c	Cold probe floating potential
V_f^{em}	Probe floating potential in the high-emission limit
$\vec{v}_{ex}$	Exhaust velocity
v_i	Ion velocity
v_k	Ion velocity projection along the laser path
α	Thick-sheath double probe correction parameter
$\alpha(\nu)$	Doppler-free lineshape
β	Thick-sheath double probe correction parameter
γ	Polytropic cooling index
δ	Sheath factor for the emissive probe
ϵ_0	Vacuum permittivity of free space
ϵ_c	Ion production cost
ϵ_{exc}	Excitation energy
ϵ_{iz}	Ionization energy
η_T	Total efficiency
η_{div}	Divergence efficiency

η_{loss}	Source efficiency
η_m	Mass utilization efficiency
η_{noz}	Nozzle efficiency
η_{rf}	Radiofrequency coupling efficiency
θ_{div}	Divergence angle
λ_D	Debye length
ν	Frequency
ν_L	Laser frequency
ν_t	Transition frequency
ρ	Mass density
ϕ	Plasma potential
Φ	LIF profile
Φ_D	Doppler lineshape
Φ_L	Laser frequency profile
$\Delta\phi_{vc}$	Difference between the floating potential and virtual cathode
χ	Non-dimensional floating potential
ψ	Non-dimensional probe potential

ABSTRACT

The thrust and efficiency performance of a low-power magnetic nozzle test article is analytically and experimentally investigated. In the last two decades the demand for new forms of in-space propulsion for small spacecraft has increased interest in low-power (< 200 W) magnetic nozzle thrusters. The inherent advantages of these devices, including the electrodeless design and the potential to be propellant-agnostic, coupled with the potential to efficiently accelerate the propellant makes low-power magnetic nozzles attractive propulsion options for small satellites. However, the measured performance of both the low and moderate power versions of these thrusters has compared unfavorably to existing state-of-the-art propulsion technologies. A theoretical model was developed to predict low-power magnetic nozzle performance and identify fundamental differences in operation between these devices and their higher power counterparts.

An experiment was designed to inform the theoretical model and to provide insight into the fundamental dynamics of plasma flowing through a low-power magnetic nozzle. This test article consisted of a reconfigurable inductively-coupled plasma source and an electromagnet. A suite of electrostatic probes and laser induced fluorescence is used to measure the plasma properties throughout the nozzle and map the plasma structures present in the plume. Using the experimental measurements, it is found that the plasma expansion follows a polytropic law, as predicted in the literature. The observed increase in the ion velocity confirms that the test article accelerates the propellant. By coupling the experimental results with the theoretical framework, two novel effects that reduce device performance are identified: 1) a low ion fraction,

and corresponding neutral-collisional effects, impedes ion acceleration and shifts the nozzle throat downstream, and 2) non-uniform power deposition enhances the plasma density adjacent to the liner wall, resulting in degraded source (the ratio of power flowing into the diverging nozzle section to the total power deposited in the plasma) and divergence efficiency (the fraction of the kinetic energy in the thrust direction). These effects arise from the low input power and the thruster design parameters. Experimental characterization of a reconfigured test article demonstrates that performance can be recovered by accounting for these two effects when designing the thruster and selecting the operating parameters.

CHAPTER I

Introduction

1.1 Small Satellites

Over the last two decades, small satellites (SmallSats) - technically classed as spacecraft with mass less than 500 kg [1] - have emerged as an alternative to traditional, larger satellite architectures, leading to an acceleration in space technological advances and an increase in in-space activities. This disruptive technology offers several potential advantages: 1) component standardization and modularization to leverage previously developed, commercial-off-the-shelf hardware, 2) economies-of-scale to reduce production costs, 3) shared launch costs by launching as a secondary payload to a traditional, more expensive satellite or by combining the deployment of many SmallSats into a single launch, and 4) less risk adversity, leading to rapid innovation and the incorporation of hardware not specifically designed for the space environment. These advantages combine to reduce mission development times and costs and are making SmallSats increasingly attractive to commercial [2, 3, 4] and scientific [5, 6, 7, 8] entities.

Numerous missions using emerging SmallSat technologies have been proposed by the scientific community, ranging from exploration [9, 10, 11, 12, 13, 14, 15] to remote sensing [16, 17, 18, 19, 20, 21, 22, 23, 24, 25, 26, 27, 28, 29]. Interest in these missions types has increased as the community has realized that revolutionary research that

was previously infeasible due to the required temporal or spatial resolution of the measurements — thus, the number of traditionally expensive satellites [30] required — is becoming possible with 10s of affordable SmallSats [31]. Additionally, the inherent affordability of SmallSats has spurred increased participation by non-traditional actors, including academia, thereby accelerating in-space scientific research [7, 32, 33, 34].

The emergence of SmallSats has coincided with an increasing global economic reliance on space-based infrastructure for everyday activities, including the embedding of on-orbit capabilities into transportation and communications networks [2]. This commercial reliance has prompted several companies, including SpaceX and OneWeb, to propose augmentations of the existing on-orbit capabilities with constellations comprised of hundreds [3] to thousands [4] of SmallSats. In addition to introducing new capabilities, the sheer number of satellites in these proposed constellations also provide redundancy and resiliency to the existing in-space commercial infrastructure — features previously limited by the cost of traditional satellite constellations, but enabled by SmallSat technologies [32]. It is clear from the trends in SmallSat interest and development efforts that SmallSats are poised to become an integral part of the in-space operational paradigm, but technological gaps remain.

1.2 SmallSat Propulsion

While both the scientific and commercial communities have begun to leverage the advantages of SmallSats, many of the proposed mission types require a level of in-space maneuverability — usually quantified by a total velocity increment (ΔV). This maneuverability may stem from the requirement to deploy a constellation from a single launch vehicle, to provide station-keeping or precision pointing, or to satisfy other mission parameters. As each SmallSat mission is unique, this translates to required ΔVs ranging from < 20 m/s [35] to > 1 km/s [11]. The need for maneuvering translates to a direct requirement for some form of on-board propulsion. The type

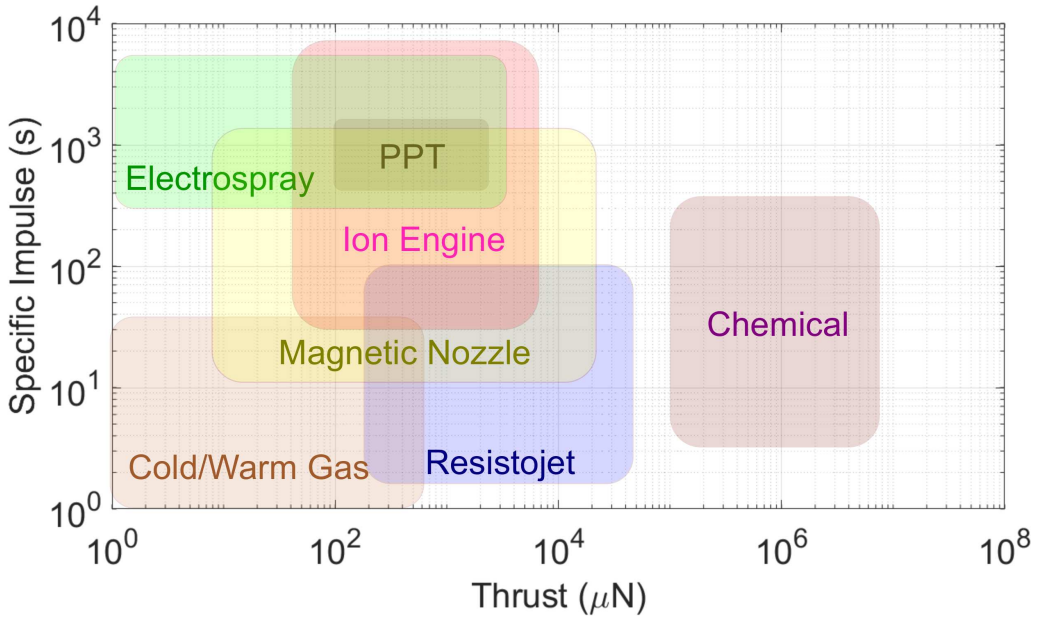

Figure 1.1: A brief overview of the available performance characteristics for different types of propulsion systems that have been developed for small satellites [9, 10, 37, 38, 39, 40, 41, 42, 43, 44, 45, 46, 47, 48, 49, 50, 51, 52, 53, 54, 55, 56, 57, 58, 59, 60, 61, 62, 63, 64, 65, 66, 67, 68, 69, 70, 71, 72, 73, 74].

of propulsion, in some cases, may be dictated by other missions constraints such as maneuver types and mission time. As an example, a timely orbit inclination change (accomplished in a few days or weeks) may require high thrust capabilities (> 1 mN) while station-keeping maneuvers may favor a high specific impulse ($> 1,000$ seconds). Finally, SmallSats have stringent on-orbit power budgets [36] that may act as another propulsion system driver.

As illustrated in Figure 1.1, these diverse propulsion requirements have led to the development of myriad SmallSat propulsion options, many of which stem from attempts to miniaturize propulsion systems originally designed for larger spacecraft (e.g. Hall-Effect Thrusters, ion engines, magnetic nozzles, etc.). However, many of the proposed propulsion options have not yet successfully flown on-orbit; most of the technologies have only a couple of representative systems that have launched [74]. This minimal flight heritage is one technological gap that stands between Small-

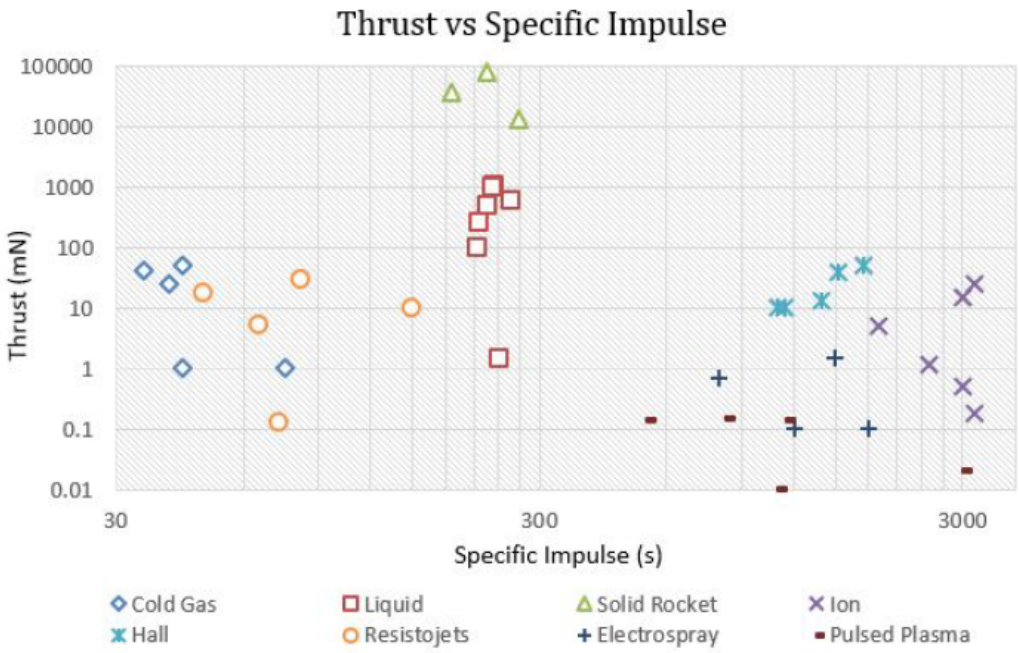

Figure 1.2: Thrust vs. specific impulse for surveyed propulsion systems in Ref. [74]. This figure is reproduced from Ref. [74].

Sats and wide-spread acceptance within the community, albeit one that is currently closing. Another interesting limitation of SmallSat propulsion options is that the thrust performance window tends to be narrow, as shown in Figure 1.2 [74], and that the electric propulsion options do not exhibit a wide range of "throttlability" — the ability to operate over a multitude of power ranges — as shown in Figure 1.3 [74]. This void within the SmallSat propulsion spectrum may render certain mission types infeasible, such as rapid-response, flexible constellations. However, one proposed propulsion technology under development shows promise in regards to filling this gap: the magnetic nozzle.

1.3 Magnetic Nozzles

Magnetic nozzles are a form of electric propulsion where thrust is generated by converting thermal energy stored within an electron fluid into directed kinetic energy

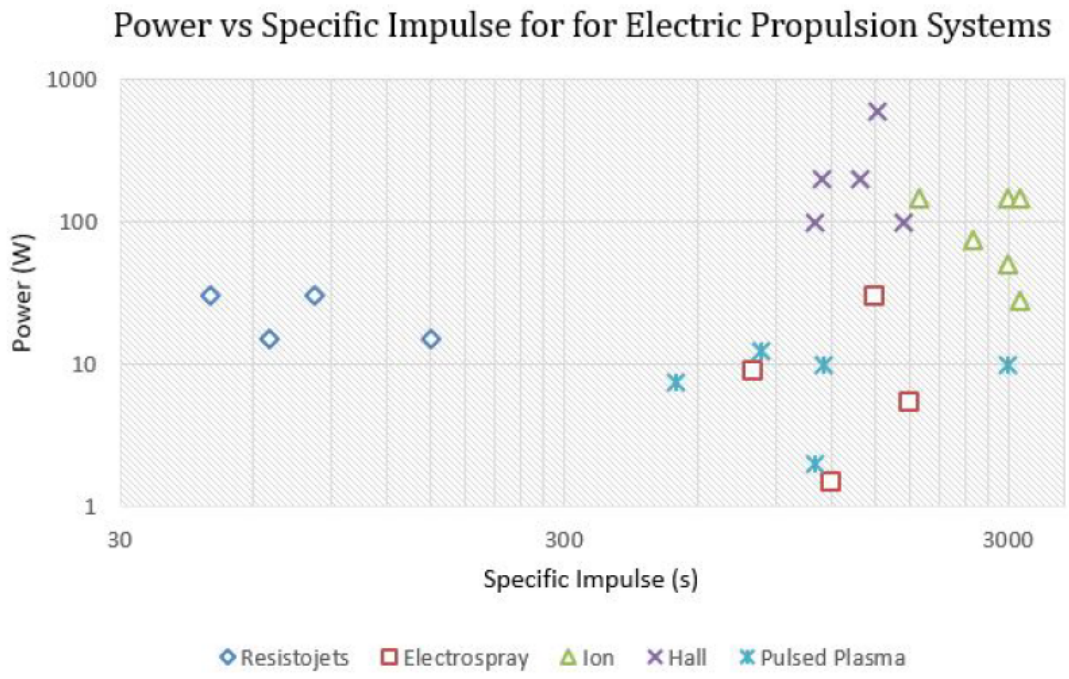

Figure 1.3: Power vs. specific impulse for surveyed electric propulsion systems in Ref. [74]. This figure is reproduced from Ref. [74].

via a convergent-divergent nozzle [39, 60, 75, 76, 77, 78, 79, 80, 81, 82, 83, 84, 85, 86, 87, 88]. As shown in Figure 1.4, the magnetic nozzle topology is reminiscent of conventional rocket nozzles [89], with the magnetic field lines replacing the physical walls. This converging-diverging magnetic circuit is created by electromagnets or a series of permanent magnets. Within the plasma generation and heating region (typically within the converging section) the nozzle is contoured to confine the plasma, thereby limiting radial diffusion to the walls. The confinement of the plasma improves device lifetime by reducing the impingement of high energy particles upon the source tube walls [90, 91] and efficiency by diminishing the amount of plasma-stored energy that is lost to the radial walls [92]. The reduction in radial wall losses effectively increases the fraction of input energy that enters the diverging section of the nozzle, resulting in higher total device efficiencies.

The plasma — the nozzle working fluid comprised of both an electron and ion

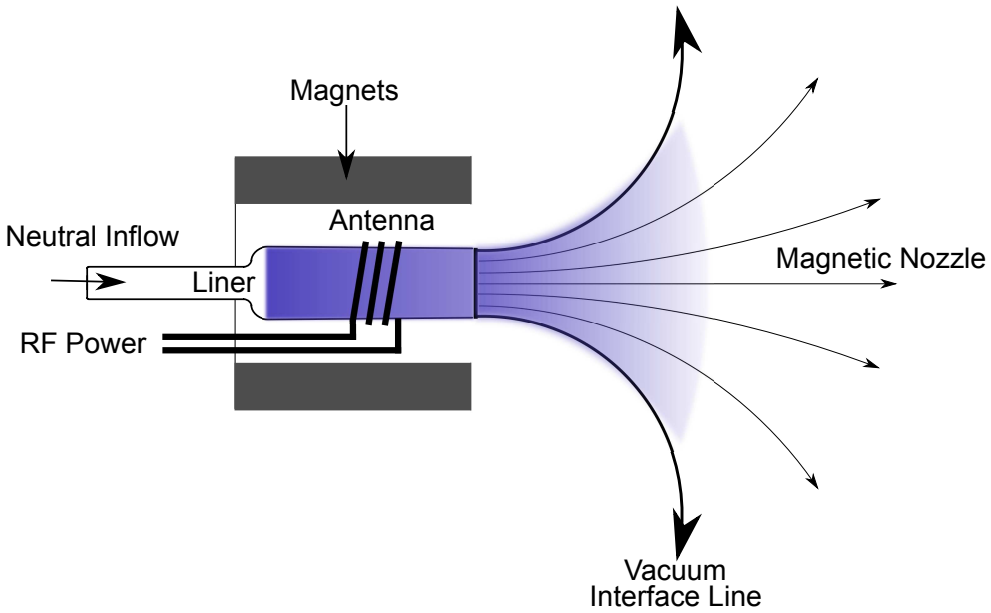

Figure 1.4: A nominal magnetic nozzle configuration.

fluid — is created by injecting neutral propellant into the ionization region where radio frequency (RF) or microwave power creates the plasma and heats the electrons via an antenna. The plasma then expands and accelerates through the converging-diverging magnetic nozzle section, transistioning from subsonic to supersonic flow. Thrust is generated by the plasma expansion process through interaction with the magnetic circuit and diamagnetic currents within the plasma [93]. Additionally, net thrust production requires that the plasma detaches from the closed magnetic nozzle field lines downstream. Laboratory magnetic nozzle devices have experimentally demonstrated net thrust generation, implying that this requisite detachment occurs [37, 38, 76, 94, 95]. However, the physical mechanisms underlying plasma detachment from the nozzle field lines is an open question being explored by the community [83, 84, 86, 96, 97, 98, 99, 100, 101].

Despite the incomplete physical understanding of these devices there has been interest in implementing magnetic nozzles as propulsion units. This interest stems from a number of inherent advantages: 1) due to the absence of a plasma-wetted

electrode these devices can have a longer lifetime compared to other forms of electric propulsion. 2) They can operate on a broad range of propellants, many of which do not require bulky high-pressure storage vessels [102, 103, 104, 105, 106, 107]. 3) They do not require a separate, dedicated neutralizing electron source because the plasma exhaust is neutral. 4) And they offer the ability to operate over a wide range of power and propellant flow rate ranges — exhibiting a degree of "throttlability" [37, 38, 76, 94, 95]. These combine to offer enhanced flexibility, reduced subsystem mass, and cost savings; advantages coveted by all spacecraft, and especially SmallSats.

1.4 Review of Magnetic Nozzles

Until recently, much of the research effort has centered around answering fundamental physics questions and the development of magnetic nozzle devices as an alternative to what is now widely accepted as mainstream electric propulsion technologies (e.g. ion thrusters and Hall-Effect thrusters). As such, until the last decade, most of the insights into magnetic nozzle operation have come from examination of devices designed around moderate power operation (0.5 - 10s of kilowatts). Driven by the apparent propulsion advantages, research on magnetic nozzles as an electric thruster technology has been ongoing for over half a century [93]. In this work we will discuss electron driven magnetic nozzles, or nozzles in which the electron temperature is much larger than the ion temperature ($T_e \gg T_i$). While there are devices for which this statement does not hold, such as the Variable Specific Impulse Magnetoplasma Rocket [87], they are not suitable options for SmallSat propulsion due to their size and power regimes.

1.4.1 Overview of Source Types

The earliest electron heated magnetic nozzle with comprehensive published literature is the Electron Cylcotron Resonance Thruster [26, 108, 109, 110, 111], dat-

ing back to 1962. As depicted in Figure 1.5, this type of device heats the electrons through microwave-plasma coupling. The plasma then expands and accelerates through a converging-diverging magnetic nozzle section. The operating parameters of these devices are specifically tuned around electron resonance to couple power efficiently; the microwave frequency must be closely matched to the electron gyrofrequency around the magnetic nozzle lines in the heating region. To achieve this type of power coupling typically requires peak magnetic field strengths of $700 - 900$ G within the heating zone and microwave frequencies near 2.45 GHz. While the measured plasma properties, namely high ion fraction and electron temperatures, were promising, this device did not demonstrate good efficiency performance, and the electron cylcotron resonance heating method for magnetic nozzle was shelved for several decades [112]. This heating method has undergone a recent resurgence [40, 112, 113, 114, 115, 116, 117, 118, 119] with the increasing interest in miniaturized, low power magnetic nozzles, spurred by the ability to miniaturize the requisite microwave power source.

Another typical magnetic nozzle architecture supplements a helicon plasma discharge with a converging-diverging nozzle section. The helicon plasma heating scheme was initially proposed by Boswell in 1970 [121]. The inclusion of a static magnetic field in the presence of an RF-heated plasma allows for the propagation of an electromagnetic whistler wave further into the plasma than capacitive and inductive heating methods [122]. This helicon wave can be launched in these devices by driving an RF antenna with a particular geometry [123, 124, 125, 126, 127, 128] between 100 kHz and 100 MHz. This type of magnetic nozzle architecture typically exhibits a higher ion fraction, plasma density, and power coupling than its electron cylcotron resonance counterpart, at the expense of electron temperature.

To date, most helicon magnetic nozzles has been performed on devices that can be classified as one of two types: ambipolar-driven [81, 129, 130, 131] and double layer-

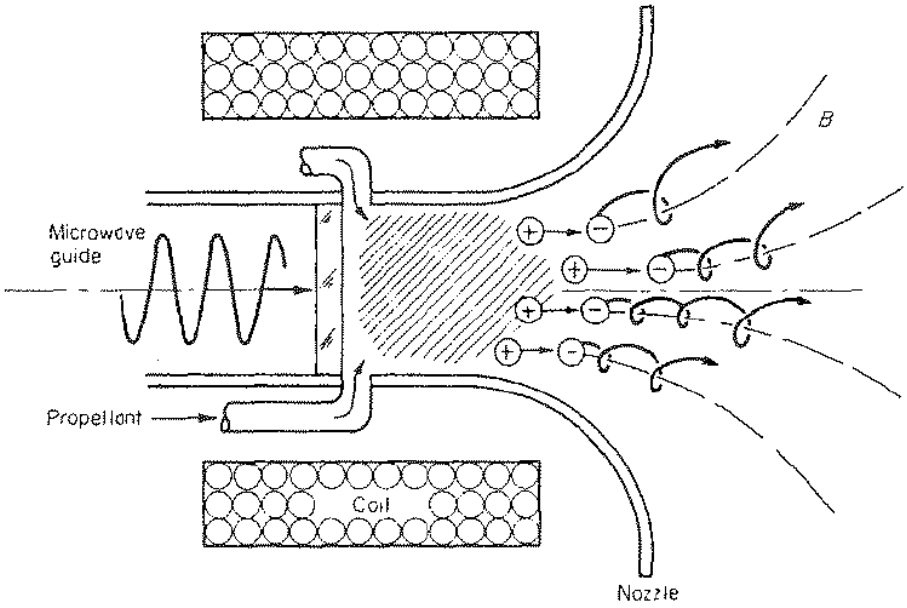

Figure 1.5: A schematic of the Electron Cyclotron Thruster. This figure is reproduced from Ref. [120].

driven [78, 79, 132, 133, 134]. As the classification names imply, the primary distinction between the two types is the electron acceleration process. In an ambipolar-driven device the ions are accelerated by the potential structure established through the expansion of the electron fluid [81, 129, 130, 131]. Conversely, in a double layer-driven device the ion acceleration stems from the sharp potential drop across the double layer — a non-neutral potential structure with a large potential gradient between two sheets of charge [79, 132]. A significant body of work exists in published literature for both classifications of devices, particularly in the moderate power regime (0.5 - 5 kW), so we will focus on their performance in our discussion here.

1.4.2 Overview of Measurement Techniques

From a mission perspective, each propulsion option is evaluated by its performance metrics — namely, the thrust and specific impulse. Traditionally, there are two methods of determining these metrics: indirect and direct. In the indirect method,

measurements of plasma properties in the expanding nozzle (electron temperature, plasma density, plasma potential, etc.) and device operating parameters (power, propellant mass flow rate, etc.) are coupled with existing theoretical models to estimate the performance [94, 95]. This leads to uncertainty in the predicted performance due to the compounding of uncertainty of the many measurements required and the fundamental assumption that the applied theoretical framework accurately captures the dominant processes present within the device. Due to these disadvantages, it it often preferable to employ direct methods, primarily through the use of a thrust stand. In this method, the thruster is mounted to a thrust stand during operation. There are several commonly used types of thrust stands including pendulum [106, 135], inverted pendulum [136], and torsional balance [137]. The type used depends on the device architecture, expected thrust levels, and facility infrastructure, but the common end product is the direct measurement of the reactionary thrust force. This force measurement is combined with the device operating parameters to obtain the specific impulse and total efficiency metrics. There are two primary advantages to using this direct performance method: no measurements must be combined, so the compounding of error is minimized, and the thrust generated includes the effect of all physical processes present in the device.

While the direct measurement of performance is preferred, this is not always possible. Depending on the thruster and facilities thrust stands can be complicated instruments, and it can be difficult to validate the measurements. In our discussion of the state-of-the-art here we will focus on performance results that have been obtained directly, but note that indirect performance measurements can provide useful insight into thruster operation.

Table 1.1: An overview of moderate power magnetic nozzle experiments and the measured performance. Here, type "DL" indicates that the device is double layer-driven, while type "A" denotes an ambipolar-driven thruster.

Year	Type	P (W)	B (G)	$\dot{m}$ (mg/s)	T (mN)	I_{sp} (s)	η_T (%)	Ref.
2011	DL	≤ 650	100	≤ 1.00	≤ 2.8	≤ 280	≤ 1	[138]
2012	DL	≤ 500	≤ 110	≤ 0.55	≤ 1.1	≤ 200	≤ 1	[139]
2013	A	≤ 840	≤ 450	≤ 4.50	≤ 6.3	≤ 380	≤ 2	[80]
2013	A	$\leq 2,000$	≤ 715	≤ 7.60	≤ 10.8	≤ 303	≤ 1	[140]
2013	A	$\leq 2,000$	300	≤ 0.72	≤ 15.0	$\leq 2,000$	≤ 8	[77]
2015	A	≤ 500	420	≤ 0.50	≤ 4.7	≤ 960	≤ 5	[83]

1.4.3 Survey of Experimental Results

In the past decade, several moderate power magnetic nozzle devices have been constructed to investigate the physical mechanisms dictating performance. We summarize these experiments and the measured performance in Table 1.1. Here, we limit the scope of the survey to experiments that directly measure thrust performance.

The low measured performance has been attributed to plasma losses to the thruster walls [76] and low mass utilization efficiency due to poor ionization fractions [138]. Both of these loss mechanisms have been observed in many magnetic nozzles. One example of the potential severity of the radial wall loss mechanism can be found in Figure 1.6. The low performance has also been attributed to ionization losses. These losses are an inherent underlying issue with magnetic nozzles; in general, the ionization losses are related to the electron temperature. The low electron temperature (and corresponding high ionization losses) in many nozzles can yield a low maximum efficiency, as shown in Figure 1.7.

To date, the best performance has been measured by Takahashi et. al. [77] using an ambipolar-driven magnetic nozzle that employed permanent magnets. To further enhance performance they suggested adding a physical nozzle at the thruster exit plane to convert energy stored in the neutral population [141] and increasing the magnetic field to reduce plasma flux to the thruster walls [142]. However, it is

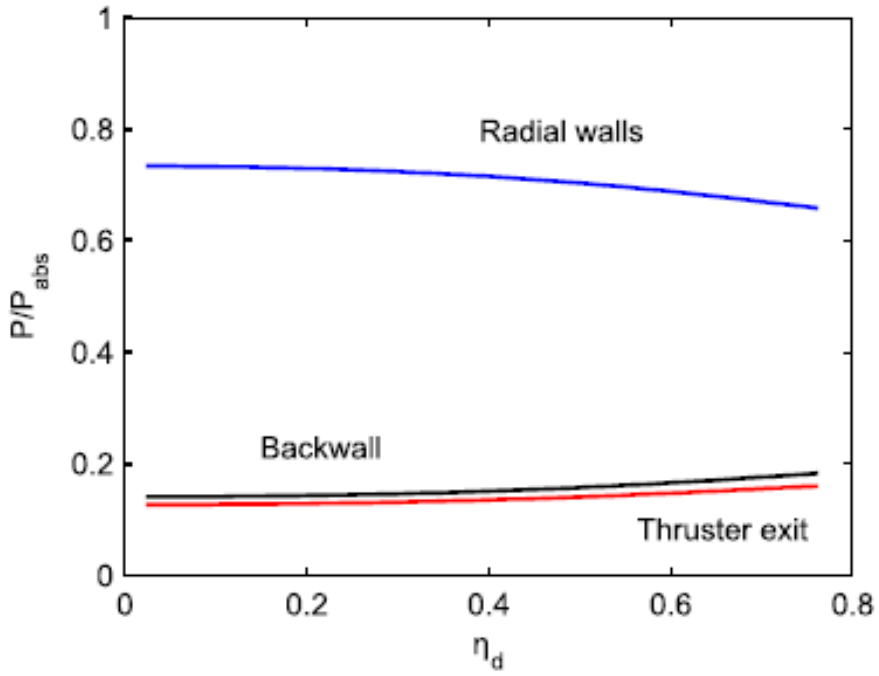

Figure 1.6: Normalized power losses in the source region of thruster D (see Ref. [94]) as a function of propellant utilization. This figure is reproduced from Ref. [94].

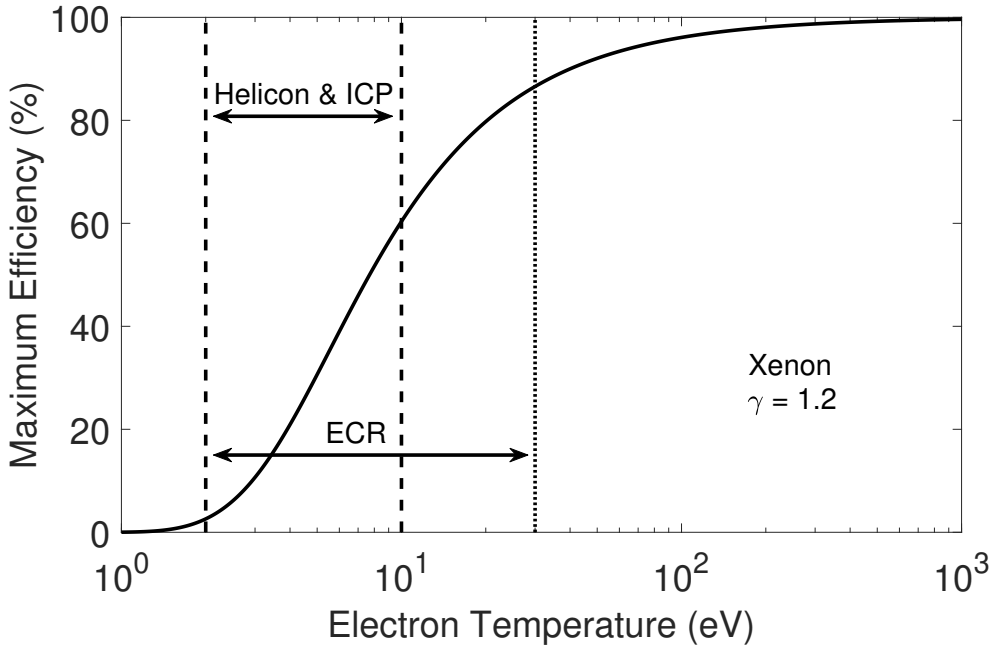

Figure 1.7: The nozzle efficiency of a general magnetic nozzle as a function of electron temperature. Note that, due to the nature of the total efficiency being the product of all of the component efficiencies, this is the generalized maximum efficiency of a magnetic nozzle.

important to note that during this experimental campaign the facility background pressure was $\sim$ 1 mTorr. This is well above the threshold at which facility effects become negligible [143] and may have resulted in artificially inflated performance measurements [144]. Despite this potential mitigating factor, it is clear that magnetic nozzles have not yet reached desirable performance levels. Further understanding is required to overcome the existing limitations and improve performance.

1.4.4 Review of Theoretical Work

A number of models have been proposed to explain the low performance of these state-of-the-art devices. One of the early models that treated helicon magnetic nozzles was proposed by Fruchtman [145]. In this 1D collisionless model it was concluded that the primary sources of performance loss could be explained by high ionization costs and the loss of energy incident on the rear wall of the source region. In another iteration of this model [146] the plasma was assumed to be collisional, which captured a reduction in the efficiency performance. It was therefore concluded that collisionality played a role in the low measured thrust efficiency. Due to the 1D nature of this model it did not incorporate some possible performance loss inducing effects like radial wall losses and plume expansion.

This work was supplemented by extensive 2D modeling efforts starting with the model proposed by Ahedo and Navarro-Cavalle [92]. This model included collisionality, plume expansion, and energy fluxes to all boundaries within the source region. Using this model, they were able to conclude that partial energy recovery within the plume and radial wall losses also had a role in degrading thrust performance (in addition to the findings of Fruchtman). Efficient operation of these devices requires the minimization of these effects: the magnetic field must be of sufficient strength to minimize plasma diffusion to the radial walls and the bulk electron temperature must be high to minimize ionization losses. If these loss mechanisms could be overcome the

predicted total efficiency could reach $\sim 25\%$ and the specific impulse could exceed $2,500$ seconds [92].

In addition to the modeling efforts directed at understanding the underlying phenomena that affect performance, there has been substantial research into plasma detachment mechanisms. In a model developed by Hooper [98], the ions and electrons are predicted to detach inwards with respect to the local magnetic field due to electron inertia. However, this model assumes that both the electron and the ion species are cold ($T_e = T_i = 0$), which limits its application to electron-driven magnetic nozzles. In a study by Ahedo and Merino [147] a two fluid model that included finite electron temperature was used to derive analytical expressions describing electron behavior throughout the nozzle. With this model they observed plume divergence losses of up to $\sim 40\%$ and found that these losses increased with increasing magnetic field strength, decreased with a centerline-peaked plasma density profile, and decreased with decreasing magnetic field divergence. In extensions of their model, they have examined far-field ion detachment [84], thermodynamic effects on the plume structure [148], and finite electron effects [149]; however, these extended models have not yet been experimentally validated.

1.4.5 Major Outstanding Questions from Previous Work

In contrast to the extensive heritage of moderate-power mangetic nozzles, research into low-power magnetic nozzles — thruster architectures that may be suitable for SmallSats — is a relatively new field of study. A few test devices have been constructed in the last several years, but, like their moderate state-of-the-art counterparts, they have demonstrated low efficiency performance. These experiments and the resulting performance is summarized in Table 1.2. As in Section 1.4.3, we limit the scope to experiments that report directly-measured performance.

A few studies have attempted to use the first-principles models developed for

Table 1.2: An overview of moderate power magnetic nozzle experiments and the measured performance. Here, type "ECR" indicates that the device is an electron resonance thruster, while type "A" denotes that it is ambipolar-driven. For the device in Ref. [38], the author states that a propietary magnetic field is employed, but does not disclose the field strength. As such, this entry is labeled as not reported (NR).

Year	Type	P (W)	B (G)	$\dot{m}$ (mg/s)	T (mN)	I_{sp} (s)	η_T (%)	Ref.
2017	ECR	≤ 50	850	≤ 0.125	≤ 0.95	$\leq 1,300$	≤ 12.5	[40]
2018	A	≤ 500	NR	≤ 1.00	≤ 9.00	$\leq 1,500$	≤ 10	[38]

moderate power magnetic nozzles to explain the low measured performance in these low power devices [113, 114, 150]. However, these models have had limited success unless the model included modifications. While the moderate power magnetic nozzle loss mechanisms exist in low power devices (refer to Figure 1.8, which shows the radial wall losses in a prototype low power magnetic nozzle [39, 75, 150]) they are insufficient to explain the low measured performance. The requisite modifications to match the models with experimental data suggests that there may be other adverse effects, in addition to the radial wall and frozen flow lossess observed in moderate power devices, that impact magnetic nozzle performance at low power. To date, several additional adverse mechanisms have been proposed, including diffusion and ionization [113] and plasma-neutral collisional effects [151]. However, most models developed for moderate power magnetic nozzle have neglected these mechanisms [84, 92, 94, 149, 152], so the impact on nozzle performance is unclear.

In summary, previous experimental, theoretical, and numerical work on moderate and low power magnetic nozzle thrusters have identified a number of underlying parameters that dictate thrust performance. In the context of SmallSat propulsion the following major questions remain unanswered:

1. *How much, if any, of this heritage moderate power nozzle work applies to low power operation?*

2. *What underlying mechanisms adversely affect low power magnetic nozzle thrust*

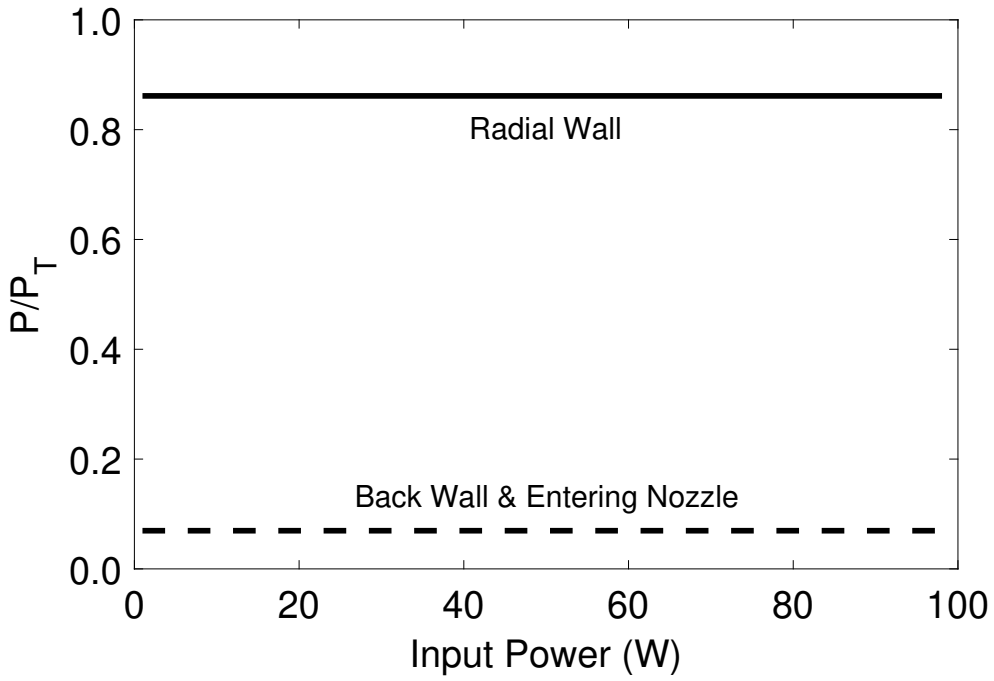

Figure 1.8: The fraction of power diffusing to each boundary within the plasma liner for an early prototype of the CubeSat Ambipolar Thruster [39, 75, 150].

performance?

3. *Can these mechanisms explain the discrepancies between predicted and measured performance when using conventional moderate power magnetic nozzle models to evaluate low power devices?*

The ultimate goal of this dissertation is to build upon previous works to answer these fundamental questions.

1.5 Dissertation Approach

In our analysis we characterize the thrust and efficiency performance to identify device conditions indicative of an adverse mechanism and for comparison to performance values predicted by conventional moderate power magnetic nozzle models. Using the device performance as a guide, our aim is to use experimental measurements to identify potential mechanisms that adversely affect low power magnetic

nozzle thrust performance. We couple these experimental measurements with a general theoretical framework to correlate these mechanisms with the discrepancies in performance values predicted by conventional magnetic nozzle models. Our results will provide insight into underlying mechanisms that may be dominant in magnetic nozzles operating in the low power regime. We aim to use these insights to inform future low power magnetic nozzle modeling and technology development efforts to improve the thrust and efficiency performance of these devices.

1.6 Dissertation Outline

Chapter 2 begins with a theoretical discussion of magnetic nozzle thrust performance. We leverage quasi-1D gasdynamic nozzle theory and an existing generalized electric propulsion efficiency framework to derive a general quasi-1D expression for nozzle efficiency that we can use in tandem with experimental results to evaluate thrust performance. In Chapter 3 we describe the experimental setup, methods, and diagnostics used to investigate the presence presence of adverse mechanisms and their impact on performance. In Chapter 4 we present experimental measurements of our test article operating in a regime possibly conducive to plasma-neutral collisional mechanisms. We identify an experimental indicator that corresponds to performance loss compared to the predicted performance and correlate these mechanisms with this indicator. In Chapter 5 we present experimental measurements of our test article operating in a configuration conducive to non-uniform power deposition and discuss the implications of this mechanism on thrust performance. In Chapter 6 we present experimental measurements of our test article operating in configuration designed to mitigate the plasma-neutral collisional and non-uniform power deposition mechanisms and discuss its thrust performance. Finally, in Chapter 7 we summarize our key findings, discuss the implications of our work on future low power magnetic nozzle modeling and development efforts, and suggest additional avenues of research.

CHAPTER II

Model for Magnetic Nozzle Performance

While the primary performance metrics (thrust, specific impulse, and efficiency) apply to all devices, the primary goal of this work is to investigate the underlying drivers that can adversely impact performance of low power magnetic nozzles. To this end, we present analytical forms for the performance metrics of magnetic nozzles. In this chapter we leverage quasi-1D gasdynamic nozzle theory [89, 153] and existing efficiency models for electric propulsion devices [154, 155] to derive performance metrics in terms of plasma parameters that can be measured using existing plasma diagnostic techniques, thereby allowing for direct comparison between theoretical and empirical performance metrics.

2.1 Magnetic Nozzle Thrust

Functionally, there are differences between gasdynamic nozzles and magnetic nozzles. Thrust generation in gasdynamic nozzles is due to the force of an expanding gas on the physical walls of the device while in magnetic nozzles thrust is generated via plasma pressure and diamagnetic currents inteacting with the magnetic circuit. Despite these differences, magnetic nozzles have been analyzed using conventional quasi-1D nozzle theory [85, 94, 156].

To clarify the analogy we are building, for a magnetic nozzle the momentum

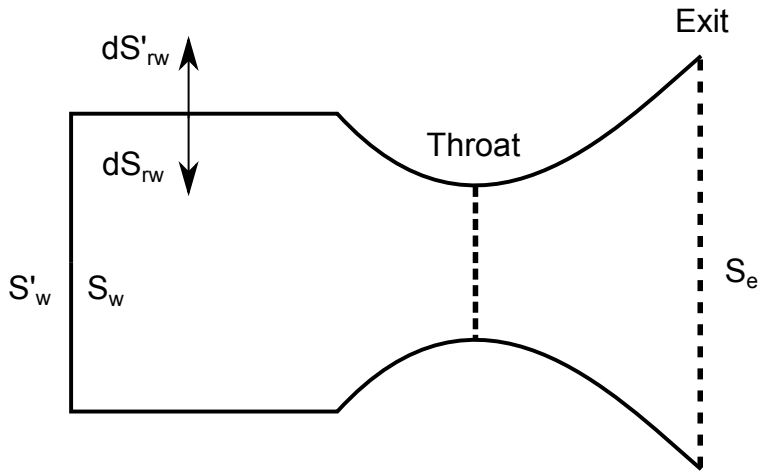

Figure 2.1: A general rocket chamber and nozzle.

exchange in the nozzle is viewed from the perspective of the heavier species — the ions. While the ions are too massive to be magnetized in most electron-driven magnetic nozzles, they are electrostatically accelerated by potential gradients that arise from the expansion of the electrons. This electron expansion process is directly analagous to the expansion of propellant in gasdynamic nozzles; during this expansion the thermal energy of the propellant is converted to directed acceleration of the propellant. Here the thermal energy is stored within the electron fluid and the accelerated species is the ions.

In a gasdynamic nozzle the propellant is accelerated until the exit plane of the nozzle is reached. To further develop the analogy, the ions (propellant) are accelerated to the detachment plane of the magnetic nozzle. Therefore, the detachment plane and the exit plane of a magnetic and gasdynamic nozzle, respectively, are equivalent. Significantly, this analogy carries beyond a qualitative analysis: gasdynamic nozzles, like magnetic nozzles, lend themselves to quasi-1D nozzle expansion theory (c.f. [89, 153]).

We begin the development of our theoretical magnetic nozzle performance framework with a discussion of this quasi-1D gasdynamic nozzle performance theory. The

first performance metric that we wish to employ in our analysis is the thrust from the device. Following the derivation of Oates [153], The thrust for a general gasdynamic nozzle (see Figure 2.1) can be calculated through a control volume analysis of the momentum equation. In its general form, the thrust for the pictured nozzle can be written as

$$\vec{F} = -\iint_{S_w} (p - p_a) d\vec{s} + (\text{visc})_{S_w}. \tag{2.1}$$

Here $\vec{F}$ is the force, S_w is the internal wall surfaces, $d\vec{s}$ is a unit normal vector, p is the pressure, p_a is the ambient pressure at the exit plane, and $(\text{visc})_{S_w}$ is the viscous forces acting on the internal walls. Note that the first term in this expression represents the forces on the internal walls. However, this form is of limited usefulness due to the complexity of the wall integrals. Instead, we can relate these integrals to properties at the nozzle exit by using the momentum equation. By equating the momentum convection out of the nozzle and forces on the internal walls our equation becomes

$$\iint_{S_e} (\rho\vec{u})\vec{u} \cdot d\vec{s} = -\iint_{S'_w} (p - p_a) d\vec{s} - \iint_{S_e} (p - p_a) d\vec{s} + (\text{visc})_{S'_w} + (\text{visc})_{S_e}. \tag{2.2}$$

Here S_e is the exit plane surface, S'_w is the external surface of the walls, ρ is the mass density, and $\vec{u}$ is the velocity vector. Note that the normal vectors of S_w and S'_w are equal, but in opposite direction. This implies that the corresponding force contributions on these surfaces are also equal, but of opposite sign. Also, because the exit plane (S_e) is a boundary in our control volume, we can assume that the viscous forces on this plane are negligible. Accounting for these two effects immediately yields an expression for the thrust:

$$\vec{T} = \iint_{S_e} (\rho\vec{u})\vec{u} \cdot d\vec{s} + \iint_{S_e} (p - p_a) d\vec{s}. \tag{2.3}$$

If we then apply the assumption that properties do not vary significantly across the nozzle cross-sectional area at a given location (the quasi-1D assumption), then the thrust may be written as

$$T = \rho u_e^2 A_e + (p_e - p_a) A_e. \tag{2.4}$$

Here u_e is the axial velocity at the nozzle exit plane, p_e is the pressure at the exit plane, and A_e is the exit plane cross-sectional area. For convenience we can also introduce the propellant mass flow rate:

$$\dot{m} = \rho u_e A_e. \tag{2.5}$$

Using this mass flow rate expression the thrust expression becomes

$$T = \dot{m} u_e + (p_e - p_a) A_e. \tag{2.6}$$

We can also write this expression as $T = \dot{m}C$, where C is the effective exhaust velocity. The comparison of Eqs. 2.4 and 2.6, yields an immediate expression for the effective exhaust velocity:

$$C = u_e + \frac{(p_e - p_a) A_e}{\dot{m}}. \tag{2.7}$$

We now introduce the Mach number, which is a normalization of the local velocity by the local sound speed

$$M = \frac{u}{\sqrt{\gamma k T_g / m_g}}. \tag{2.8}$$

where γ is the polytropic index, k is the Boltzmann constant, T_g is the gas temperature, and m_g is the mass of a single molecule of the gas. Combining Eqs. 2.7 and 2.8 yields an alternate form for the effective exhaust velocity:

$$C = u_e \left[1 + \frac{1}{\gamma M_e^2} \left(1 - \frac{p_a}{p_e} \right) \right]. \tag{2.9}$$

If we assume that our nozzle will be operating in a space environment (i.e. that $p_a/p_e \to 0$), the effective exhaust velocity expression transforms into

$$C = u_e \left(1 + \frac{1}{\gamma M_e^2} \right). \tag{2.10}$$

Interestingly, the quadratic scaling of the effective exhaust velocity with Mach number suggests that, at high exit Mach numbers, the effective exhaust velocity approaches the propellant velocity at the exit plane ($C \to u_e$). In fact, as Figure 2.2 illustrates, the effective exhaust velocity is within 10% of the propellant exit velocity at exit Mach numbers of $\sim$ 2.0 - 3.5. This holds across all physically possible nozzle types — isothermal ($\gamma = 1$) to adiabatic ($\gamma = 5/3$). This implies that, for a sufficiently accelerated propellant, the pressure term in the thrust expression (Eq. 2.6) may be assumed to be negligible, which simplifies the form of our various performance terms.

Throughout this derivation the model has assumed that there is a single working fluid — the propellant. However, a plasma is generally a fluid comprised of three species: the electrons, ions, and neutrals. To strengthen the analogy between gasdynamic and magnetic nozzles, we neglect the neutral species and examine the collisionless electron and ion momentum equations:

$$m_i n_i \vec{u}_i \cdot \nabla \vec{u}_i = -\nabla(n_i T_i) + q n_i \nabla \phi + q n_i \vec{u}_i \times \vec{B}, \tag{2.11}$$

and

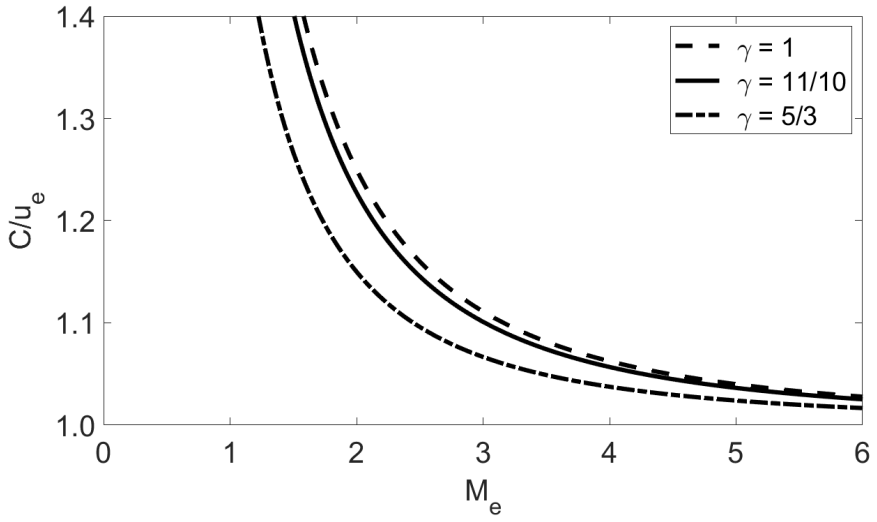

Figure 2.2: The effective exhaust velocity as a function of polytropic index and working fluid Mach number at the nozzle exit plane (refer to Eq. 2.10).

$$m_e n_e \vec{u}_e \cdot \nabla \vec{u}_e = -\nabla(n_e T_e) - q n_e \nabla\phi + q n_e \vec{u}_e \times \vec{B}. \tag{2.12}$$

Here, subscript i denotes an ion property, subscript e denotes an electron property, T is the temperature, n is the number density, ϕ is the potential, and B is the magnetic field. If we assume that the ions are cold, the electrons are massless, the plasma is quasi-neutral throughout the nozzle, and the plasma expands approximately along the nozzle field lines these species momentum equations simplify to

$$m_i n \vec{u}_i \cdot \nabla \vec{u}_i = q n \nabla\phi, \tag{2.13}$$

and

$$0 = -\nabla(n T_e) - q n \nabla\phi. \tag{2.14}$$

From this formulation it is immediately apparent that the, through the linkage of electric field ($qn\nabla\phi$), that the expansion of the electron fluid dictates the acceleration

of the ions. Combining the electron and ion momentum equations by eliminating the electric field yields

$$m_i n \vec{u}_i \cdot \nabla \vec{u}_i = -\nabla(nT_e). \tag{2.15}$$

Rearranging, it is clear that axial momentum is conserved throughout the nozzle:

$$\frac{d}{dz}\left(m_i n u_i^2 + p_e\right) = 0. \tag{2.16}$$

Here p_e is the electron pressure. Integrating the axial momentum across the nozzle cross-section yields an expression the thrust

$$T = \int_0^{r_{p(z)}} \left(m_i n u_i^2 + p_e\right) 2\pi r dr. \tag{2.17}$$

Following the quasi-1D approach that we have taken with the gasdynamic nozzle derivation, this thrust expression yields a form similar to Eq. 2.6:

$$T = m_i n u_i^2 A + p_e A = \dot{m} u_i + p_e A. \tag{2.18}$$

This suggests that gasdynamic and magnetic nozzles are analogous, where the thermal energy of the propellant (as stored in the electrons) is converted to directed acceleration of the propellant (as represented by the ions). Armed with this information, we can now formalize the second primary performance metric: the specific impulse. The specific impulse is defined as the ratio of the thrust to the propellant weight flow, or

$$I_{sp} = \frac{T}{\dot{m} g_0} = \frac{C}{g_0}, \tag{2.19}$$

where g_0 is the gravitational acceleration on the surface of Earth. Now that we have expressions for the thrust and specific impulse parameters, as derived through the lens of traditional, quasi-1D gasdynamic nozzle theory, we can turn to determining

an efficiency architecture that can provide useful insights into our magnetic nozzle analysis.

2.2 Magnetic Nozzle Efficiency

On a fundamental level, the total efficiency for an electric thruster is the amount of power that generates thrust compared to the total input power [154, 155]. This can be simply expressed as

$$\eta_T = \frac{P_{jet}}{P_{in}}, \tag{2.20}$$

where η_T is the total efficiency, P_{jet} is the thrust-producing power, and P_{in} is the total input power. However, this form, while general, provides limited insight into the causes of efficiency loss within a given device. Instead, these insights can be gleaned by decomposing the total efficiency into component efficiency terms. We begin with an expression for P_{jet} in terms of the propellant flow rate and the exhaust velocity. Noting from Eq. 2.6, that the thrust is dependent on the propellant exhaust velocity, we can write the expression for P_{jet} as a kinetic thrust power:

$$P_{jet} = \frac{1}{2}\dot{m}v_{ex,z}^2, \tag{2.21}$$

where $v_{ex,z}$ is the axial component of the exhaust velocity. We can immediately substitute this form into Eq. 2.20 to yield

$$\eta_T = \frac{\dot{m}v_{ex,z}^2}{2P_{in}}. \tag{2.22}$$

However, we also note that thrust force is actually due to the projection of $\vec{v}_{ex}$ onto the thrust axis. This indicates that energy stored in any transverse motion is a loss mechanism. The ratio of the jet power to the total fluid kinetic power is known

as the divergence efficiency:

$$\eta_{div} = \frac{P_{jet}}{P_k} = \frac{(|\vec{v}_{ex}| \cos\theta_{div})^2}{|\vec{v}_{ex}|^2} = \cos^2\theta_{div}. \tag{2.23}$$

Here P_k is the total kinetic power and θ_{div} is the angle between the thrust axis and $\vec{v}_{ex}$ - also known as the divergence angle. Using this relation we can recover an expression for thrust that is similar to that in Eq. 2.6, but preserves information regarding plume divergence:

$$T = \dot{m}|\vec{v}_{ex}| \cos\theta_{div}. \tag{2.24}$$

Noting that $v_{ex,z} = |\vec{v}_{ex}| \cos\theta_{div}$, this expression for thrust can be inserted into the total efficiency (Eq. 2.22) to yield

$$\eta_T = \frac{T^2}{2\dot{m}P_{in}}. \tag{2.25}$$

Embedded within this expression is the propellant mass flow rate. However, in a low temperature device, such as a magnetic nozzle, a fully ionized plasma is unlikely. Assuming that neutrals negligibly contribute to thrust production, a more appropriate form of the mass flow rate is that of the working fluid (the plasma):

$$\dot{m}_{ion} = m_i n_e u A, \tag{2.26}$$

where m_i is the ion mass, n_e is the plasma density, u is the velocity of the ions leaving the source region, and A is the cross-sectional area of the source region. Note that the plasma is assumed to be quasineutal in the source region, so the electron and ion densities are approximately equal and the ions are singly charged. We can now capture the performance effects of a partially ionized plasma with the mass utilization efficiency:

$$\eta_m = \frac{\dot{m}_{ion}}{\dot{m}}. \tag{2.27}$$

Substituting the mass utilization efficiency into Eq. 2.25 yields

$$\eta_T = \frac{T^2}{2\dot{m}_{ion}P_{in}}\eta_m. \tag{2.28}$$

However, further insights into the physical device operation can be obtained by decomposing P_{in} into subcomponents. In RF and microwave devices a fraction of the total input power may be consumed by parasitic losses [157, 158], such as transmission line heating. Additionally, impedance mismatches between the power transmission lines and the plasma load generally results in the reflection of a portion of the input power [157, 158] - this power is not absorbed by the plasma. The resulting reduced power coupling into the plasma is captured in the power coupling efficiency:

$$\eta_{rf} = \frac{P_{dep}}{P_{in}}, \tag{2.29}$$

where P_{dep} is the power deposited into the plasma.

Like before, this component efficiency can be substituted into the total efficiency expression (Eq. 2.28) to yield an intermediate expression

$$\eta_T = \frac{T^2}{2\dot{m}_{ion}P_{dep}}\eta_{rf}\eta_m. \tag{2.30}$$

Assuming that the plasma source region is comprised of a cylindrical section —- typical of magnetic nozzles [77, 78, 80, 81, 84, 85, 86, 88, 94, 95, 113, 132, 148, 152, 159, 160, 161, 162, 163, 164] — and leveraging a simple control volume power balance, the deposited power (P_{dep}) can be further separated into energy fluxes to each surface. In the assumed cylindrical geometry these fluxes are power flows to the source back wall, radial walls, and into the diverging nozzle section. This is captured by

$$P_{dep} = P_{bw} + P_r + P_{noz}, \tag{2.31}$$

where P_{bw} is the power incident on the back wall, P_r is the power incident on the radial walls, and P_{noz} is the power flowing into the nozzle. All terms are effectively due to plasma diffusion to the boundaries of the source region. Of these three terms, the power flowing into the nozzle is the only one that can be converted into directed kinetic energy; the other two terms are efficiency loss terms. As the back wall and radial wall terms are loss mechanisms, it is desirable to minimize them; proposed mitigation methods have included back wall shielding [92] through magnetic field contouring and increasing the magnetic field within the source region to limit diffusion to the radial walls [92, 94]. However, these solutions may interfere with nuanced power coupling mechanisms [165, 166] and lead to lower electron temperatures [122] thereby reducing efficiency through other means. In any case, the fraction of the deposited power that enters the diverging nozzle section can be captured by the source region efficiency:

$$\eta_{loss} = \frac{P_{noz}}{P_{dep}}. \tag{2.32}$$

Substituting this component efficiency expression into the total efficiency (Eq. 2.30) yields

$$\eta_T = \frac{T^2}{2\dot{m}_{ion}P_{noz}}\eta_{rf}\eta_{loss}\eta_m. \tag{2.33}$$

The remaining terms on the right hand side of this equation, excluding the component efficiencies, captures the conversion of thermal energy stored within the plasma into directed kinetic energy [83, 92, 94, 146, 152] and is the product of the energy conversion and divergence efficiencies. This is termed the nozzle efficiency:

$$\eta_{noz} = \frac{T^2}{2\dot{m}_{ion}P_{noz}}. \tag{2.34}$$

The total thrust efficiency for a magnetic nozzle, as a product of component efficiency terms, takes the form of

$$\eta_T = \eta_{rf}\eta_{loss}\eta_m\eta_{noz}. \tag{2.35}$$

This general form provides insights into the physical performance loss mechanisms and captures information regarding the power coupling, plasma source region losses, partial ionization of the plasma, the energy conversion processes in the nozzle section, and the divergence losses. While this general expression for the total efficiency provides a theoretical framework that is adapted from the efficiency architectures for other electric propulsion devices [154, 155], not all of the component efficiency terms are in forms that are conducive to comparison with experimental measurements. In the next section we further manipulate these equations into forms that lend themselves to direct comparison with experimental results.

2.3 Nozzle Efficiency

We can now combine the gasdynamic quasi-1D analysis where the thrust is related to the cross-section of the nozzle and the efficiency architecture to estimate the performance of an ideal magnetic nozzle. We apply this formalism to discuss the expansion and acceleration of the exhaust through the throat with cross-sectional area, A_0, and the exit plane with cross-sectional area, A_d. As shown in Figure 2.3, the radius of the nozzle geometry at each location is defined from the centerline to the vacuum interface line - the magnetic field line that grazes the edge of the source at the exit plane.

For this ideal analysis we leverage insight from previous analytical studies [83, 84, 85, 86, 92, 94, 96, 98, 114, 147, 149, 152, 164] to make four key assumptions:

- The neutral species can be neglected

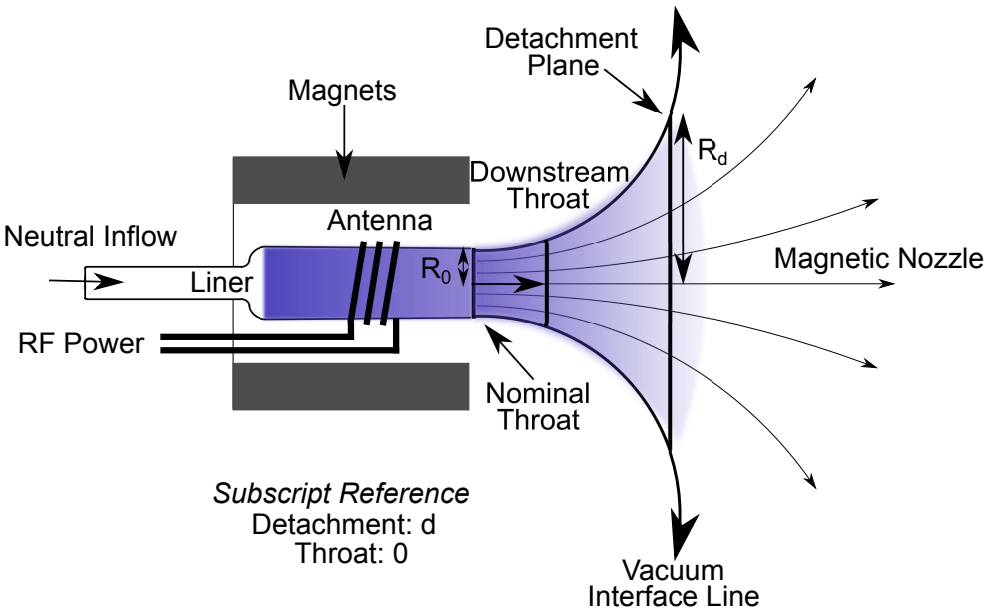

Figure 2.3: A nominal magnetic nozzle configuration with points of interest identified.

- The ions are cold
- The ions are sonic at the throat (location of peak magnitude field), i.e. $M = u_0/c_s = 1$, where M denotes the ion Mach number and c_s is the local Bohm speed ($c_s = \sqrt{\gamma q T_e/m_i}$)
- The plasma expansion is polytropic and governed by an equation of state $T_e(n_e)^{1-\gamma} =$ constant, where $1 \leq \gamma \leq 5/3$

We begin with the nozzle efficiency equation in Eq. 2.34 and assume that the plasma is singly ionized. Due to the low electron temperatures [83, 88, 94, 151] in these devices, this assumption is plausible. Of the three terms in this Eq. 2.34, we have the expressions for the thrust (Eqs. 2.6 and 2.24) and the ion mass flow rate (Eq. 2.26) in terms of measurable quantities. We are missing an expression that relates the power flowing into the nozzle to measurable plasma quantities. In a magnetic nozzle, there are four primary energy fluxes that must be accounted: ion kinetic energy, internal energy stored within the plasma pressure, heat conduction,

and ion production costs. The sum of these four energy fluxes describes the power that flows into the nozzle. The power associated with the ion kinetic energy at the nozzle throat can be written as

$$P_v = \int_0^{R_s} \pi m_i n_{e,0} u_0^3 r dr, \tag{2.36}$$

where the subscript 0 denotes the value at the nozzle throat and R_s is the source tube radius at the exit plane. The power stored within the plasma pressure is

$$P_p = \int_0^{R_s} 5\pi q n_{e,0} T_{e,0} u_0 r dr. \tag{2.37}$$

The heat conduction term [148], assuming that the expanding plasma in the nozzle is globally governed by polytropic cooling, can be written as

$$P_Q = \int_0^{R_s} 3\pi q n_{e,0} T_e u_0 \left(\frac{5/3 - \gamma}{\gamma - 1} \right) r dr, \tag{2.38}$$

where γ is the polytropic index. Physically, this is the energy flowing through the electron fluid along the nozzle field lines to maintain the plasma gradients present within the plume. The power consumed in producing the ions is

$$P_c = \int_0^{R_s} 2\pi q n_{e,0} \epsilon_c u_0 r dr, \tag{2.39}$$

where ϵ_c is the ion cost in eV. The ion cost can be interpreted as the net energy required to create an electron-ion pair. The ion cost can be determined from [122]

$$K_{iz}(T_e)\epsilon_c = \sum_{i=1}^{\infty} K_{iz,i}(T_e)\epsilon_{iz,i} + \sum_{i=1}^{\infty} K_{exc,i}(T_e)\epsilon_{exc,i} + \frac{3m_e}{m_i} K_{el} T_e. \tag{2.40}$$

In this expression K_{iz} is the volumetric ionization rate, K_{exc} is the volumetric excitation rate, K_{el} is the elastic scattering rate, ϵ_{iz} is the ionization energy, ϵ_{exc} is the

excitation energy, and i is the state index. Both the ionization and excitation rates are functions of electron temperature. Note that the ion cost exceeds the ionization energy due to the presence of excited states that absorb a portion of the absorbed energy.

The power entering the nozzle is then the sum of (2.36) - (2.39):

$$P_{noz} = \left[\frac{1}{2}m_i u_0^2 + \frac{5}{2}qT_{e,0} + \frac{3}{2}qT_{e,0}\left(\frac{5/3-\gamma}{\gamma-1}\right) + q\epsilon_c\right] n_{e,0}u_0 A_0. \tag{2.41}$$

Note that the first term on the right hand side of this equation is the ion kinetic energy, the second is the plasma pressure, the third is the heat conduction, and the fourth is the ion production costs.

Combining the nozzle efficiency (Eq. 2.34), the thrust (2.24), and the ion mass flow rate (Eq. 2.26) while leveraging the definition of the Mach number (Eq. 2.8) to simplify the expression yields the theoretical nozzle efficiency:

$$\eta_{noz,t} = \frac{M^2\gamma T_{e,d}}{[5+\gamma+3\left(\frac{5/3-\gamma}{\gamma-1}\right)+\frac{2\epsilon_c}{T_{e,0}}]T_{e,0}}\eta_{div}. \tag{2.42}$$

Note that in this expression $M = u_d/\sqrt{\gamma q T_{e,d}/m_i}$ denotes the ion Mach number at the detachment plane. This form of the nozzle efficiency is composed of terms that are directly measurable plasma properties or inferred from these properties. This nozzle efficiency expression can be used in two ways: in conjunction with plasma measurements or the ideal expansion can be analytically predicted. A control volume analysis of the diverging magnetic nozzle section from the throat to the detachment plane can yield the latter. The combination of the continuity and the polytropic state equations, assuming no transverse losses across the vacuum interface lines, yields an expression for the electron temperature at the detachment plane

$$T_{e,d} = T_{e,0}\left(\frac{u_0 A_0}{u_d A_d}\right)^{\gamma-1}. \tag{2.43}$$

Similarly, via the momentum equation in the control volume analysis, the axial velocity at the detachment plane is given by

$$u_d^2 = u_0^2 + \frac{2\gamma q m_i T_{e,0}}{\gamma - 1}\left[1 - \left(\frac{u_0 A_0}{u_d A_d}\right)^{\gamma-1}\right]. \tag{2.44}$$

This latter expression is an implicit function for the detachment plane ion velocity, but can be solved numerically. These expressions formally relate the plasma expansion through the nozzle to the area expansion ratio. This is consistent with the gasdynamic nozzle formalism that we apply here. For clarity, the detachment plane is defined as the plane at which the plasma is no longer influenced by the magnetic nozzle. The identification of the physical mechansims that cause detachment is an open research question [83, 84, 86, 96, 97, 98, 147, 149, 152, 167]; as such, a self-consistent model does not yet exist. To circumvent this issue and close the above performance model, in this work the detachment plane coincides with the location at which the ion velocity plateaus — namely, where the ions are no longer being accelerated by the nozzle.

Note that all of the terms in Eq. 2.42 are either directly measurable or have been explicitly related to directly measurable quantities, except for the polytropic index. For completeness, we now formally establish the relationship between the polytropic index and the measurable plasma properties. Assuming that the plasma is steady and that the electron velocity vector is approximately aligned with the nozzle field lines, the collisionless Ohm's Law states that the electron pressure balances the electric field

$$\nabla p_e = e n_e \nabla \phi, \tag{2.45}$$

where ϕ is the plasma potential. These assumptions have been shown to be apprximately correct for a moderate power magnetic nozzle operating on argon [164]. If the electron temperature can be assumed to be constant this relation gives rise to the canonical Boltzmann relation that links the plasma potential to the plasma density:

$$n_e(\phi_2) = n_e(\phi_1) \exp\left[\frac{e(\phi_2 - \phi_1)}{kT_e}\right]. \tag{2.46}$$

However, in magnetic nozzles the plasma cannot be assumed to be isothermal — the electron fluid cools as it expands through the nozzle [164]. Loosening the isothermal assumption and manipulating Eq. 2.45 yields

$$\phi = \frac{\gamma k T_{e,0}}{e(\gamma - 1)} \left(\frac{n_e}{n_0}\right)^{\gamma - 1}, \tag{2.47}$$

and

$$\phi = \frac{k}{e}\left(\frac{\gamma T_e}{\gamma - 1} - T_{e,0}\right). \tag{2.48}$$

Here, the polytropic index (γ) can be determined from measurable plasma properties by taking the derivative of each of these equations with respect to n_e and T_e. In our analysis we primarily use the derivative of Eq. 2.48 with respect to T_e (rearranged to solve for γ):

$$\gamma = \frac{d\phi/dT_e}{d\phi/dT_e - 1}. \tag{2.49}$$

This form allows us to apply linear regression to the plasma potential and electron temperature data. This analysis technique enables us to use a larger fraction of the available data — compared to a point-by-point calculation using Eq. 2.48 — and estimate uncertainties in the polytropic cooling parameter through repeated fitting of the data.

We now have a general theoretical framework for the nozzle efficiency that is composed of measurable plasma properties. Later in this thesis we couple this framework with experimental measurements to quantify the performance of a low-power magnetic nozzle test article.

2.4 Source Efficiency and Power Deposition

In addition to the nozzle efficiency architecture outlined above, we can also develop a framework that can be used to predict the source efficiency of a low-power magnetic nozzle. In this section we strive to build this framework and manipulate it into a form that can be used in conjunction with experimental measurements. Fundamentally, we must start with the broad definition of source efficiency (Eq. 2.32) and derive expressions for the various terms. We already have an expression for the power flowing into the diverging nozzle section (Eq. 2.41), so we focus on the deposited power here.

Using a cylindrical control volume analysis of the plasma liner, the deposited power must be balanced by the sum of the power incident on each surface (back wall, radial, and entering the diverging nozzle section). The power on the back wall is comprised of the same terms as the nozzle power,

$$P_{bw} = P_v + P_p + P_Q + P_c. \tag{2.50}$$

While the form may be the same, it is possible that the plasma properties differ between the back wall and the nozzle boundaries. However, it is difficult to make direct measurements of the plasma within the plasma liner region without perturbing the plasma [168, 169] to ascertain the exact properties variations between these two boundaries. Lafleur [94] overcomes this difficulty by assuming that the plasma density is the same and that the ions are sonic at both boundaries. The primary difference between the energy fluxes at both boundaries is that the nozzle boundary includes electron heat conduction. This term is absent in the back wall formulation. However, upon examining the terms in Eq. 2.50 in detail, it is clear that for low electron temperature devices the ion production cost (P_c) is the dominant power term, often by a few orders of magnitude. If we combine this with the assumption that the electron

temperature is approximately constant within the source region, the power incident on the back wall and the power entering the nozzle can be estimated as approximately equal ($P_{bw} \approx P_{noz}$). This result is consistent with model results published by Lafleur [94].

The remaining boundary is the radial surface. If we assume that the plasma is collisionless, that the electrons are fully magnetized, and that the magnetic field lines are axially-aligned, then only the ion species can impinge on the radial walls. The energy within the ion species is comprised of the ion kinetic energy and the ion production cost, so we can write

$$P_r = P_{v,r} + P_{c,r}, \tag{2.51}$$

where the subscript r denotes the radial component. We can write the general form for the radial ion kinetic energy as

$$P_{v,r} = \int_0^L 2\pi m_i n(z, R_s) u_{i,r}^3 R_s dz, \tag{2.52}$$

where L is the length of the cylindrical plasma liner, R is the radius of the plasma liner, $n(z, R)$ is the axial variation in the plasma density adjacent to the liner walls, and z is the axial coordinate. Likewise, the ion production cost that is carried with the radial ion motion is

$$P_{c,r} = \int_0^L 2\pi q n(z, R_s) \epsilon_c u_{i,r} R_s dz. \tag{2.53}$$

In order to evaluate this expression we need to determine the radial ion velocity ($u_{i,r}$). For the source tube wall, this value is the Bohm speed, but the radial ion velocity can also be spatially mapped across the source tube using measurements. Due to the small nature of many low-power magnetic nozzle devices and the possibility

of perturbing the device operation direct measurement of the radial ion velocity is difficult. However, leveraging 2.11 for a cold plasma, using cylindrical axisymmetry ($\partial/\partial\theta = 0$), referencing the geometry to the throat, and eliminating the electric field we can write the general component momentum equations throughout the plume:

$$u_{i,z}\frac{\partial u_{i,z}}{\partial z} + u_{i,r}\frac{\partial u_{i,z}}{\partial r} + \frac{c_s^2}{n}\frac{\partial n}{\partial z} = -(u_{i,\theta} - u_{e,\theta})B_r \tag{2.54}$$

and

$$u_{i,z}\frac{\partial u_{i,r}}{\partial z} + u_{i,r}\frac{\partial u_{i,r}}{\partial r} + \frac{c_s^2}{n}\frac{\partial n}{\partial r} = (u_{i,\theta} - u_{e,\theta})B_z + \frac{u_{i,\theta}^2}{r}. \tag{2.55}$$

Here B_r is the radial magnetic field component, B_z is the axial magnetic field component, and $u_{i,\theta}$ and $u_{e,\theta}$ are the ion and electron swirl velocities, respectively. While these equations appear to introduce more degrees of freedom (the swirl velocities and magnetic field) we can eliminate these variables by assuming that the magnetic field is approximately axial within the plasma liner ($B_r \approx 0$). This allows us to rearrange Eq. 2.54 to solve for the radial ion velocity:

$$u_{i,r} = -\left(u_{i,z}\frac{\partial u_{i,z}}{\partial z} + \frac{c_s^2}{n}\frac{\partial n}{\partial z}\right)/\frac{\partial u_{i,z}}{\partial r}. \tag{2.56}$$

Note that this form is comprised of measurable properties - even the gradients if we make spatial measurements. After solving for the radial ion velocity using experimental measurements we can solve for the radial power losses using Eqs. 2.51 - 2.53 if we assume that the plasma profiles within the source region are self-similar. This allows us to evaluate the source efficiency as

$$\eta_{loss} = \frac{P_{noz}}{2P_{noz} + P_{v,r} + P_{c,r}}. \tag{2.57}$$

Interestingly, we can also estimate the power deposition as a function of radius

using the principles outlined above if we decompose the cylindrical source region into cylindrical shell control volumes, as shown in Figure 2.4. If a large number of partitions are used, the plasma properties can be radially averaged in each shell, thereby simplifying the P_{noz} equations. In each shell the deposited power must still be equal to the sum of the power incident on all boundaries; we must simply account for the n and $n-1$ radial boundaries. Thus, the estimate deposited power within the cylindrical shell becomes

$$P_{dep_n} = 2P_{noz_n} + P_{v,r_n} + P_{c,r_n} + P_{v,r_{n-1}} + P_{c,r_{n-1}}. \tag{2.58}$$

Note that power flowing from one shell into another is a signed term; the sign of the radial velocity component can make these terms positive or negative. Power flowing into a shell reduces the total deposited power into that layer by the amount of influx. Likewise, it is important to note that the limits on the P_{noz} terms are modified - they are $[r_{n-1}, r_n]$ rather than the original $[0, R_s]$. While this estimated radial power deposition may not be as accurate as a full 2D power deposition and antenna radiation model it does provide a useful analysis tool that we can couple with experimental measurements.

2.5 Divergence Efficiency

While our quasi-1D nozzle efficiency model (derived in the Section 2.3) provides a simple, useful framework, it has a major limitation: it does not capture radial information due to the area-slice averaging throughout the nozzle. This limitation is inherent to quasi-1D models and makes it difficult to track the momentum vectors throughout the nozzle. Therefore, it is difficult to predict the divergence efficiency using such a model because, by definition, the divergence efficiency can only be determined if radial velocity information is available. As such, in this section we strive

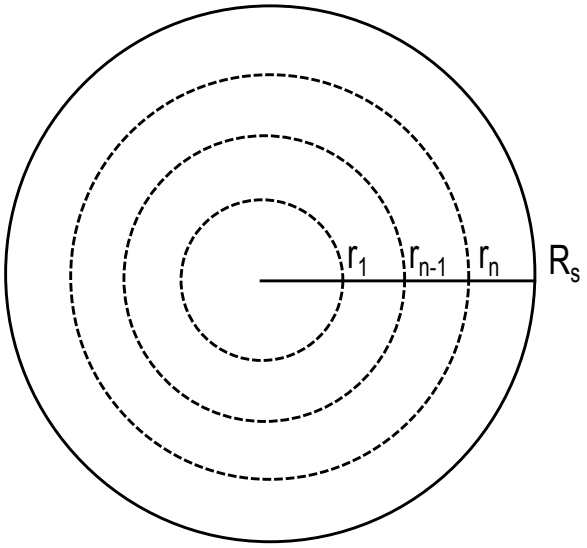

Figure 2.4: A notional splitting of the cylindrical source control volume into cylindrical shell control volumes to estimate the radial power deposition.

to loosen the quasi-1D averaging assumption, by incorporating the measured radial plasma density profile at the throat, to allow us to predicted the expected divergence efficiency.

As the basis for this model we assume that the diverging magnetic nozzle section can be approximated by the magnetic topography generated by a current loop. Leveraging the analytical work by Simpson, et. al. for a single current loop [170] the magnetic field components can be written as

$$B_r = \frac{\mu_0 I z}{2\pi\alpha_m^2\beta_m r}\left[(a_m^2 + r^2 + z^2)E(k^2) - \alpha_m^2 K(k_m^2)\right], \tag{2.59}$$

$$B_z = \frac{\mu_0 I}{2\pi\alpha_m^2\beta_m}\left[(a_m^2 - r^2 - z^2)E(k^2) + \alpha_m^2 K(k_m^2)\right], \tag{2.60}$$

$$\alpha_m^2 = a_m^2 + r^2 + z^2 - 2a_m r, \tag{2.61}$$

$$\beta_m^2 = a_m^2 + r^2 + z^2 + 2a_m r, \tag{2.62}$$

and

$$k_m^2 = 1 - \frac{\alpha_m^2}{\beta_m^2}. \tag{2.63}$$

Here B_r is the radial magnetic field, B_z is the axial magnetic field, μ_0 is the vacuum permeability, a_m is the magnet radius, and I is the coil current. The entirety of the magnetic nozzle can be defined by iteratively solving these equations. The model parameters were tuned to match our experimentally measured nozzle profile.

As done by Little [152], if the plume expansion can be assumed to be collisionless and perfectly attached to the nozzle streamlines up to the detachment point the diverging nozzle section to be transformed into magnetic coordinates - the local coordinate vectors are parallel ($\hat{\psi}$) and perpendicular ($\hat{\xi}$) to the magnetic streamlines - while retaining the advantages of a quasi-1D model. The first term in the Taylor expansions of Eqs. 2.59 and 2.60 and the appropriate derivatives to determine the streamfunction yields the (r, z) to (ψ, ξ) transformation:

$$\psi = \frac{(r/a_m)^2/2}{[1 + (r/a_m)^2 + (z/a_m)^2]^{3/2}} \tag{2.64}$$

and

$$\xi = \frac{(z/a_m)/2}{\left[(r/a_m)^2 + (z/a_m)^2\right]^{3/2}}, \tag{2.65}$$

where $\xi(r, z)$ holds for $(z/a_m) > 1$.

At the nozzle throat the streamlines are parallel to $\hat{z}$ allowing for a simple coordinate transformation of the measured density profiles from $n(r)$ to $n(\psi)$. Due to our assumptions of self-similarity and perfect attachment to the nozzle streamlines

the $n(\psi)$ profile is valid up to the detachment point and the local velocity vector is tangent to the nozzle streamlines. This allows the total momentum to be defined as

$$p_T = 2\pi \int_0^{\psi_v} n(\psi)\langle v \rangle r d\psi \tag{2.66}$$

and the axial momentum as

$$p_z = 2\pi \int_0^{\psi_v} n(\psi)\langle v \rangle_z r d\psi, \tag{2.67}$$

where $\langle v \rangle$ is the average velocity determined from the quasi-1D analysis and ψ_v is the vacuum-interface streamline that grazes the source tube wall. The divergence efficiency is then

$$\eta_{div} = \frac{p_z^2}{p_T^2}. \tag{2.68}$$

We now have a model, albeit one that generally must be solved numerically, to predict divergence efficiency using the same measurements (primarily density and velocity) as the quasi-1D nozzle efficiency model. Due to the inclusion of radial information and the loosening of the property averaging across the area-slice of the nozzle this model yields a more accurate efficiency prediction than the cylindrical quasi-1D model alone. Upon examination of Eqs. 2.66 and 2.67 the density profile shape impacts the divergence efficiency performance; if the density profile is non-ideal (concentrated off-centerline) a greater portion of the velocity is directed radially due to the higher divergence of the nozzle streamlines away from centerline. This suggests that we can use this model to examine thruster architectures that generate discharges with non-ideal density concentrations and assess the performance impact.

2.6 Summary

In this chapter, we have demonstrated that magnetic nozzle performance can be evaluated through the lens of gasdynamic nozzles. We have derived expressions for low power magnetic nozzle performance parameters by leveraging existing efficiency architectures for electric thrusters and models for moderate power magnetic nozzles. We now have a theoretical framework for device performance that is composed of measurable plasma quantities. In the remainder of this thesis we seek to combine this framework with experimental investigations of a low-power magnetic nozzle test article to examine the physical mechanisms present in these devices in detail and elucidate their impact on performance.

CHAPTER III

Experimental Setup and Diagnostics

The goal of the experimental investigation is to identify non-ideal effects present within low-power magnetic nozzles and to explore how these effects impact thrust performance of these devices. In this chapter, we describe a low-power magnetic nozzle test article that is designed to achieve this end by allowing for a wide range of operating conditions. In Section 3.1 we detail the vacuum facilities used to conduct this experiment investigation. In Section 3.2 we provide a schematic of the various plasma source physical configurations, details on the magnetic nozzle, and describe the various operating modes of the plasma source. In Section 3.3 we describe the diagnostics used during the experiments. These include a Hall probe, Stabil-Ion Gauge, various electrostatic probes, and 2D time-averaged Laser Induced Fluorescence to measure the magnetic nozzle topology, neutral density, and properties of the plasma as it expands through the nozzle.

3.1 Vacuum Chamber

The experiments were conducted in the Junior Test Facility connected to the Large Vacuum Test Facility at the University of Michigan. Junior is a 3 meter long by 1 meter diameter stainless steel clad vacuum chamber backed by a turbopump and a cryopump nominally rated at 800 and $38,000$ L/s on xenon, respectively. At rough

vacuum the pressure was measured at the wall using an MKS Series 979B Bayard-Alpert/MicroPirani-style Multi-Sensor Atmosphere to Vacuum Transducer integrated with an MKS PDR900$-$1 controller. At high vacuum the pressure was measured by a Varian 563 Bayard-Alpert hot cathode ion gauge and an Agilent XGS-600 Controller.

The measured background pressure of Junior without the cryopump was $\sim 5\times10^{-4}$ Torr when the experiment required propellant flow rates of 3 mg/s of xenon. At this background pressure, the ion-neutral charge exchange mean free path is $\sim$ 10 cm. To facilitate far-field plume measurements and reduce the presence of this effect within the plume, the Junior cryopump was operated for all the experiments discussed herein.

The effective pumping speed for these experiments was $\sim 15,000$ L/s on xenon due to the inclusion of a large hexagonal aluminum plate mounted to the cold head. To ensure that the plate could sustain a xenon pumping temperature of $\leq$ 45 K, a Multilayer Insulation blanket on the bottom of the plate limits the radiative heat transfer from the chamber walls. The temperature of the cold head and the edge of the plate was monitored in real-time using two LakeShore DT-670 Silicon Diode temperature sensors connected to a LakeShore Model 224 Temperature Monitors. With this pumping capacity Junior was capable of achieving base pressures of $\sim 1\times10^{-8}$ Torr and a background pressure of $\sim 4\times10^{-5}$ Torr during the nozzle source operation at neutral flow rates up to 3 mg/s of xenon. Figure 3.1 is a photo of this facility.

3.2 Magnetic Nozzle Plasma Source

The plasma source is a flexible testbed magnetic nozzle source designed to investigate the phenomena and underlying physics present in low-power magnetic nozzle operation. It is $\sim$ 13 cm in diameter and can integrate plasma liners up to 3 cm in diameter. This compactness enables us to use smaller vacuum facilities without the diverging nozzle field lines intersecting the facility walls near the source. The di-

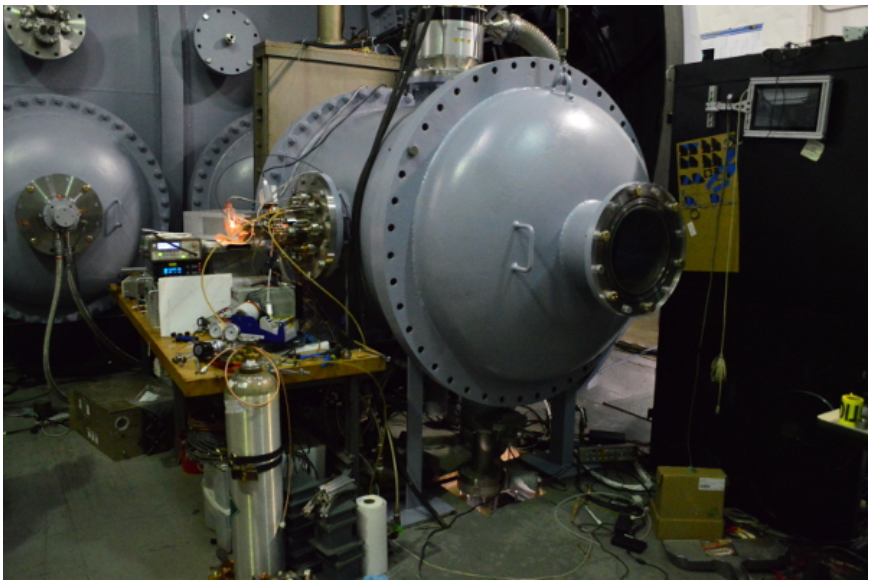

Figure 3.1: A photograph of the Junior vacuum test facility at the University of Michigan.

verging magnetic nozzle section is generated by a 149-turn solenoid constructed of 10 AWG square, enamel-coated copper magnet wire. In this configuration the solenoid is capable of producing peak axial magnetic fields of up to $\sim$ 900 G. The coil current is driven by an external Sorenson DCS 33-33 DC laboratory power supply. The radio frequency (RF) power is generated external to the facility by a Agilent 33220A signal generator and an Ophir 5087Q RF amplifier. Our experiments operated in the 13 - 14 MHz range, based on if frequency tuning was used. To minimize the reflected power an RF Plasma Products, Inc. AMNS-3000E L-type matching network matches the antenna load to the source load. Both the RF antenna and the electromagnet spool are open-loop water cooled to dissipate heat and maintain maximum steady-state operating temperatures below the maximum source operating temperature of 240 °C. Finally, the propellant is fed to the plasma source from an external reservoir. A Faraday enclosure surrounds the liner and antenna to reduce stray RF signal propagation throughout the chamber, with openings for connections and the plasma expanding through the magnetic nozzle.

In this research we used three distinct source configurations: 1) a solenoidal antenna configuration with an external RF matching network, 2) a solenoidal antenna configuration with an internal RF matching network, and 3) a planar antenna configuration with an internal RF matching network. The latter two configurations are designed to improve power coupling to the plasma by minimizing the transmission line length distortion of the load impedance.

3.2.1 Solenoidal Antenna Configuration

Based on previous findings [94, 150, 171] suggesting that limiting source wall losses is critical to enhancing overall performance, we chose to integrate a quartz plasma liner with a diameter of 2.5 cm (external matching network configuration) or 1.9 cm (internal matching network configuration) and a length of 1.9 cm. In both configurations a 3-turn solenoidal antenna is wrapped around the quartz liner, such that the antenna is slip-fit to the outer diameter of the plasma liner. The antenna is made of thin-walled 3.2 mm diameter copper tubing to facilitate open-loop water cooling to minimize impedance changes due to thermal effects. A notional diagram of the source in the solenoidal configuration can be found in Figure 3.2. A photograph of this configuration installed in the Junior Test Facility can be found in Figure 3.3; for clarity and further detail, a 3D rendering of the plasma source in the 2.5 cm solenoidal antenna configuration is shown in Figure 3.4. Source operation in these solenoidal configurations were repeatable and demonstrated stable operation exceeding 200 cumulative hours with deviations of less than 1% in the steady state net deposited power and temperature telemetry over the duration of operation.

3.2.2 Planar Antenna Configuration

In the planar antenna configuration, the baseline test device (depicted in Figure 3.4) was used, but the quartz plasma liner is replaced with a boron nitride plasma

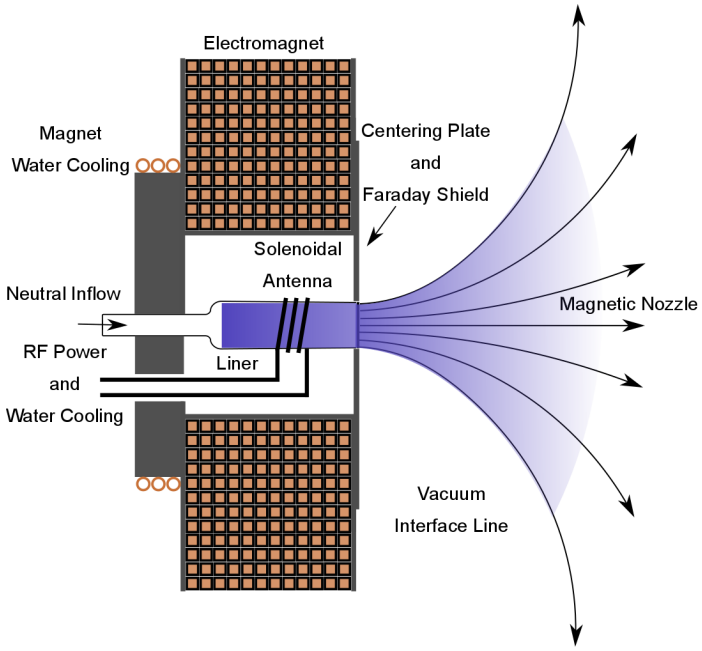

Figure 3.2: A notional diagram of the plasma source in the solenoidal antenna configurations.

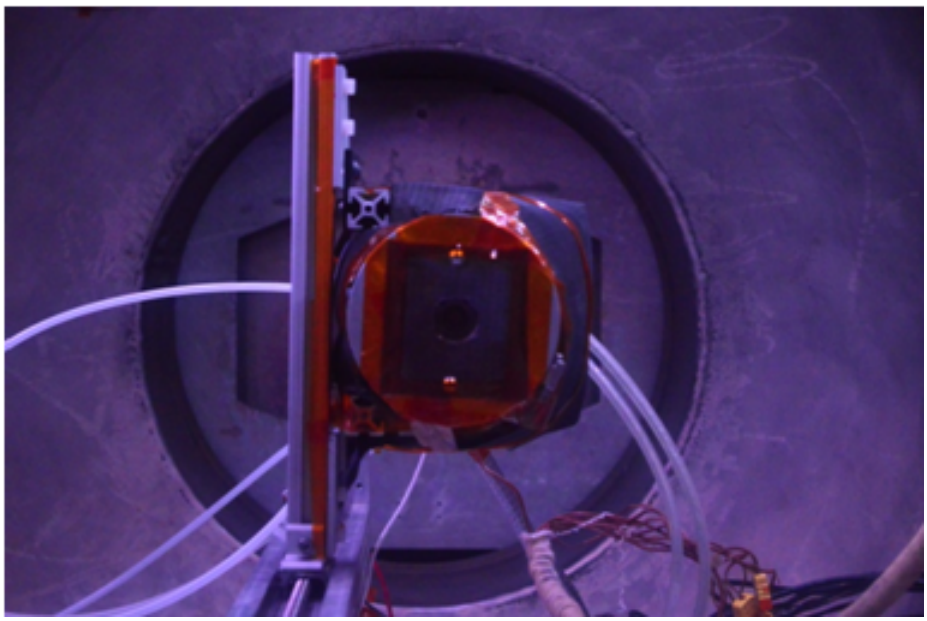

Figure 3.3: A photograph of the solenoidal antenna test configuration installed in the Junior Test Facility.

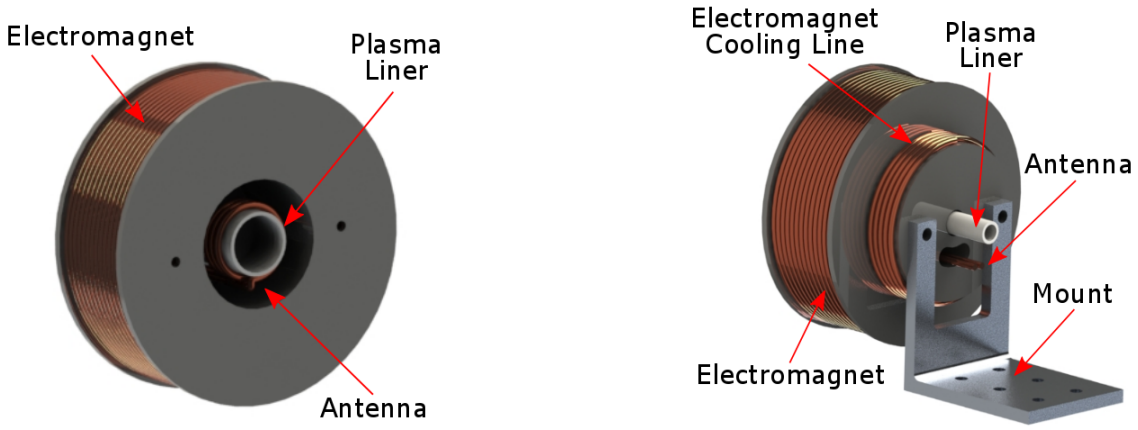

(a) (b)

Figure 3.4: a) A rendered front view of the testbed device, minus the front Faraday plate that prevents stray RF leaking into the plume and centers the plasma liner. b) A rendered rear view of the device.

liner that is 3.8 cm in diameter and 2.7 cm in length. A 3-turn spiral planar antenna comprised of the thin-wall copper tubing described above is affixed to the backplane of the boron nitride plasma liner. A notional diagram of this configuration is provided in Figure 3.5.

3.2.3 Magnetic Nozzle

While the source electromagnet was capable of producing a peak throat strength of up to 900 G, the experiments detailed within this work did not exceed a throat strength of 600 G. To verify the electromagnet operation, the magnetic field was mapped using a 3-axis gaussmeter (all diagnostics are detailed in the next section). The linear relationship between current input to the electromagnet and the throat strength, in Figure 3.6a, and the centerline decay of the field strength downstream of the throat, in Figure 3.6b, is quantified by centerline measurements. A 2D map of the diverging nozzle section confirms that nozzle is approximately axisymmetric, as shown in Figure 3.7. The slight nozzle field line deflections in the $-\hat{r}$ direction are attributed to small asymmetries in the electromagnet and the fact that the process

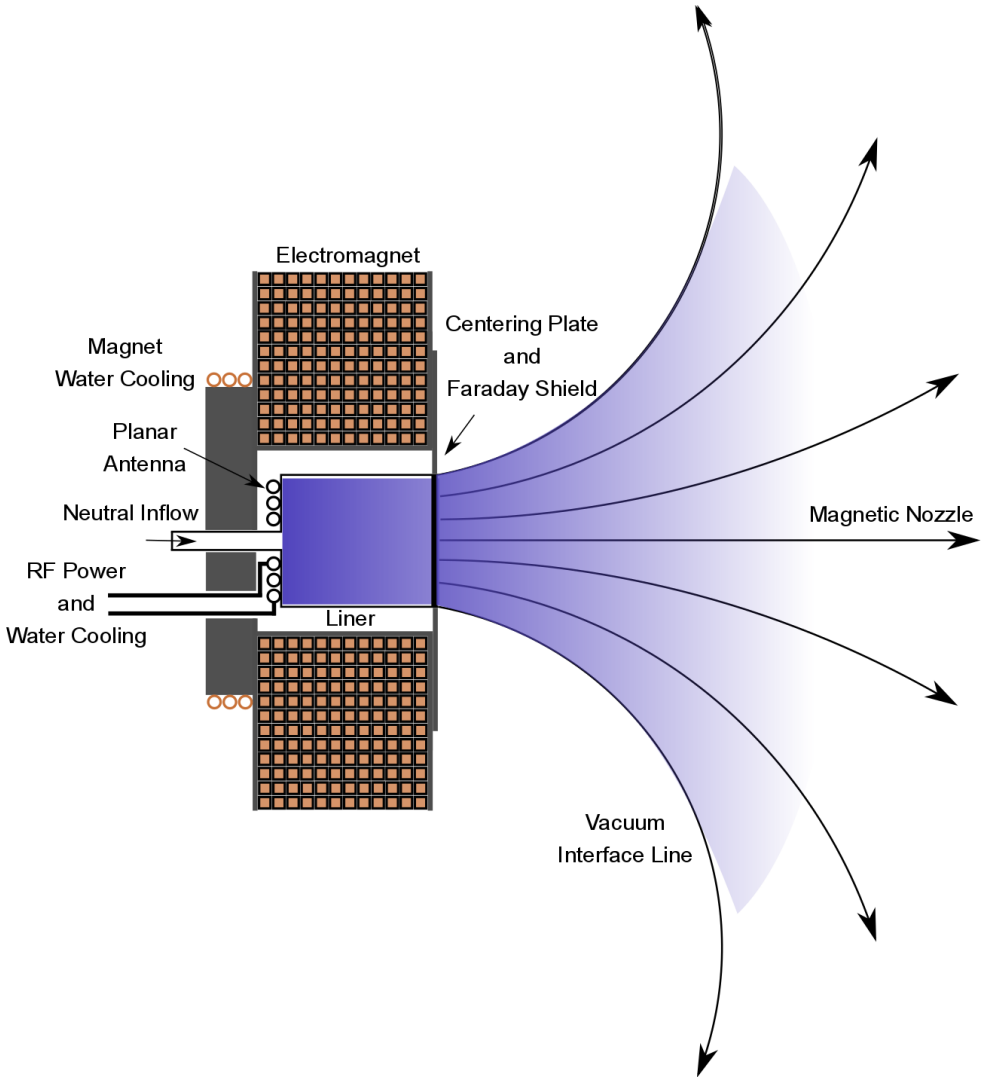

Figure 3.5: A notional diagram of the source in the planar antenna configuration.

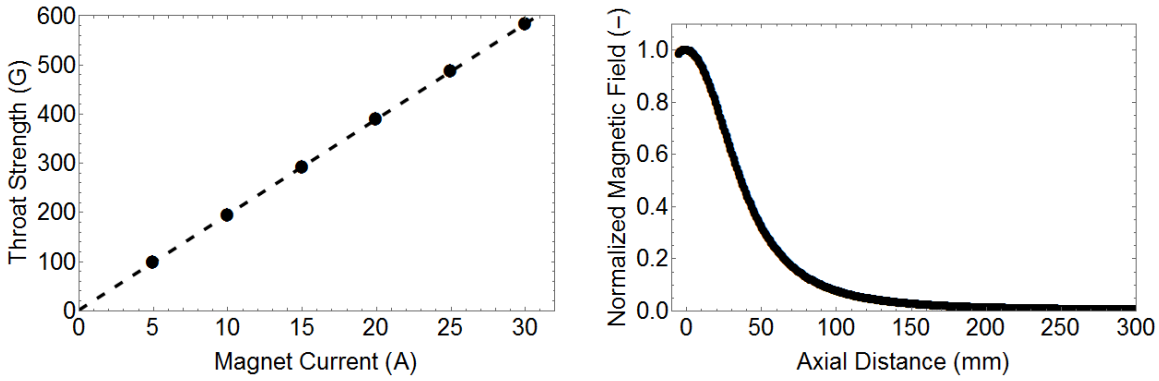

(a) (b)

Figure 3.6: a) The measured nozzle throat magnetic field strength as a function of the magnet current. b) The measured nozzle centerline magnetic field strength normalized by the throat strength.

of winding the electromagnet results in coil layers that are slightly helical in nature, rather than the perfectly flat and aligned layers depicted in the notional diagrams in Figures 3.2 and 3.5.

3.2.4 Operating Modes

We found the testbed article to operate in two distinct modes - "ring discharge" and "Gaussian" - depending on the RF antenna configuration, applied power, magnetic field strength, and injected xenon mass flow rate. The "ring discharge" mode is qualitatively characterized by the formation of a visible bright ring, as viewed axially down the centerline (refer to Figure 3.8), within the plasma liner. We only observed this mode when the plasma source was in a solenoidal antenna configuration. From a side view of the plasma source operating in this condition (Figure 3.8b), we observed visible, bright zones near the vacuum-interface field line as the plasma expanded away from the plasma source. We did not observe this qualitative feature in the "Gaussian" mode - only observed in the planar configuration and at very low powers in the solenoidal antenna configurations - as illustrated by the photograph in Figure 3.9.

While we observed qualitative distinctions between the two operating modes, these qualitative results were corroborated by electrostatic probe measurements (these diagnostics are detailed in the next section). As we demonstrate in Figure 3.10, when

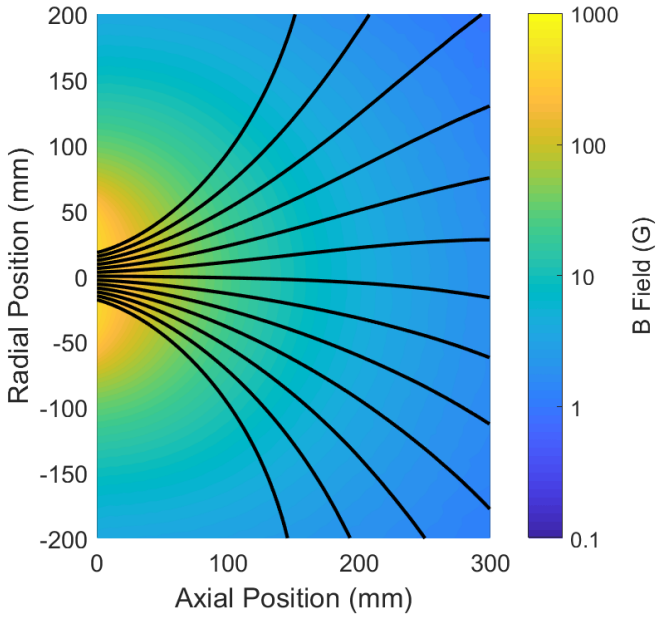

Figure 3.7: The measured nozzle topology at the 30 A magnet current condition. In the far field the nozzle streamlines deflect in the $-\hat{r}$ direction due to small asymmetries in the magnet construction. This general nozzle topology is consistent across all operating conditions.

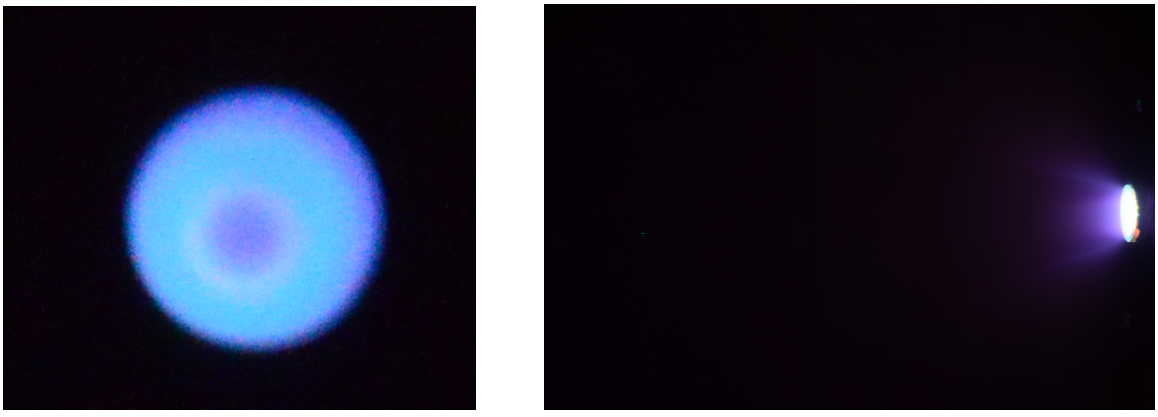

(a) (b)

Figure 3.8: a) A front view and b) side view photograph of the source operating at 400 G in the 1.9 cm solenoidal antenna configuration.

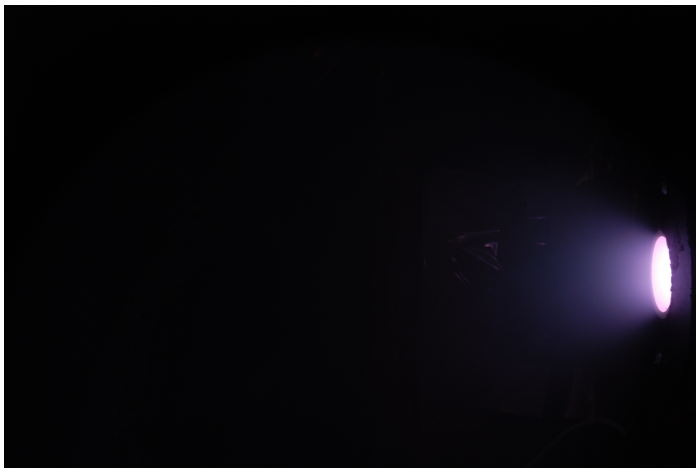

Figure 3.9: A photograph of the source operating at 600 G in the planar antenna configuration.

the source is operating in a "ring discharge" mode a dip in centerline plasma density and increase in the density at the radial wall is observed. Note that we choose to normalize the plasma density profiles in this figure to more clearly illustrate the radial profile changes; in these operating conditions there were variations in the maximum plasma density measured as a function of the magnetic field strength. These variations are attributed to the quality of the plasma-antenna power coupling. As we increased the magnetic field strength the centerline centerline density depression became greater. Similarly, the density at the radial wall is enhanced. These results are consistent with modeling results of magnetically enhanced inductively coupled plasmas commonly used in plasma processing applications; these results capture spatially non-uniform power deposition in both solenoidal and helicon antennae configurations when a critical magnetic field threshold is achieved [165, 166]. While the critical magnetic field is dependent on plasma species, source and antenna geometry, magnetic topology, and dominant power coupling mechanisms, it can drop into the 10-100s of Gauss range [165, 166], which overlaps with our magnetic operating conditions. Estimation of the skin depth — a small region into which the bulk of the power is deposited — for these conditions show that the skin depth decreases from ~ 1 cm to

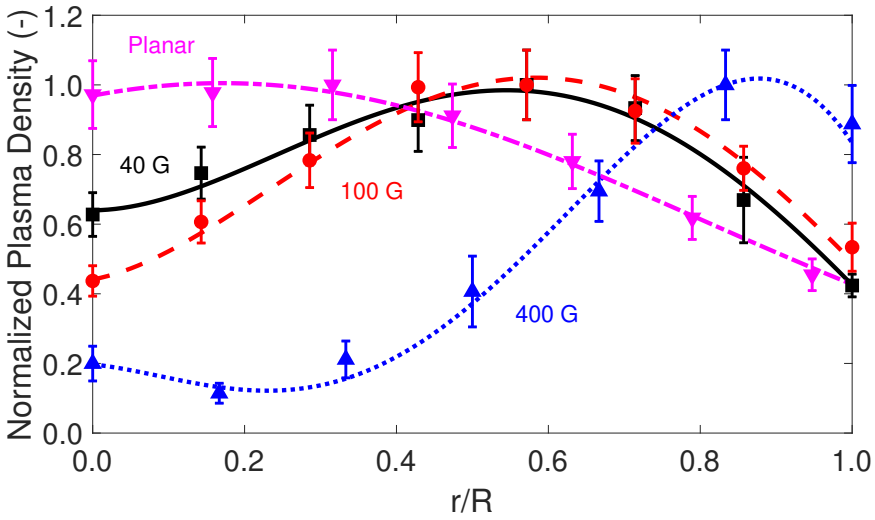

Figure 3.10: A comparison of the density at the source exit plane for the 40 G (solid curve/squares), 100 G (dashed curve/circles), and 400 G (dotted curve/triangles) source operating conditions in the internal matching network solenoidal antenna configuration and the 600 G planar antenna configuration (dashed-dotted curve/inverted triangles). All conditions were operated at a net deposited power of $\sim$ 170 W and the propellant flow rate was set to 0.5 and 0.25 mg/s xenon for the solenoidal and planar antenna configurations, respectively. These measurements were made using the double Langmuir probe detailed in Section 3.3.

$\sim$ 1 mm with our increasing magnetic field conditions, further suggesting that this structure is arises from the power coupling.

Conversely, in the "Gaussian" operating mode the density profile is more consistent with those observed in other magnetic nozzle devices [77, 83, 94, 95, 147, 149, 159] and a planar antenna-driven magnetically enhanced inductively coupled plasma source designed for electric propulsion [172]. As observed in Figure 3.10 this mode has a predominantly center-peaked plasma density profile, across all magnetic field operating conditions. This trend runs counter to the "ring discharge" results outlined above.

In both operating modes of the plasma source, the initial plasma ignition resulted in a steady, dim discharge with $T_e \sim 1-5$ eV, $n_e \sim 10^{14}-10^{15}$ m^{-3}, and forward power of $\sim$ 50 W. This initial ignition often required an increased propellant flow rate ($3-5$

mg/s of xenon), followed by a gradual decrease in the propellant flow rate to the final operating condition. The above reported plasma parameters are representative of the steady discharge at the final flow rate condition. These qualitative and quantitative observations are consistent with characteristics of a capacitively coupled plasma [83, 122, 173, 174, 175]. After the flow rate was set to the final operating setting, the power could be increased. As we increased the power to ~ 120 W forward power, we observed a shift in brightness of the plume and an impedance mismatch that had to be corrected by the matching network. In the "ring discharge" mode, this is when the bright ring became visible. After we tuned the match parameters, the steady, bright discharge plasma characteristics were $T_e \sim 5 - 10$ eV and $n_e \sim 10^{16} - 10^{17}$ m^{-3}. After tuning the match parameters we increased the power to the final operating setting and made final adjustments to the match to minimize the reflected power - often below 20% of the forward power. Throughout the entire start-up process the magnetic field setting was applied, and kept constant. While these observed characteristics are consistent with a shift from capactively to inductively coupled plasmas [83, 122, 173, 174, 175, 176, 177, 178], we do not have the power telemetry to confirm how the source was coupling power.

For all experiments reported herein, unless otherwise noted, we operated the plasma source at a net deposited power of ~ 170 W and varied the antenna geometry. In each antenna configuration (large solenoidal, small solenoidal, and planar) we kept the flow rate constant (3, 0.5, and 0.25 mg/s of xenon, respectively) and varied the magnetic field strength.

3.3 Plasma Diagnostics

3.3.1 3-Axis Hall Probe

The magnetic field topology of the magnetic nozzle testbed source is mapped using a 3-axis Hall probe and a Lakeshore Model 460 Gaussmeter. The Hall probe is mounted at the end of a 25.4 cm stem and is capable of measuring magnetic fields up to 3 kG in each axis. During the mapping process, the Hall probe was mounted to three Velmex linear translation stages with a 30 cm vertical and longitudinal throw and a 40 cm transverse range. These stages are orthogonally aligned and mounted to an optical table. The magnetic nozzle source is mounted to the same optical table and then aligned to the stages. The final source-probe alignment is done using a combination of light reflection from a mirror mounted to the source and using features of the thruster, such as the exit diameter and the front face, to center the probe with the thruster centerline at the exit plane. An automated, custom LabVIEW VI accepts a user-specified measurement location data file and controls the stage motion, gaussmeter polling, and the data logging. A settling time of 2 seconds at each measurement location is built in to yield accurate, stable probe measurements. The 2.08 mm offset of the radial Hall sensor is corrected by an additional probe movement and sample at each specified grid location. To account for the magnetic field of the Earth an additional map is measured after the electromagnet is turned off or - in the case of permanent magnets - the thruster is removed. This map is subtracted from the initial nozzle map to yield the nozzle streamlines.

3.3.2 Stabil-Ion Gauge

The neutral pressure distribution within the plume is measured with a MKS 370 Stabil-Ion Bayard-Alpert Vacuum Gauge that is calibrated on xenon. To increase spatial resolution and eliminate measurement error due to the neutral gas flow velocity

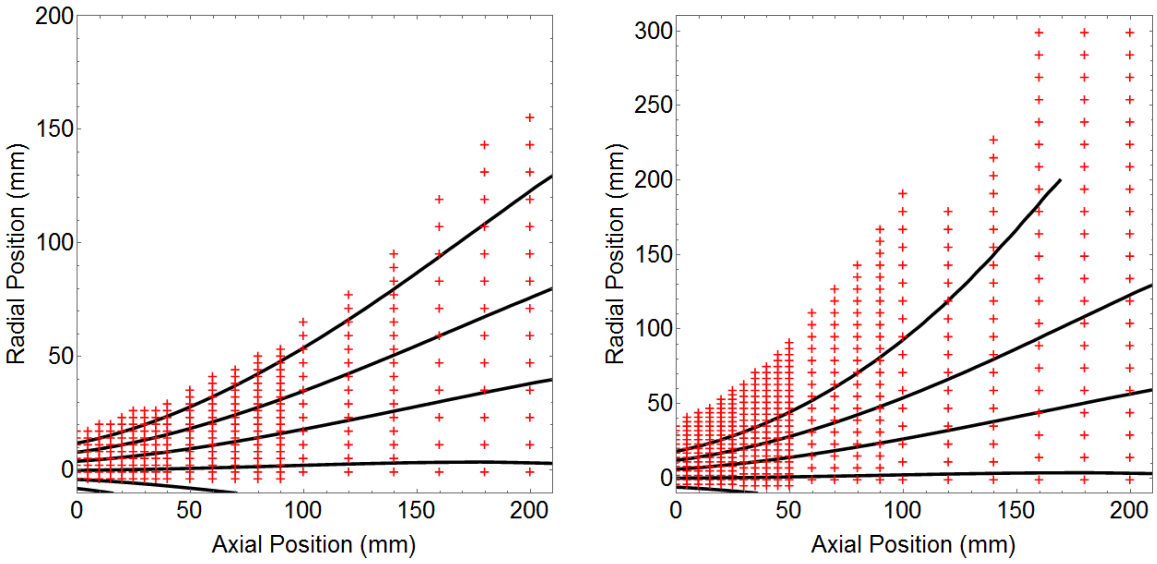

(a) (b)

Figure 3.11: The neutral pressure measurement locations (center of the crosses) throughout the plume of the plasma source a) solenoidal antenna configurations and b) planar configuration with an overlay of the nozzle field lines (curves).

a 3.2 mm diameter Pitot probe is connected to the $2 - 3/4$" Conflat connection on the Stabil gauge. To accommodate the size of the Stabil gauge relative to the nozzle source diameter, the Pitot probe was constructed in an L-shape with a length of 15.2 cm and height of 10.2 cm. To correct for the pressure drop across the Pitot tube, the Pitot tube is removed and the gauge is placed downstream of the device and pressure measurements are made at various propellant flow rates. The Pitot tube is then replaced and the measurements are repeated at the same flow rates. This process characterizes the pressure drop, allowing the measurements with the Pitot tube to be corrected. Figure 3.11 details the measurement locations for the solenoidal and planar antenna configurations of the testbed article.

The MKS 370 controller communicates with the DAQ via RS-232 to log the pressure data. Prior to starting the automated move-acquire process, the Stabil gauge was turned on and allowed to warm up for an hour to remove moisture within the Pitot tube and reduce measurement error. Due to the low conductance of the Pitot probe the settling time is set to 100 seconds at each measurement location to provide

a stable pressure reading.

3.3.3 Double Langmuir Probe

For this testbed device, which operates at 1s to 10s of MHz, electrostatic probes that reference ground require RF compensation to avoid distortion of the measured I-V traces [179, 180, 181, 182, 183, 184, 185]. However, RF compensation adds complexity to the circuit, is often designed for a single operating frequency, and results in a large probe. Due to the frequency tuning used during source operation and the small sizes of these nozzle sources RF compensation was not attempted. To circumvent this issue, we used a floating planar double Langmuir probe (DP) to extract plasma density and electron temperature profiles throughout the plume. In this probe configuration (see Figure 3.12), a bias is applied between the two probe tips and both tips are allowed to follow the local RF-driven potential oscillations. If these potential oscillations are small this scheme minimizes the RF-induced distortion effects on the measured I-V trace [186, 187, 188, 189, 190, 191].

To extract plasma parameters from the measured I-V trace we follow the methods outlined by Brockhaus et. al. [192]. If the plasma is assumed to be Maxwellian the I-V trace fits a hyperbolic tangent function dependent on the plasma density and electron temperature, thereby allowing these properties to be extracted. Note that this measurement technique does not allow the probe to enter electron saturation, so the plasma potential cannot be extracted from the trace. For completeness, the theory used during data analysis is highlighted here; for a more complete derivation refer to Refs. [192, 193, 194]. The first step in the analysis is determining if the probe is operating in a thin- or thick-sheath regime by comparing the characteristic probe length (ℓ_p) to Debye length (λ_D). The Debye length characterizes the distance over which a plasma screen electric potentials and the sheath around a surface has been shown to be several Debye lengths thick [122]. The Debye length is defined as

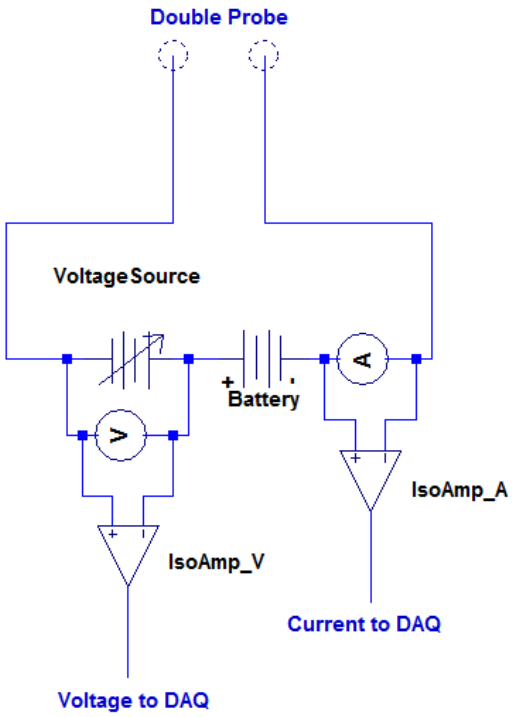

Figure 3.12: The general electrical circuit for a double Langmuir probe.

$$\lambda_D = \sqrt{\frac{\epsilon_0 k T_e}{n_e q^2}}, \tag{3.1}$$

where ϵ_0 is the vacuum permittivity of free space. In the thin-sheath limit ($\ell_p \gg \lambda_D$) the collected double probe current can be shown to be

$$I = I_\infty \tanh\left(\frac{qV}{2kT_e}\right), \tag{3.2}$$

where V is the probe bias and I_∞ is the saturation current, defined as

$$I_\infty = q n_i A_p \sqrt{\frac{kT_e}{2\pi m_i}}. \tag{3.3}$$

Here n_i is the ion density and A_p is the probe area. By taking the second derivative of this equation and using the extrema of the results, we can recover a simple expression for the electron temperature:

$$kT_e = \frac{q\Delta V}{\ln\left[(2+\sqrt{3})/(2-\sqrt{3})\right]}, \tag{3.4}$$

where ΔV is the voltage difference between the extrema. Using this result, the I-V trace data can be fit with the hyperbolic tangent function in Eq. 3.2 to yield the ion density. If the assumption of quasineutrality holds, the ion density is equal to the electron density and can be simply called the plasma density.

If the probe is operating in the thick-sheath regime ($\ell_p \ll \lambda_D$) then a series of corrections must be applied. The end results takes the form of

$$I(\psi) = I_\infty \frac{j_{11}\exp(\psi/2) - j_{12}\exp(-\psi/2)}{\exp(\psi/2) - \exp(-\psi/2)}, \tag{3.5}$$

where ψ is the bias voltage normalized by the electron temperature, and j_{11} and j_{12} are correction factors. These correction factors are of the form

$$j_{11} = (\beta - \chi + \psi_1)^\alpha \tag{3.6}$$

and

$$j_{12} = (\beta - \chi - \psi_2)^\alpha. \tag{3.7}$$

Here α and β are correction parameters, χ is the dimensionless floating potential, and ψ_1 and ψ_2 are the dimensionless probe potentials relative to the floating potential. Note that, from the general double probe circuit in Figure 3.12, that $\psi_1 = \psi - \psi_2$. These parameters take the form of

$$\alpha = \frac{2.9}{\ln(\ell_p/\lambda_D) + 2.3} + 0.07\left(\frac{T_i}{T_e}\right)^{0.75} - 0.34, \tag{3.8}$$

$$\beta = 1.5 + \left\{ 0.85 + 0.135 \left[\ln\left(\frac{\ell_p}{\lambda_D} \right) \right]^3 \right\} \left(\frac{T_i}{T_e} \right), \tag{3.9}$$

$$\chi = \frac{1}{2} \ln\left(\frac{m_e}{m_i} \right) + \alpha \ln(\beta - \chi), \tag{3.10}$$

and

$$\psi_1 = -\ln\left[\left(1 + \frac{\psi_1}{\beta - \chi} \right)^{\alpha} + \left(1 + \frac{\psi_1 - \psi}{\beta - \chi} \right)^{\alpha} \right] + \ln[1 + \exp(\psi)]. \tag{3.11}$$

If we assume that the ion temperature is small compared to the electron temperature ($T_i \ll T_e$), then this series of equations is somewhat simplified. Eqs. 3.5 - 3.11 can be numerically iterated to yield the electron temperature and plasma density. Most of our measurements presented in the following chapters required this thick-sheath analysis, especially in certain operating conditions and in the plasma-sparse plume far-field.

To make the measurements required for this analysis the probe was constructed of 1 mm diameter tungsten rods slip-fit into a standard 3.2 mm diameter double bore alumina tube. The probes were physically mounted to the probe positioning system. A floating Keithley 2400 Sourcemeter interfaced with the main LabVIEW DAQ VI is used to bias the probes from $-100 \leq V \leq 100$ V and sink the measured current. To determine the error in the plasma density and electron temperature the I-V trace is bootstrapped at least $1,000$ times. Bootstrapping is the practice of reconstructing the I-V trace using randomly selected bias points and a randomly selected corresponding current bounded by the original errorbars at that point. To clarify this process, take an example trace of the double probe like the one in Figure 3.13. Referring to Figure 3.13, during the boostrapping process the collected current at each bias potential is randomly assigned, with the value residing between the

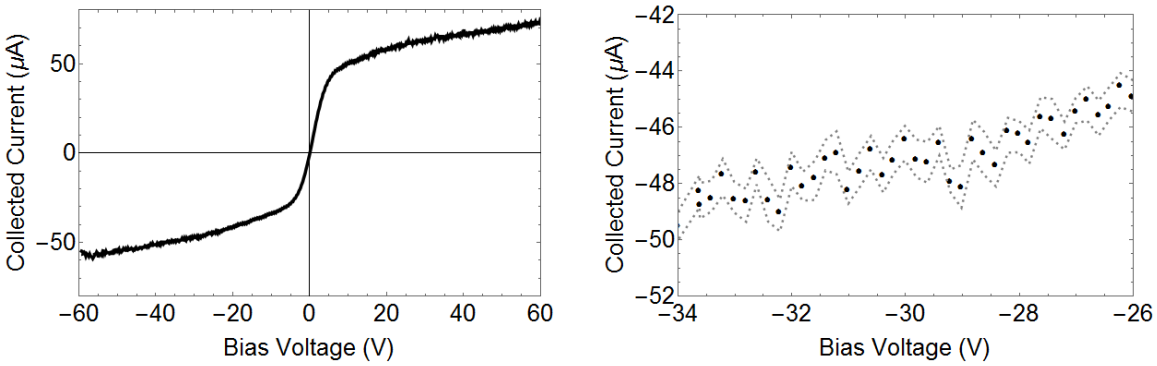

Figure 3.13: a) A characteristic I-V trace measured with the double probe. This specific trace was measured at the centerline, exit plane of the testbed article operating in the solenoidal antenna with an external RF matching network configuration with $\sim$ 170 W input power, 3 mg/s of xenon, and a throat strength of 300 G. b)A subset of the measured I-V trace (black dots) and the associated error at each point (gray dashed lines).

upper and lower error bounds depicted in the figure. These errors were characterized as the combination of the 2σ error through repeated measurements of the collected current at the trace voltage endpoints and the Sourcemeter error listed in the vendor documentation. The reconstructed trace is then fitted to extract plasma properties and this process is repeated. Assuming that the original errors are Gaussian-like the electron temperature and plasma density can be described by the mean and standard deviation of the bootstrapped results, with our chosen errorbars corresponding to 2σ. For clarity, the measurement locations with the double Langmuir probe for the testbed article configurations are outlined in Figure 3.14.

3.3.4 Emissive Probe

A DP cannot measure the plasma potential directly, so we use a hairpin emissive probe to supplement the DP measurements. A general electrical schematic for this probe can be found in Figure 3.15. This particular schematic is able to support both the inflection point and the floating point with large emission measurement methods [195, 196]. For simplicity and speed of measurement, we employed the floating point

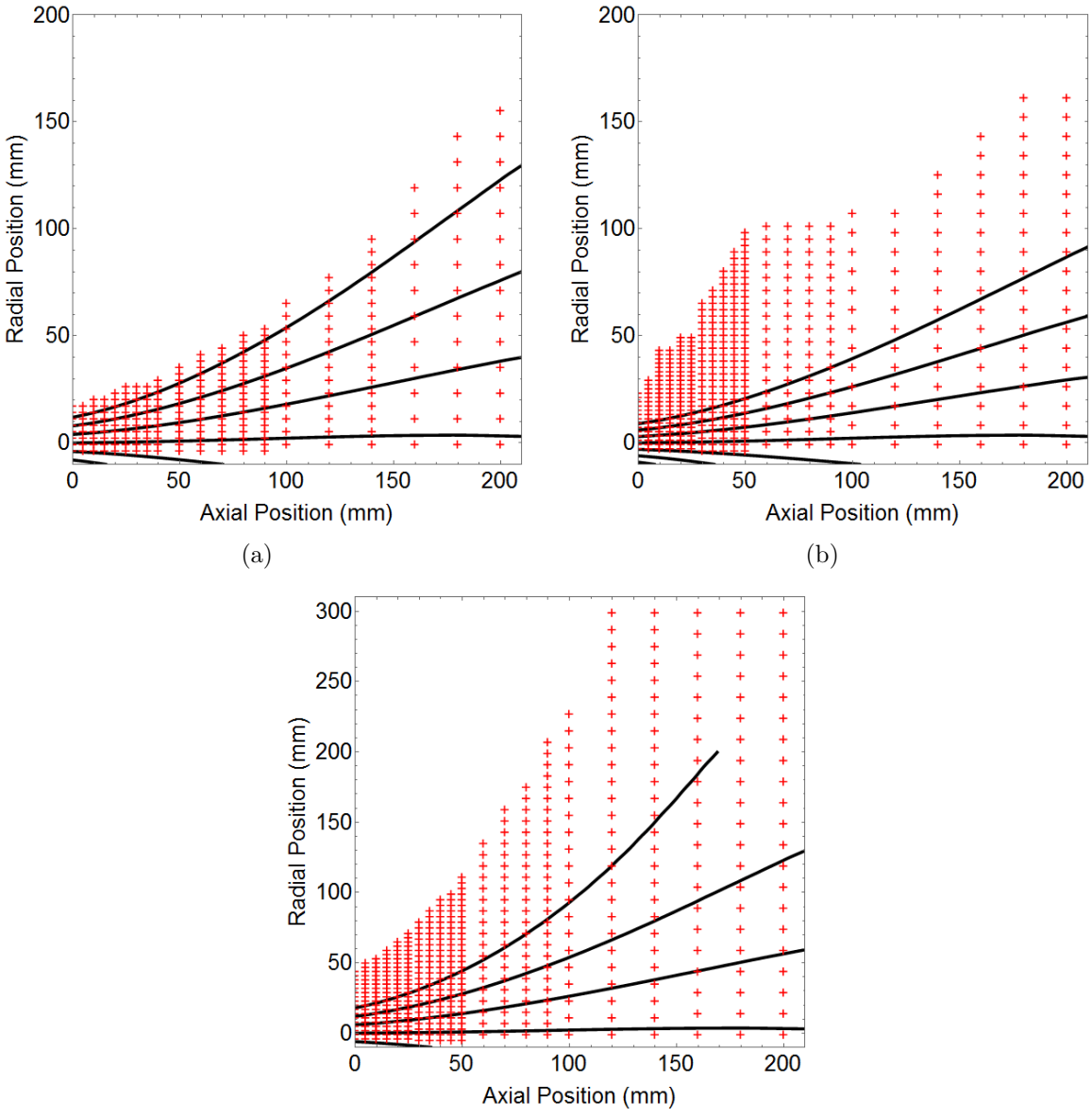

Figure 3.14: The double Langmuir probe measurement locations (center of the crosses) throughout the plume of the a) 2.5 cm ID solenoidal antenna, b) 1.9 cm ID solenoidal antenna, and c) planar antenna configurations overlain with the diverging magnetic nozzle lines (curves).

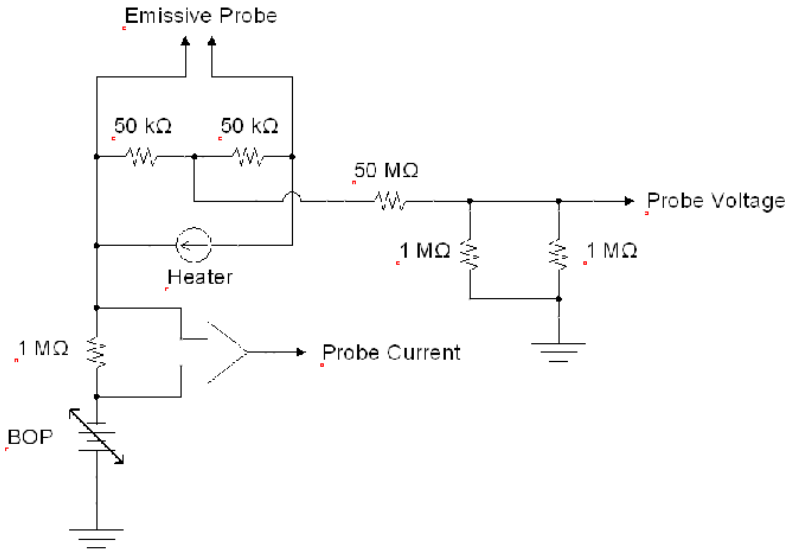

Figure 3.15: The general electrical circuit for a hairpin emissive probe.

with large emission method during our experimental campaign and accepted the higher error associated with this method [195, 196]. As such, the bipolar operational amplifier (BOP) in Figure 3.15 is removed.

It is important to note that an emissive probe does not directly measure the plasma potential; rather, it measures the sheath floating potential, which is typically offset from the plasma potential by a factor of T_e. Here we briefly highlight the theory outlined by Sheehan et. al. [196] that is used in our analysis. For a more complete discussion refer to Ref. [196]. Like the DP analysis, the first step in the emissive probe analysis is determining whether the probe is operating in the thin-sheath ($\ell_p \gg \lambda_D$) or the thick-sheath ($\ell_p \ll \lambda_D$) regime. There is no simple analytical models for a floating emissive probe, however in the thin-sheath limit the high emission floating potential can be approximated as

$$V_f^{em} = \phi - 1.5T_e + \Delta\phi_{vc}, \tag{3.12}$$

where $\Delta\phi_{vc}$ is the potential difference between the floating potential and the virtual cathode minimum. This last term captures space-charge effects that may be present, but for plasmas where T_e is much greater than the emissive probe wire temperature this term may be negligible [195, 196]. There is one major inconvenience with Eq. 3.12: the electron temperature must be known. Typically, the electron temperature is measured with a different diagnostic (like our DP here), but it is also possible to estimate this value using the emissive probe itself. This can be a quick check for the DP results. Noting that a floating potential adjusts such that no net current is drawn, and assuming the probe can be modeled as cylindrical, the electron current incident on the probe is

$$I_e(V) = \frac{en_eA_p}{4}\sqrt{\frac{8T_e}{\pi m_e}}\exp\left[\frac{e(V-\phi)}{T_e}\right]. \tag{3.13}$$

Noting that the ions must be accelerated to the Bohm speed for a probe operating in the thin-sheath limit and equating the ion and electron currents yield the cold floating potential:

$$V_f^c = \phi + T_e \ln\left(0.61\sqrt{\frac{2\pi m_e}{m_i}}\right). \tag{3.14}$$

For a xenon plasma the cold floating potential in the thin-sheath regime can be approximated as

$$V_f^c = \phi - 5.77T_e. \tag{3.15}$$

The high emission floating potential (Eq. 3.12) and the cold floating potential (Eqs. 3.15) can be combined to eliminate the plasma potential and yield an estimate for the electron temperature as a function of the floating potentials - the measured values from the emissive probe. For the thin-sheath limit, the estimated electron temperature is

$$T_e^{est} = \frac{V_f^{em} - V_f^c}{4.27}. \tag{3.16}$$

However, if the probe is operating in the thick-sheath regime the maximum collected ion current becomes

$$I_i(V) = \frac{2en_iA_p}{\sqrt{\pi}}\sqrt{\frac{-e(V-\phi)}{2\pi m_i}}. \tag{3.17}$$

By equating Eqs. 3.13 and 3.17 the relationship between the cold floating potential, plasma potential, and electron temperature in the thick-sheath limit can be determined:

$$\frac{4m_e}{\pi m_i} = \frac{T_e}{e(\phi - V_f^c)} \exp\left[\frac{2e(V_f^c - \phi)}{T_e}\right]. \tag{3.18}$$

This equation can be implicitly solved for the cold floating potential as a function of electron temperature and plasma potential. For xenon this results in

$$V_f^c = \phi - 5.24T_e. \tag{3.19}$$

For the thick-sheath case the high emission floating potential can be written as

$$V_f^{em} = \phi - \delta T_e, \tag{3.20}$$

where $0 < \delta < 1.5$. These bounds stem from the fact that for an electropositive plasma (like xenon) the floating potential is lower than the plasma potential ($\delta > 0$) and must be less than the thin-sheath cold floating potential ($\delta < 1.5$ - from Eq. 3.14). The value for δ in the thick-sheath case is difficult to accurately predict; this results in an expression for estimated electron temperature that is not well defined

$$T_e^{est} = \frac{V_f^{em} - V_f^c}{5.24 - \delta}, \tag{3.21}$$

but can be useful to quickly check the order of magnitude of the DP electron temperature values. Recall that we assumed a xenon plasma for both the thin- and thick-sheath estimated electron temperature equations (Eqs. 3.16 and 3.21, respectively).

Armed with this analysis we built, our hairpin emissive probe. The probe is constructed of 250 μm diameter thoriated tungsten wire that is friction fit into a 1.6 mm diameter double bore alumina tube that is packed with filaments of tungsten wire [195, 196]. The additional tungsten filaments ensure that that the hairpin loop is the only portion of the probe that reaches emission temperatures. We heated the hairpin filament to electron emission using a a Sorensen $60-10$ DC laboratory power supply and measured the floating potential on each side of the filament using a pair of AD-210 isolation amplifiers. To account for the finite resistance of the hairpin filament, and resulting potential drop due to the heating current, the average of the two floating potential measurements is taken as the nominal value. This averaged value is corrected by an appropriate factor of T_e [195], depending on the thin- or thick-sheath regime that the probe encountered and using the electron temperature results of the DP, to determine the plasma potential. The floating potential is sampled at 10 kHz and at least 5000 samples are averaged at each measurement location. The error in the plasma potential is taken as the convolution of the propagated error in the electron temperature and 2σ of the sampled floating potential measurements. For reference, the emissive probe measurement locations for the testbed configurations are provided in Figure 3.16.

3.3.5 Guarded Faraday Probe

To complement the density, electron temperature, and plasma potential measurements of the DP and EP we also employ a planar guarded Faraday probe to infer ion velocity and plume divergence. The Faraday probe schematic - illustrated in Fig-

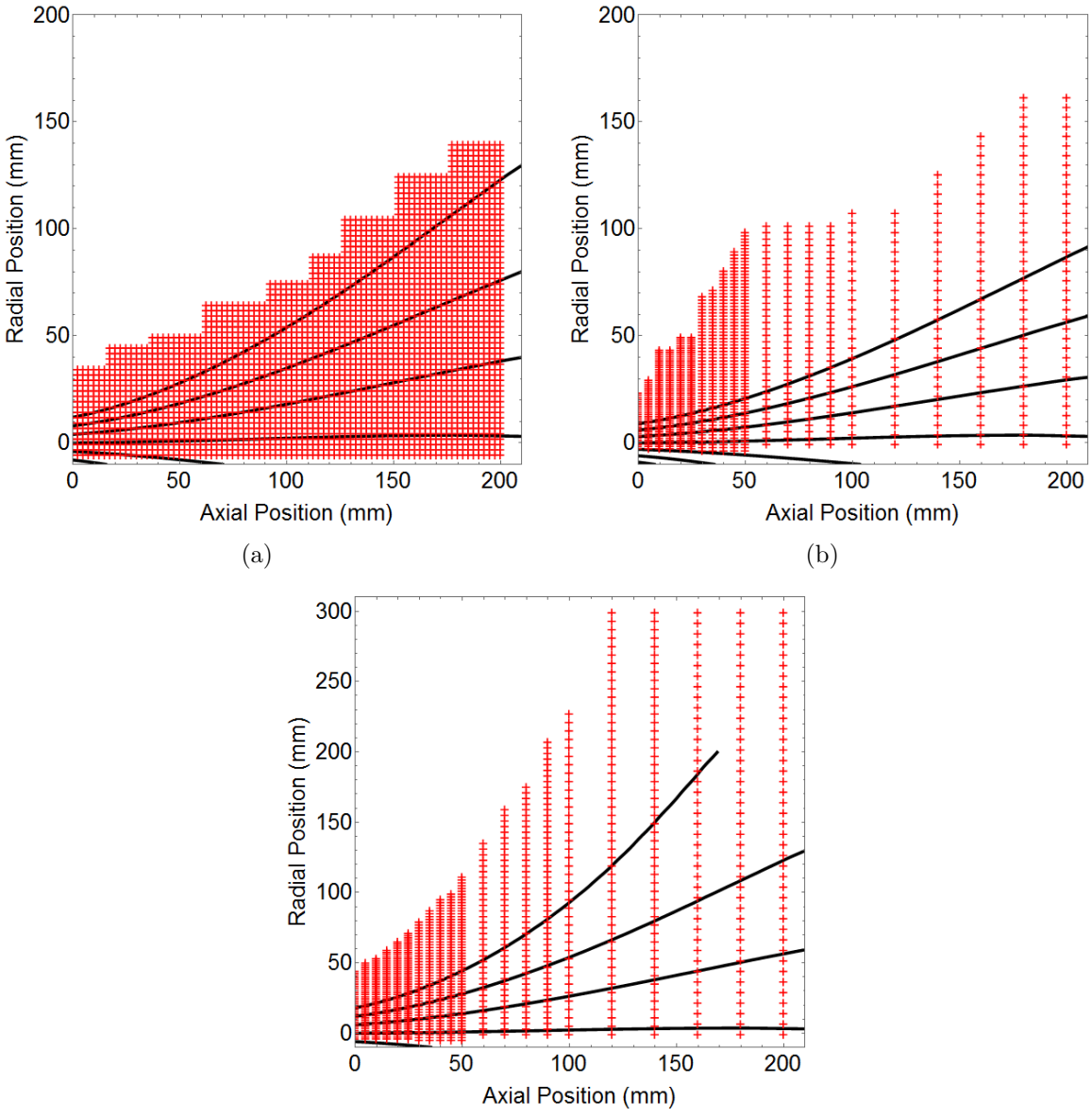

Figure 3.16: The emissive probe measurement locations (center of the crosses) throughout the plume of the a) 2.5 cm ID solenoidal antenna, b) 1.9 cm ID solenoidal antenna, and c) planar antenna configurations overlain with the diverging magnetic nozzle lines (curves).

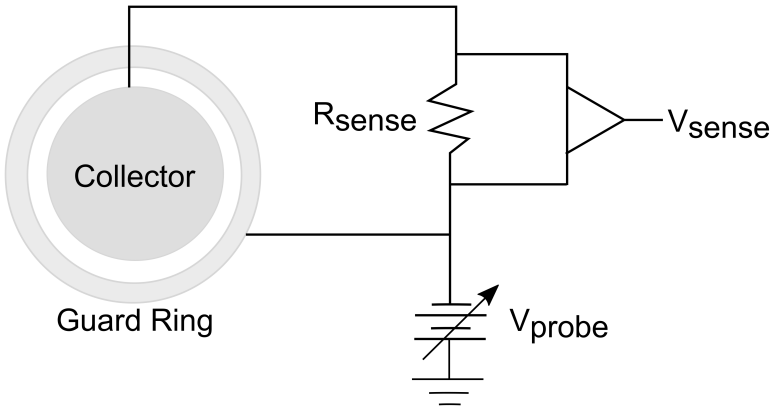

Figure 3.17: The axial evolution of the current density measured by the Faraday probe for the planar antenna source configuration.

ure 3.17 - is used to bias the probe into ion saturation and measure the collected current across a sense resistor. A Faraday probe that is biased into ion saturation ($V_{probe} \ll V_f$), assuming that the ion population is singly charge, collects ion current:

$$I_i = q n_i v_i A_p, \tag{3.22}$$

where v_i is the incident ion velocity. The inclusion of a guard ring flattens the probe sheath and serves to screen ions with shallow incidence angles from the collector [197], reducing erroneous current collection and reducing uncertainty in the effective probe collection area. Assuming that the plasma is quasineutral the collected current measurement, probe geometry, and plasma density from the DP can be combined to determine the incident ion speed. Directional information for the ion velocity can be inferred with knowledge of the probe orientation at each measurement location.

A spatially-resolved map of the ion velocity can be created by repeatedly taking measurements throughout the plume, possibly lending insight into acceleration mech-

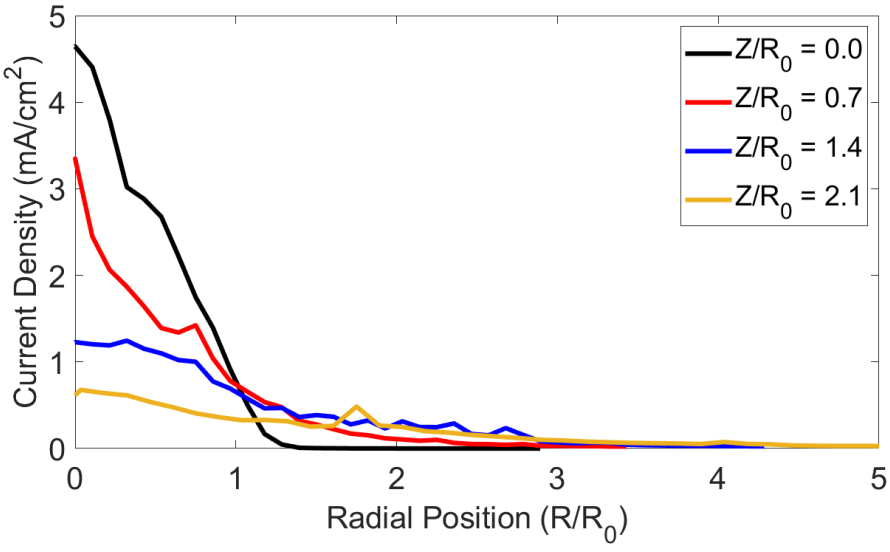

Figure 3.18: The axial evolution of the current density measured by the Faraday probe for the planar antenna source configuration.

anisms or plume divergence. The divergence angle of the plume can be determined from multiple Faraday probe measurement sweeps, with each sweep being taken at a fixed distance from the thruster exit plane. In our experiments, most of the Faraday probe measurements were taken in the plume near-field, so we follow the practice of using a cylindrical coordinate system for the thruster-probe system [197], with Faraday probe sweeps made at fixed axial distances downstream. An example of these radial sweeps at several axial distances for the planar antenna configuration can be found in Figure 3.18.

Note that the sweeps in Figure 3.18 have been normalized by the probe collection area to yield the current density. This form is convenient for determining the divergence angle of the plume. This analysis starts by determining the total plume current. For a magnetic nozzle, assuming axisymmetry, this can be determined by

$$I_{plume} = 2\pi \int_0^\infty j(r) r dr, \tag{3.23}$$

where $j(r)$ is the current density as a function of the radial position and r is the radial

coordinate. We use the Faraday probe sweep at the thruster exit plane to determine the plume current. We then choose to track the axial evolution of the area required to encompass 95% of the calculated plume current. This process yields a $(Z, R_{95\%})$ pair for each Faraday probe sweep. We can then use linear regression to determine the slope of the line through all Faraday probe $(Z, R_{95\%})$ pairs $(S_{95\%})$ and estimate the divergence angle using trigonometry:

$$\theta_{div} = \arctan\left(\frac{1}{S_{95\%}}\right). \tag{3.24}$$

In light of this analysis, we built our planar guarded Faraday probe following the design methodologies recommended by Brown et. al. [197]. Due to the small size of the testbed device the probe is constructed of a 1.5 mm diameter tungsten rod slip fit into a single bore alumina tube with a 2.3 mm OD. Tungsten foil - 80 μm in thickness - is wrapped around the alumina to create the guard ring. A pair of Keithley 2400 Sourcemeters apply a -50 V bias to both the guard ring and the collector, ensuring that the probe is collecting ion saturation current, and measure the collected current. The current density is calculated by dividing the collected ion current by the probe collection area. Due to motion stage constraints and the recommendation that Faraday probe measurements within 4 thruster diameters be treated as near-field measurements [197] only axial data is presented. The locations for the axial Faraday probe measurements for the source configurations are presented in Figure 3.19.

3.3.6 Time Averaged Laser Induced Fluorescence

To supplement the electrostatic probes we use a 2D time averaged Laser Induced Fluorescence (LIF) scheme to measure the axial and radial ion velocity distribution functions (IVDFs) noninvasively. Noninvasive diagnostics are advantageous for our study, especially in the near-field plume, because they do not require a physical

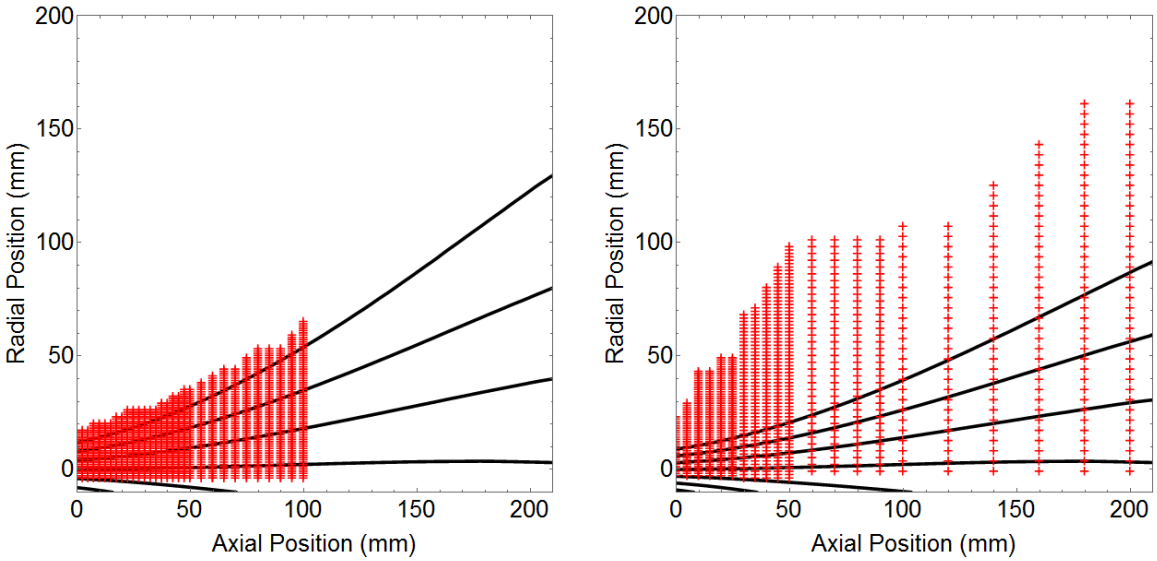

(a) (b)

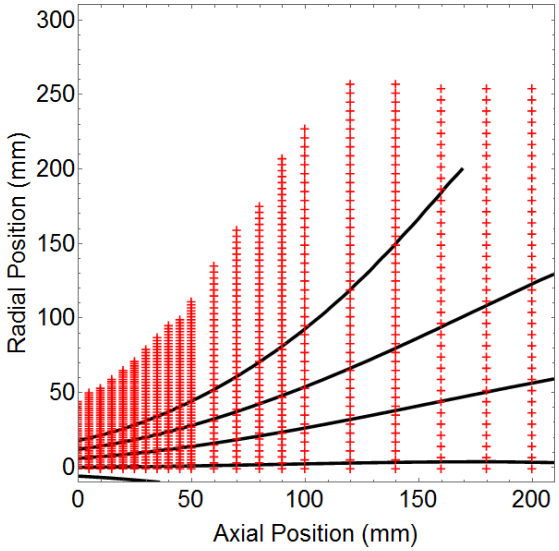

(c)

Figure 3.19: The axial Faraday probe measurement locations (center of the crosses) throughout the plume of the a) 2.5 cm ID solenoidal antenna, b) 1.9 cm ID solenoidal antenna, and c) planar antenna configurations overlain with the diverging magnetic nozzle lines (curves).

probe to be inserted into the plasma, thereby avoiding perturbations inherent with traditional electrostatic probes [198].

Our LIF setup measures the ion velocity by exciting ions in the $5d^2F_{7/2}$ state to the excited $6p^2D^0_{5/2}$ state. This excited state then relaxes to the $6s^2P_{3/2}$ state, releasing a photon. By counting the number of photons released over an integration period the ion intensity at a given wavelength is determined. By detuning the laser and accounting for Doppler shift the ion velocity distribution is measured. At a fundamental level the LIF profile is a convolution of the laser frequency profile, the Doppler lineshape, and the line broadening profile:

$$\Phi(\nu) = \alpha(\nu) \circledast \Phi_D(\nu) \circledast \Phi_L(\nu), \tag{3.25}$$

where $\alpha(\nu)$ is the Doppler-free lineshape, $\Phi_D(\nu)$ is the Doppler lineshape, and $\Phi_L(\nu)$ is the laser frequency profile. LIF leverages the fact that for moving, nonrelativistic ions the change in frequency observed by the ions is

$$\Delta\nu = -\nu_L \frac{v_k}{c}, \tag{3.26}$$

where ν_L is the laser frequency, v_k is the projection of the ion velocity along the laser path, and c is the speed of light. Since the metastable transition wavelength is fixed in the laboratory frame, the Doppler-shifted frequency indicates the ion velocity along the laser path. Due to the fixed wavelength, the corresponding laser frequency to excite the transition is equal to the zero-velocity transition frequency for fluorescing ions in the ion frame is

$$\nu_t = \nu_L + \Delta\nu = \nu_L \left(1 - \frac{v_k}{c}\right). \tag{3.27}$$

The ion velocity along the laser path for at a given laser frequency can then be written as

$$v_k = c\left(1 - \frac{\nu_t}{\nu_L}\right). \tag{3.28}$$

Physically, by repeating this process across a range of laser frequencies, the Doppler lineshape is mapped to the ion velocity distribution along the laser path. Assuming that the Doppler lineshape is integral normalized, the velocity distribution can be formally written as

$$f(v_k) = \frac{\nu_t}{c\left(1 - v_k/c\right)^2}\Phi_D\left(\frac{\nu_t}{1 - v_k/c}\right). \tag{3.29}$$

Note that this result is a 1D ion velocity distribution. We estimate the mean ion velocity in a given direction by using the moment of a sums-of-Gaussian fit to the measured IVDFs. An example of the sums-of-Gaussian fit can be found in Figure 3.20. Orthogonal laser paths can yield 1D distributions for each laser path, but information concerning how the velocity in one direction relates to the velocity in other directions is lost. For our analysis we accept this information loss and assume that there is a single ion population at each point in space; our mean velocity analysis then yields values in each direction (axial and radial). These mean velocities can be combined to approximate the velocity vector. To enhance the measurement signal-to-noise ratio we integrate the measurement over long time periods (1 ms - 1 s) at each discrete laser frequency, therefore we also assume that the time-averaged velocity distribution is representative of a single ion population.

Due to the presence of the magnetic nozzle, we had to assess the potential impact of Zeeman splitting on our results. Following the approaches of Jorns et al. [199] and Huang et al. [200], and assuming that the ion velocity distribution is Maxwellian, we estimate that Zeeman splitting adds $\leq 5\%$ to the uncertainty in the ion velocity measurements at the exit plane. Due to the rapid decay in the magnetic field strength with increasing distance from the exit plane, the uncertainty due to Zeeman splitting

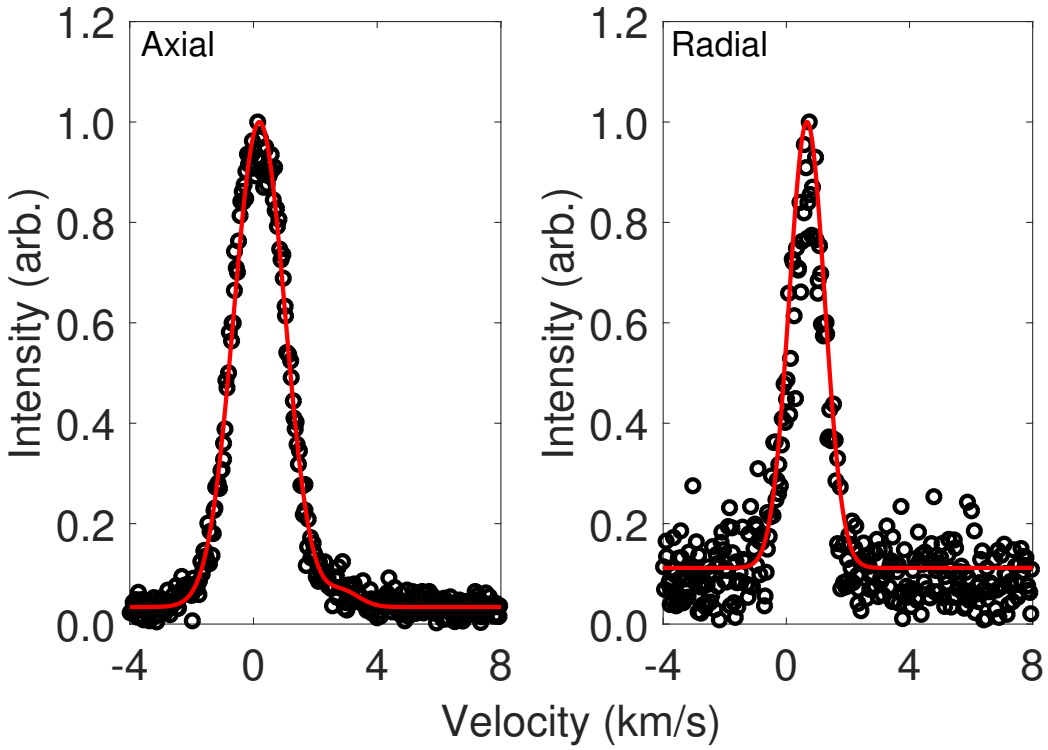

Figure 3.20: An example axial and radial IVDF at $(Z, R) = (0, R_0/4)$ for the large solenoidal antenna configuration operating at ~ 170 W net deposited power, 3 mg/s xenon flow rate, and 400 G peak magnetic field.

decreases downstream. This low uncertainty contribution allows us to neglect this effect in our analysis of the results.

To make these IVDF measurements we use the 2D LIF system notionally outlined in Figure 3.21. In the injection leg we use a New Focus TLB-6716-P Velocity External Cavity Diode Laser with a nominal wavelength of 834.7 nm (in air) to excite the xenon ion transition. A sampler diverts $\leq 1\%$ of the laser power into a wavemeter, etalon, powermeter, and an opto-galvanic cell through a chopper. The wavemeter measures the laser wavelength at each point along the IVDF. The laser mode quality is monitored by the etalon while the laser power is measured by the powermeter. For the experiments herein the laser power remained constant throughout the sweeps so no IVDF corrections were required. The laser wavelength corresponding to zero ion velocity is measured with the opto-galvanic cell. To reduce noise the leg of the laser entering the opto-galvanic cell is chopped and the output signal is sampled using a Lock-In-Amplifier (LIA). Similarly, the two injection legs - one for the radial and the other for the axial measurements - are chopped at distinct frequencies and collimated into optical fibers. The fibers are then passed into the chamber via potted FC/PC feedthroughs.

Inside the chamber the fibers are connected to the injection optics. The internal optics are aligned using an optical pin mounted to the source. We verify the chamber-source-optics alignment by moving the source mounted to the translation stages. The collection optics are also aligned to the optical pin and feeds the measured signal into the collection fibers. These fibers are passed to the external LIF setup through an SMA feedthrough.

In the collection leg of the system the collected light is passed through a spectrometer, a PMT, and a trans-impedance amplifier (TIA). The spectrometer band-pass filters the collected broadband light, retaining the relevant wavelengths. The signal is then amplified by the PMT and the resulting current signal is converted into a voltage

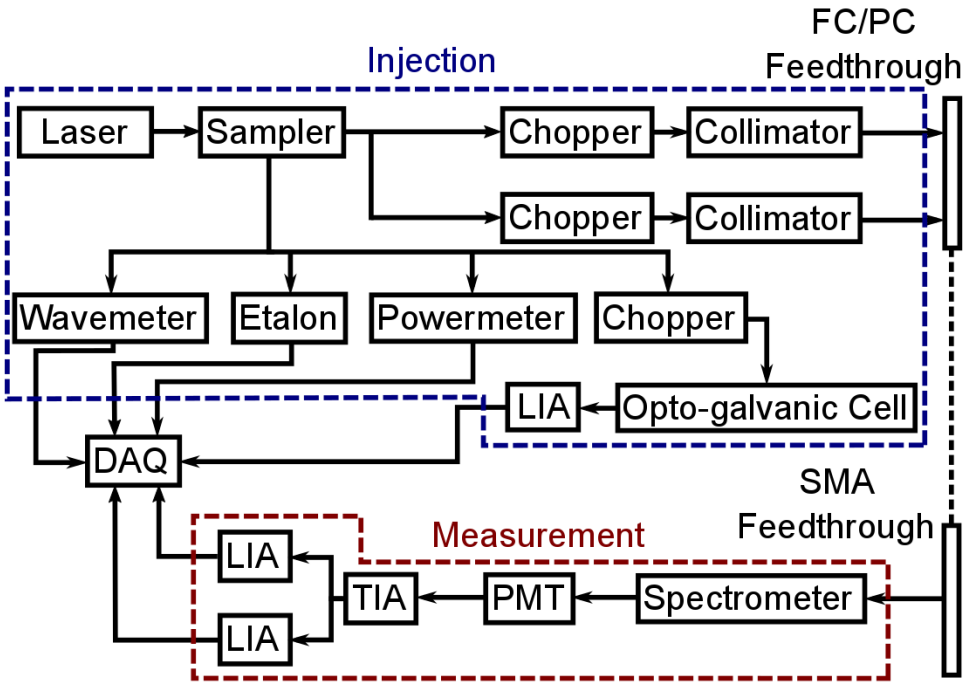

Figure 3.21: A block diagram of the time averaged LIF experimental setup.

signal by the TIA. This voltage signal is passed into a pair of LIAs that decompose the signal into the axial and radial measurements. This process is repeated for each laser scanning wavelength to yield an IVDF in both directions.

3.3.7 Motion Stage Positioning System

To facilitate 2D plume mapping we use a motion stage positioning system comprised of two Velmex Unislide translation stages with 84 cm (transverse) and 69 cm (longitudinal) ranges. The motion stages are controlled by a PhidgetStepper 1067 motion circuit interfaced with a LabVIEW VI that converts a user-specified measurement grid into motor steps. We use this positioning setup to interrogate the plume from source centerline to several centimeters beyond the vacuum interface magnetic field line and from the source exit plane to 20 cm downstream.

The first configuration described in Section 3.2 is designed to facilitate time-averaged LIF measurements by allowing the optics to reside at a fixed location. As

illustrated in Figure 3.22a, in this configuration the plasma source is mounted on the pair of translation stages and moved relative to the LIF optics and fixed-position electrostatic probes. In the other two configurations the internal RF matching network requires the testbed device to reside at a fixed location. We interrogate the plume with electrostatic probes mounted to the this motion stage positioning system. Figure 3.22b depicts this setup.

3.4 Summary

In this chapter, we have detailed the configurations of the versatile test article that we used throughout work and the vacuum facilities used during the experimental campaigns. The various test configurations were used to investigate different low-power magnetic nozzle operating regimes, and, as such, we observed different operating modes. These operating modes were discussed to provide clarity and context for our work presented in the remaining chapters of this thesis. We have also described the plasma diagnostics that were used and outlined the analyses associated with each. We next use these test article configurations and this suite of plasma diagnostics to measure the plasma properties required for the performance model described in Chapter II. The fusion of these experimental measurements and the performance framework allows us to examine the physical mechanisms present in low-power magnetic nozzle devices and quantify their impact on performance.

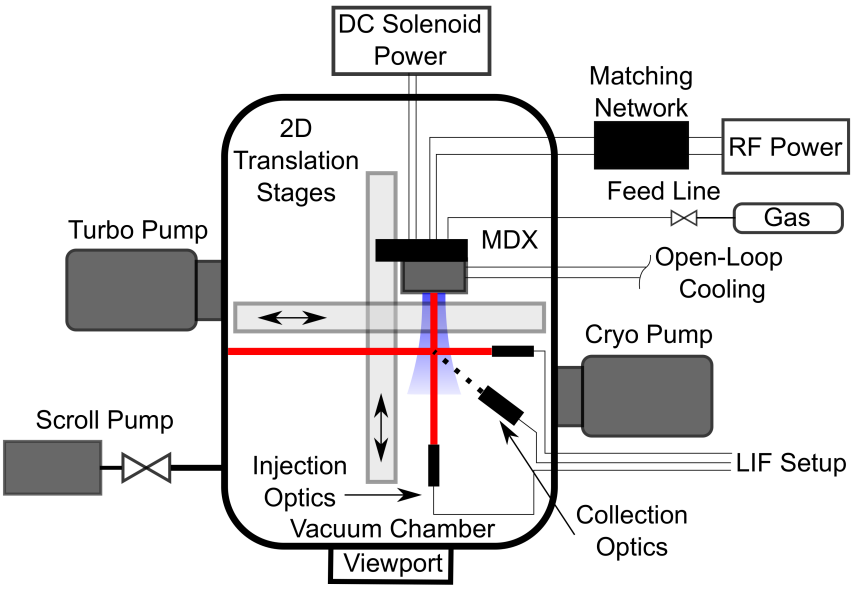

(a)

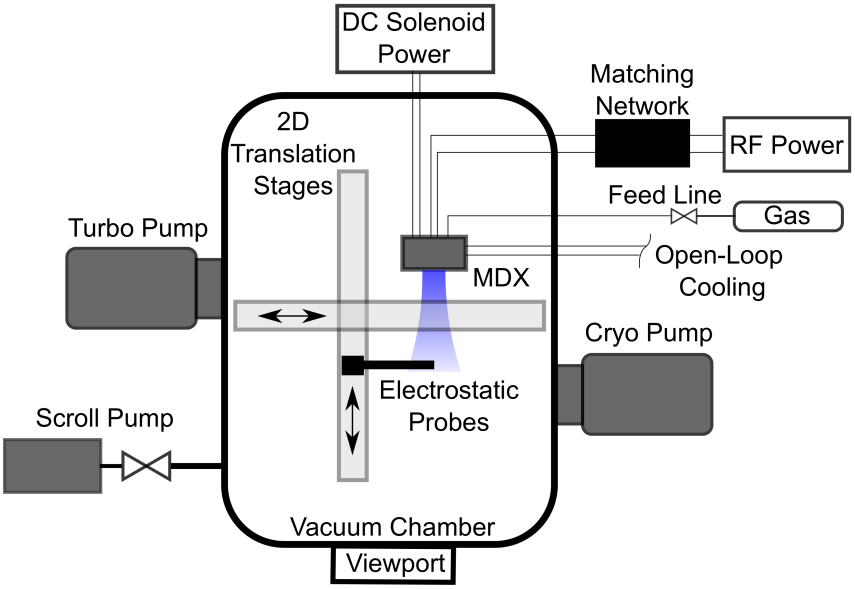

(b)

Figure 3.22: a) The experimental setup used to measure the spatial evolution of the ion velocity distribution throughout the expanding magnetic nozzle using LIF. b) The experimental setup used to map the 2D spatial plasma properties within the plume using electrostatic probes.

CHAPTER IV

Impact of Near-Field Neutral Density on Thrust Performance

4.1 Introduction

In this chapter we examine the performance of the low power magnetic nozzle test article operating in a low ionization fraction regime. To this end we combine the theoretical performance framework outlined in Chapter II with the plasma diagnostics in Chapter III. In the derivation of the theoretical performance architecture we assumed that the neutral species played a negligible role in the plume expansion and overall device performance. In this chapter, we examine the validity of this assumption. This question is of particular interest because, to date, existing magnetic nozzle predictive models neglect the role of the neutral species beyond the source region [84, 92, 94, 149, 152]. It is unclear if this species plays an important role in the plasma expansion or significantly impacts the device performance.

To explore this question, we configure the plasma source and set the operating conditions such that the ionization fraction is low. In Section 4.2 we present extensive spatially-resolved plume maps of the exhaust structures that were obtained using the suite of electrostatic probes and LIF outlined in Chapter III. Using these experimental results, we are able to apply the theoretical architecture derived in Chapter II to

determine the both the empirical and expected performance of the test article. We discover that the performance of the device is significantly lower than the predicted performance. We posit that an apparent downstream shift in the location where the ions become sonic is a primary contributor to the observed performance discrepancy. Indeed, we demonstrate that the nozzle performance theory agrees well with the empirical thruster performance when the model throat location is shifted to coincide with the actual ion sonic location. In Section 4.3, we explore possible underlying neutral-driven mechanisms that may contribute to the delayed onset of the sonic condition and proceed to correlate these mechanisms to the downstream shift in the sonic location. We present evidence that ion-neutral collisions and ionization may be mechanisms that influence the plasma expansion, while electron-neutral elastic collisions do not appear to play a significant role. We summarize our results and discuss the ramifications of these findings in Section 4.4.

4.2 Experimental Results

In this section we present the measurements of the plasma properties necessary to evaluate the measured and model predictions for nozzle performance. The source was configured in the 2.5 cm OD solenoidal antenna case detailed in Chapter III. Refer to Figure 3.2 for a notional diagram of this configuration. These data were taken with the nozzle operating at $\sim$ 170 W combined deposited power into the transmission line and plasma source and 3 mg/s xenon propellant flow rate. We took measurements for magnetic field strengths ranging from 100 - 600 G at 100 G intervals.

4.2.1 Plume Properties

4.2.1.1 Plasma Properties

In Figure 4.1 we show contours maps of the measured plasma density, plasma potential, and electron temperature in the nozzle plume. The electron temperature map in figure 4.1a shows cooling as the plasma expands downstream. This indicates that the plasma is not isothermal and is losing thermal energy. In turn, this cooling is correlated with the spatial distribution of the plasma potential, which figure 4.1b shows is highest at the nozzle inlet and decreases with distance from this plane. The electrostatic field in the plume that results from this potential structure is the mechanism for accelerating ions. The plasma density plot (Figure 4.1c) shows the evident expansion of the plasma in the axial and radial directions with the highest density concentrated on centerline at the throat. This is consistent with the plasma pressure, as represented by the electron pressure, decreasing as it expands. The convolution of the ion acceleration and the density profile is captured in the axial ion current density plot in Figure 4.1d. However, there is a notable feature in the plasma density and current density profiles: for slices at constant axial location beyond the $(Z/R_0) = 1$ plane, the plasma density exhibits a radially non-monotonic dependence. This is characterized by an effective "clustering" near the vacuum interface line. This type of structure has been observed before [88] and may be explained in part by a combination of spatially non-uniform heating within the plasma liner [165, 166] and the presence of a corresponding well in plasma potential along this boundary (Figure 4.1b). This potential well structure has been noted in a number of magnetically confined plasmas [83, 201, 202, 203] and can be interpreted as the consequence of charge separation that results from ions with sufficient transverse energy overshooting the attached electron fluid. The potential well forms to counter this finite transverse ion inertia and deflect the ion streamlines back toward the field-aligned electron stream-

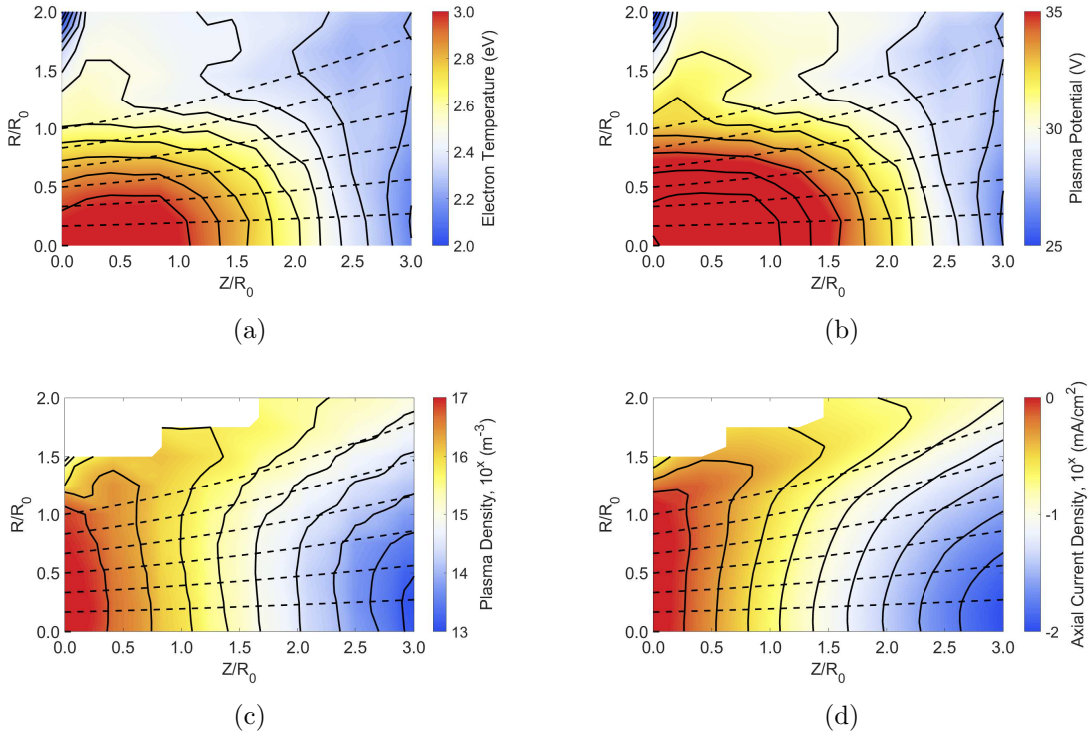

Figure 4.1: a) A spatial map of the electron temperature, b) plasma potential, c) plasma density and d) axial ion current density (contour and solid curves) with an overlay of the magnetic nozzle field lines (dashed curves) for the 400 G, $\sim$ 170 W net deposited power, and 3 mg/s xenon propellant flow rate operating condition. Note the potential well near the vacuum interface line and that the axial position is referenced to the throat location.

lines [83, 201].

4.2.1.2 Ion Acceleration

Taken together, the plasma measurements in Figure 4.1 show that the conditions are appropriate for electrostatic ion acceleration. We measured this acceleration directly in the near-field with the LIF system by characterizing the axial and radial IVDFs simultaneously (see Figure 4.2a). The mean velocity in each direction is calculated by taking the moment of these distributions after applying a sums-of-gaussians fit. The resulting vector map exhibits a subsonic ion speed at the source exit plane ($c_s \sim 1.5$ km/s for this 400 G condition) and large radial velocity components

throughout the plume. The error in these measurements is estimated as the 95% confidence interval after bootstrapping the IVDFs 10,000 times; the largest error is at $(Z/R_0,R/R_0) = (5/4, 3/2)$ mm with $\pm 12\%$ error in speed and $\pm 4^\circ$ in angle. The trajectories of the ions are consistent with our measurements of the plasma potential in Figure 4.1. Indeed, following these contours, it is evident that the ion trajectories appear to be driven by electrostatic acceleration resulting from the potential structure. This is consistent with our physical interpretation of the nozzle dynamics outlined in Chapter II. Moreover, we note that our results are consistent with previous nozzle studies in two signficant ways. First, as shown in Figure 4.2b, the ions are in fact accelerated, albeit not prodigiously, in the axial direction as they transit downstream. This is an indication that the ions are gaining directed kinetic energy as they transit the nozzle. Second, the ions appear to exhibit an "outward separation" in so much as their trajectories diverge more quickly than the nozzle streamlines. This type of ion motion has been seen both experimentally [83] and predicted numerically [149].

Due to low signal-to-noise ratio in the downstream region where the plasma becomes more sparse, we were only able to map the ion trajectories using LIF in the region shown in Figure 4.2. To supplement the near-field data and provide a more complete depiction of the ion dynamics, we also mapped the ion current density in the far-field (see Figure 4.1d). This spatial map, like all the electrostatic probe maps, extends from the near-field into the plume far-field. The overlapping of the ion current density map with the LIF measurements allows for the inference of the far-field ion velocity when coupled with the plasma density measurements, assuming that the plasma is singly ionized ($j = qn_e u$). This map reveals a new detail for the ion trajectories: as shown in Figure 4.2c, the centerline ion velocity plateaus within $(Z/R_0) \sim 5$, thus we are able to empirically designate this plane as the detachment location.

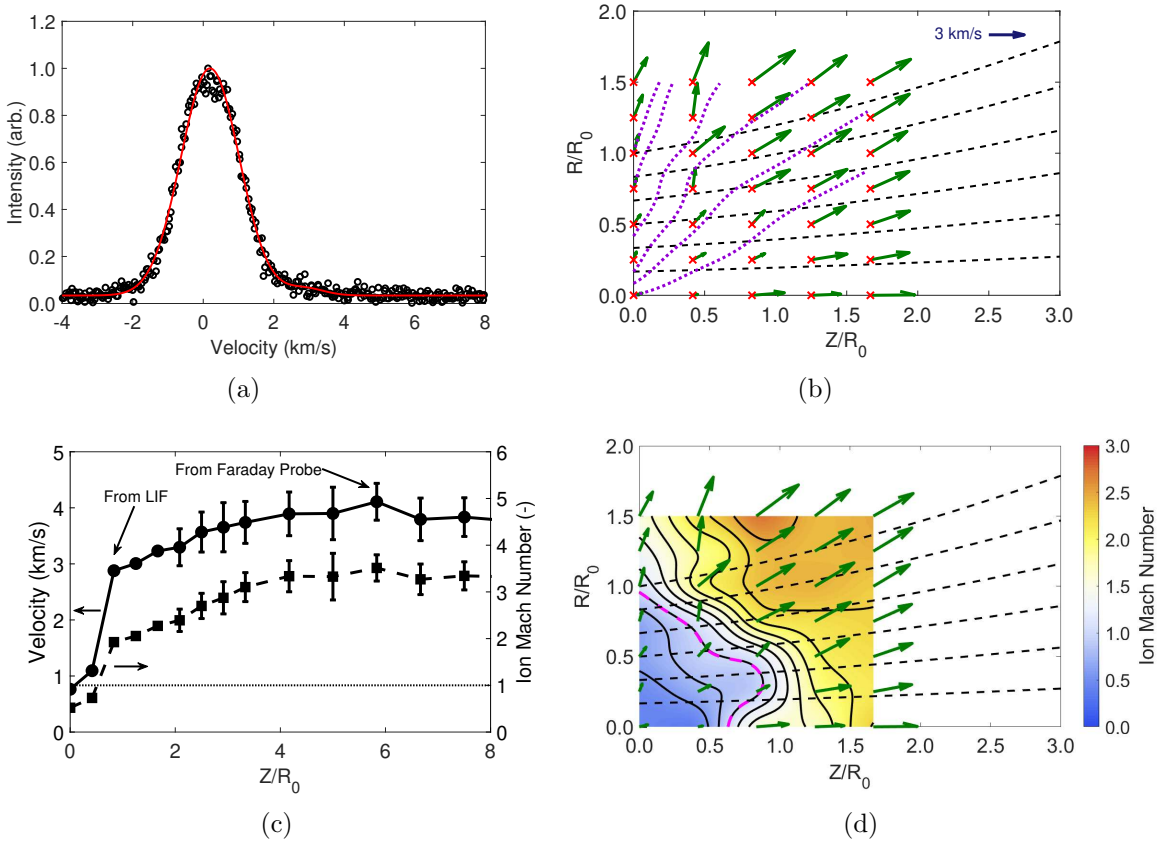

Figure 4.2: a) An example axial IVDF at $(Z/R_0, R/R_0) = (0, 1/4)$ with a sums-of-Gaussian fit (solid curves) to the raw data (circles). b) The resulting ion velocity vectors (arrows) and corresponding ion streamlines (dotted curves). c) The mean axial ion velocity on centerline. d) The inferred local ion Mach number (contour and solid curves) with an overlay of the magnetic nozzle field lines (dashed curves). All data is taken from the 400 G, $\sim$ 170 W net deposited power, and 3 mg/s xenon propellant flow rate operating condition. Note that the measurement locations are indicated by an 'x' and that the axial position is referenced to the throat location.

4.2.1.3 Mach Number

In Figure 4.2d we show a plot of the calculated ion Mach number. This result reveals a notable feature that is inconsistent with the physical assumptions we outlined for the model described in Chapter II: it is evident that at the inlet plane of the nozzle, which is characterized by the peak magnetic field magnitude, the ions have not become sonic. Instead, the sonic transition occurs further downstream at location $(Z/R_0) \sim 0.5$. This result is consistent with recent work that has been performed on a low power electron-cyclotron resonance thruster [113] and seems to be evidence that the idealized nozzle expansion may have some limitations in describing this low power regime of operation. We revisit this in the following section.

4.2.1.4 Polytropic Cooling

With the plasma measurements from the preceding sections, we have nearly all of the information required to evaluate both the experimental and analytical predictions for nozzle conversion efficiency. The major remaining key element is the polytropic cooling index. However, we can estimate this value by noting that $d\phi/dT_e = \gamma/(\gamma - 1)$ and using linear regression of the plasma potential versus electron temperature [164, 204]. The resulting best fit linear regression to the data along centerline is shown in Figure 4.3a for the six magnetic field settings that we investigated in this work. The error is estimated by using the lines fit to the extremes of the data and its associated error, resulting in the steepest and shallowest line slopes (see Figure 4.3b). For comparison, we also show the polytropic index for adiabatic and isothermal cooling. In all six cases, it is evident that $\gamma \sim 1.1$, which is within the range of measured values for electric propulsion devices operating on xenon [99, 114, 204, 205], and between the adiabatic ($\gamma = 5/3$) and isothermal ($\gamma = 1$) limits.

Summarizing the above results, we see that this low power nozzle does exhibit the type of behavior we expect for these devices. Electron thermal energy evidently is

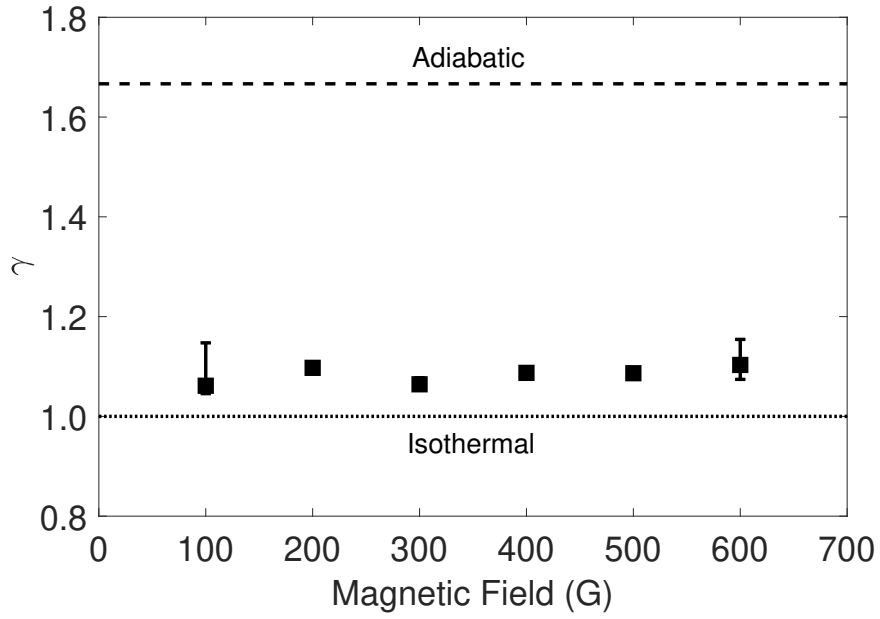

(a)

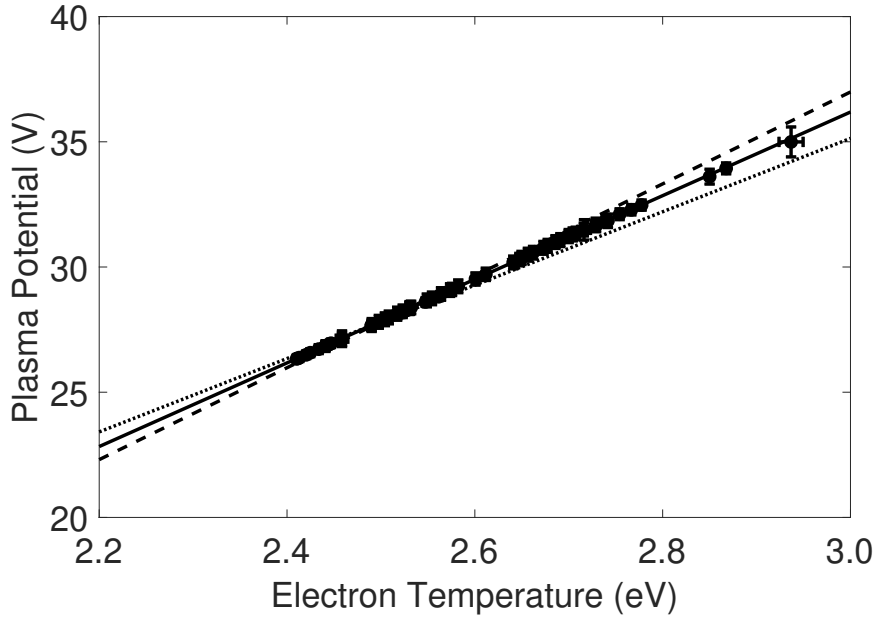

(b)

Figure 4.3: a) The value of the polytropic index inferred using linear regression of the plasma potential versus the electron temperature for the source operating conditions (squares). Note that value of the polytropic index is bounded by the adiabatic ($\gamma = 5/3$, dashed line) and isothermal ($\gamma = 1$, dotted line) limits. b) The measured centerline plasma potential versus the electron temperature (circles) for the 400 G operating condition and the best-fit regression line (solid line). The error in the polytropic index is calculated by using the lines fit to the data, and its associated error, such that the minimum and maximum slopes are obtained (dashed and dotted lines). Across all magnetic fields the device is operated at $\sim$ 170 W net deposited power and 3 mg/s xenon propellant flow rate.

converted to ion kinetic energy with the magnetic field acting as a mediating factor. This acceleration then occurs until a discrete downstream "exit plane." In the next section, we apply the formalism outlined in Chapter II to quantify the efficacy of this nozzle conversion and compare it to the analytical predictions.

4.2.2 Nozzle Performance

4.2.2.1 Efficiency

Leveraging the results from the previous section, we can employ the formulations from Chapter II - Eqs. (2.36) - (2.42) - to evaluate the nozzle efficiency. To this end, we estimated the location of the exit plane as the location where the ion velocity plateaus, as inferred from the Faraday probe, yielding A_d (as defined by the area swept by the vacuum interface lines). We estimated the axial component of the ion velocity at this exit plane from the Faraday probe data, yielding a value for u_d. We approximated the ion flow rate by using the measured density (double Langmuir probe), ion velocity (LIF), and source geometry at the throat ($\dot{m}_{ion} = m_i n_{e,0} u_0 A_0$). We determined the electron temperature at the throat using the double Langmuir probe measurements to yield $T_{e,0}$ and the polytropic index of ~ 1.1 from Figure 4.3. And finally, we estimated the ion energy cost using the analysis outlined in Lieberman and Lichtenberg [122] to yield ϵ_c. Combining these measurements and inferred values at the throat yielded a calculated power flowing into the nozzle and an estimate for thrust. With these values, we ultimately were able to use Eq. 2.42 to generate a plot of the nozzle efficiency, as shown in Figure 4.4a.

This result shows that the nozzle contribution to the overall efficiency is markedly low, $< 10\%$. In other words, this low power nozzle is only capable of converting 10% of the available energy at the inlet into directed exhaust. The major driver for this loss in efficiency is illustrated by looking at the different contributions to the nozzle power in Eq. 2.41, shown in Figure 4.5. It is evident from this figure that the

largest term is the ion cost, scaling with ϵ_c. This finding is consistent with previous works [85, 92, 94, 152] and underscores the dominant role of frozen flow losses associated with ion production. On the other hand, we note that the nozzle efficiency does monotonically improve with magnetic field strength. Physically, this trend is expected because our measured electron temperature at the throat increases with increasing magnetic field, and as previous work has shown, increased electron temperature can translate to improved efficiency [83, 94, 114]. We do note that the trend in electron temperature with magnetic field is not predicted by classical 0D global power balance models [122]; this power balance predicts that electron temperature decreases with increasing magnetic field strength due to the correspoding decrease in plasma diffusion to the radial walls. This discrepancy does not impact our analysis here as we focus on the downstream dynamics of the source. However, we note that there are a number of possible explanations for this result. For example, as Kinder and Kushner proposed, the increased electron temperature at higher magnetic field conditions may be explained by spatially non-uniform power deposition; a result that is numerically predicted for solenoidal antenna power coupling to a plasma in the presence of a magnetic field [165, 166].

For comparison to these measured results, we next evaluate the analytical predictions for the nozzle efficiency. To this end, we follow the conventional approach used in the formulation in Chapter II where we assign the "throat" to be the exit of the liner. We assume an expansion ratio consistent with the detachment point measured in Figure 4.2d ($A_d/A_0 = 6.7$) and that the ions are sonic at the throat. We also employ the measured electron temperature at the throat (Figure 4.1a) and the polytropic index (Figure 4.3). As can be seen from Eq. 2.42, in order to do a comparison between the analytical nozzle efficiency and measurements, we need to take into consideration the divergence efficiency of the system. We evaluated this correction by using Faraday probe measurements in the detachment plane and the

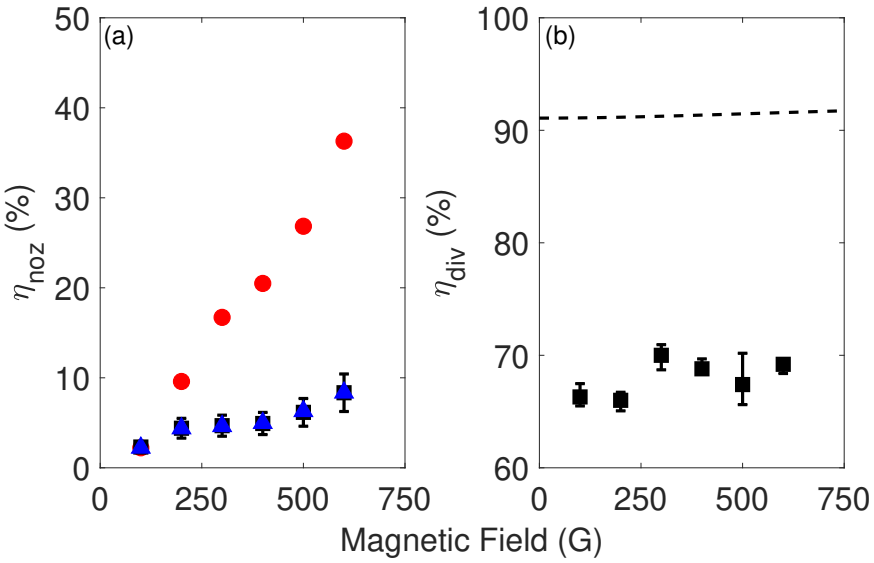

Figure 4.4: a) The inferred nozzle efficiency from measurements of the plasma source (squares) compared to the efficiency predicted by the ideal model (circles) and the model using the downstream throat properties (triangles). b) The divergence efficiency of the plasma source (squares) compared to the divergence efficiency of a fully attached, ideal nozzle that detaches as the same location. In all magnetic field conditions the source is operated with a net deposited power of $\sim$ 170 W and propellant flow rate of 3 mg/s xenon.

iterative path-finding method recommended by Brown et. al. [197] for use with these near-field Faraday probe measurements. As can be seen in Figure 4.4b, for all the magnetic field settings this yielded a divergence efficiency of $\eta_{div} \approx 68\%$. Armed with this result, we are able to plot the analytical predictions for nozzle efficiency in Figure 4.4a. From the comparison of the model and source results, it is immediately apparent that the analytical nozzle efficiency model overpredicts the measured value for all magnetic field settings by a factor of $\sim$ 5 at the highest magnetic field case (600 G). This is direct evidence that these types of idealized nozzle expansions are not representative of our actual system and underscores the point that, at low power, similar magnetic nozzles have a more nuanced behavior.

There could be a number of reasons why this discrepancy occurs, but the explanation we explore here stems from observations outlined in the previous section and informed by the work of Correyero et. al. [113]: the ions are not actually sonic at

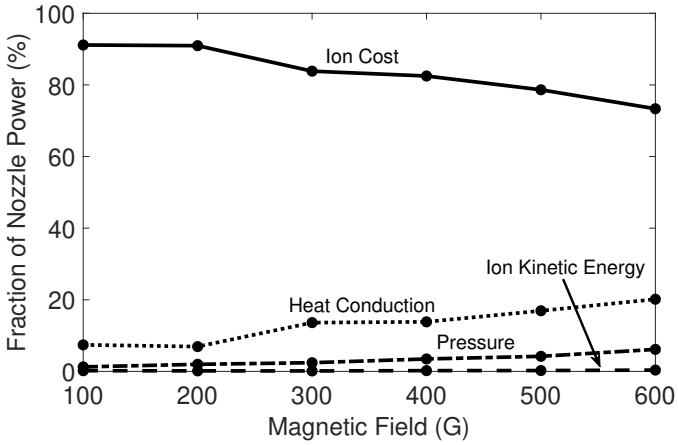

Figure 4.5: The fraction of all modes to the total power flowing into the nozzle. Note that at each magnetic field strength the net deposited power is ~ 170 W and xenon propellant flow rate is 3 mg/s.

the expected throat location. Critically, one of the key physical assumptions underpinning the physical model has been violated. With this in mind, we can explore the validity of the analytical model if we re-define the throat to not be coincident with the location of peak magnetic field, but, in keeping with the definition of classical nozzles, where the ions become sonic - location $Z/R_0 = 0.5$, as shown in Figure 4.2. By using this A_0 and the plasma parameters at this revised inlet plane, but preserving the same detachment location, we recover the experimentally inferred nozzle efficiency results shown in Figure 4.4a. What this shows is that by adjusting the throat to this new location the predicted and measured efficiency are directly coincident. The physical reason for this reduced performance is that we are effectively lowering the expansion ratio by moving the nozzle throat further downstream. This translates to a lower overall expansion through the nozzle and reduced recovery of thermal energy. This is strong correlational evidence then that the model is still applicable, provided we track more carefully the sonic condition, as found by Correyero et. al. [113].

Moreover, the increasing discrepancy between the model and source efficiency with increasing nozzle strength can be explained by tracking the location of the sonic condition as a function of magnetic field setting. This is shown in Figure

4.6a along with the location of the exit plane inferred from the procedure outlined above. Notably, the detachment plane does not shift, but with increasing magnetic field, the location of the throat — and therefore effective area of the throat — does move downstream. As shown in Figure 4.6b, this translates to a lower expansion ratio with increasing magnetic field strength compared to the expansion ratio that would be assumed if we ascribed the throat simply to the source exit plane. This explains why the model and actual efficiency results diverge more with increasing magnetic field strength.

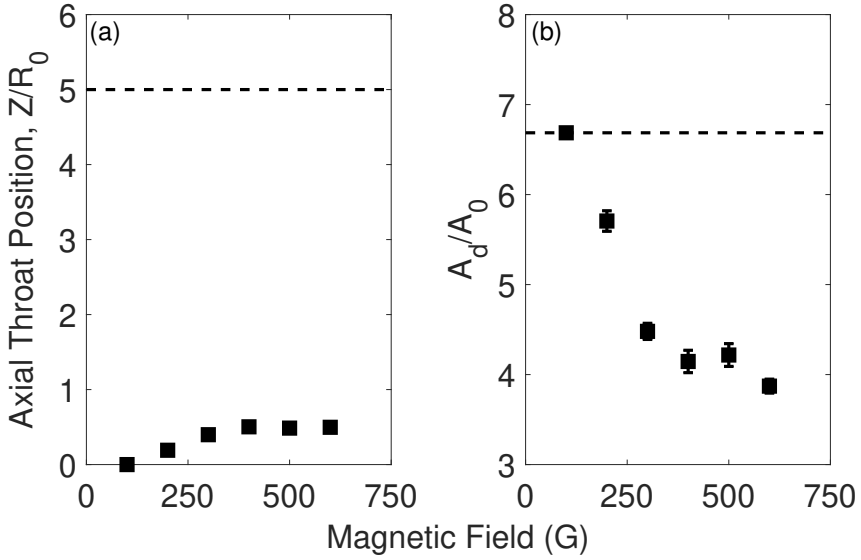

Figure 4.6: a) The downstream axial location of the effective nozzle throat (squares) and the detachment plane location (dashed line). b) The area expansion ratio of the nozzle after the throat is shifted downstream (squares) compared to the ideal nozzle expansion ration (dashed line). In all magnetic field conditions the source is operated with a net deposited power of ~ 170 W and propellant flow rate of 3 mg/s xenon.

4.2.2.2 Thrust and Specific Impulse

The physical reason why the expected throat and actual sonic line are not coincident at this low power is not immediately apparent. Before we discuss this in the following section, however, we briefly present here an analysis of other key performance parameters that can be inferred from these measurements: the thrust and specific

impulse. In the experimental plasma source, the plasma contribution to thrust is calculated using Eq.2.24 and is shown in Figure 4.7a. This thrust is compared to the plasma-generated thrust for the idealized model in Chapter II. For this latter calculation, we inferred thrust from the same equation but used the results from the model — Eqs. (2.42) - (2.44) with $\gamma = 1.1$, $A_d/A_0 = 6.7$, and measurement-inferred throat parameters — to determine the various detachment plane parameters $(u_d, T_{e,d}, n_{e,d})$. Using these parameters, the experimental source achieves thrust that is $\sim 50\%$ - 70% of the expected plasma thrust with a very low overall value. This is consistent with the efficiency measurements and can be explained similarly by the changing location of of the throat. To calculate the specific impulse, the plasma-generated thrust must be added to the cold gas thrust, which we calculate to be $\sim$ 850 μN, from $F_g = (\dot{m}_p - \dot{m}_{ion})v_g[1 + qT_g/(m_i v_g^2)]$ where $v_g = \sqrt{(5/3)qT_g/m_i}$ [94]. The neutral gas temperature is assumed to be room temperature ($T_g = 0.026$ eV). Due to the dominance of the cold gas thrust at these low power conditions, the specific impulse is limited to several 10s of seconds, as shown in Figure 4.7b. The two significant implications from this discussion of performance are 1) that the overall performance of this device is low with thrust in the micronewton range and specific impulse levels little better than cold gas, and 2) the analytical model overpredicts the performance. This type of low performance is consistent with most low power magnetic nozzles to date [37, 38, 40]. We also emphasize that, although we show efficiency values in Figure 4.4 on the order of 10%, these are only nozzle efficiencies. In practice, taking into consideration RF coupling and wall losses in the liner, the overall efficiency of this system is less than 1%, as is also consistent with most low power studies.

In either case, despite the low overall performance, one of the major findings from this work is that in low power operation, analytical predictions that rest on ascribing the throat location simply to be coincident with the peak magnetic field are insufficient. The correct performance can only be recovered if the location of the

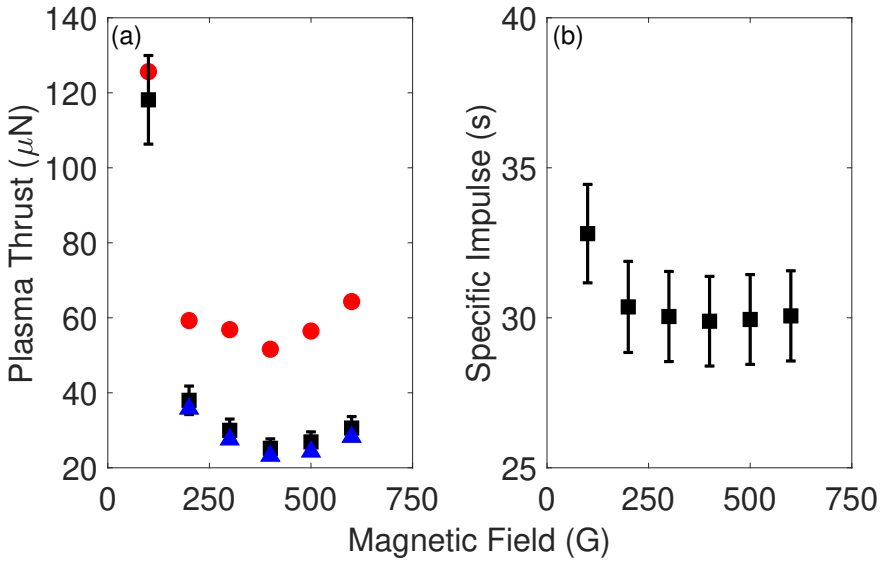

Figure 4.7: a) The inferred plasma contribution to thrust from measurements of the plasma source (squares) compared to the thrust predicted by the ideal model (circles) and the model using the downstream throat properties (triangles). b) The inferred specific impulse. In all magnetic field conditions the source is operated with a net deposited power of $\sim$ 170 W and xenon propellant flow rate of 3 mg/s.

throat is moved to the actual ion sonic line. We discuss in the next section a possible physical explanation for why this result occurs at low power.

4.3 Discussion

In this section, we examine potential physical mechanisms that may drive the shift in the location of the sonic point in the nozzle from the location of peak magnetic field intensity. Informed by our previous work [151], the hypotheses outlined in Correyero et. al. [113], and studies on these low temperature devices [84, 92, 94, 149, 152], the conjecture we explore here is that the throat may be driven downstream by collisional or ionization processes. In particular, this plasma has a low ionization fraction which results in a high neutral density within the nozzle exhaust, leading to effects not accounted for in an ideal analysis of magnetic nozzle performance. We look at three neutral-dependent mechanisms in particular: enhanced resistivity, charge exchange

collisions, and ionization within the plume.

4.3.1 Elastic Electron-Neutral Collisions

In order for the nozzle to accelerate the ions up to sonic speed, the electrons must be influenced by the magnetic field. In a low ionization fraction operating mode the plasma within the source tube is dominated by the neutral propellant gas. This is in contrast with the collisionless model detailed in Chapter II. In the case of low ionization fraction, electron-neutral collisions act to de-magnetize the electrons. At some point within the source tube in a sufficiently ionized device, the degree of ionization becomes high enough that neutral collisions no longer dominate and the plasma is guided by the converging-diverging magnetic field lines. However, we conjecture that due to the very low ionization fraction ($\sim 0.1-1\%$) the plasma remains dominated by collisions in the near-field plume. This precludes the accelerating action of the magnetic field until the neutral gas becomes sufficiently sparse that the electrons become magnetized.

To evaluate this mechanism empirically, we consider the electron-neutral Hall parameter:

$$\Omega = \frac{qB}{m_e \nu_{en}}, \tag{4.1}$$

where B is the local magnetic field strength, m_e is the electron mass, and ν_{en} is the electron-neutral collision frequency. Physically, if the Hall parameter is large ($\Omega \gg 1$) an electron undergoes many gyrorotations between collisions with a neutral. Conversely, if the Hall parameter is small, an electron undergoes either partial or few gyrorotations between collisions with a neutral. During each collision with a neutral an electron can move to an adjacent nozzle streamline; a large collision frequency results in enhanced cross-field electron transport.

Embedded within the electron-neutral collision frequency is a dependency on neutral density. In order to evaluate this parameter, it was necessary to map the neutral

density of the device. To this end, we show in Figure 4.8 the neutral density as inferred from pressure measurements made using a Stabil Ion Gauge with an integrated pitot tube. Note that the measurements are taken without power to the RF antenna, but the measured plasma density is typically ~ 3 orders of magnitude lower than the neutral density at the source exit plane. This low ion fraction suggests that the neutral profile shape does not significantly change with plasma ignition.

We show in Figure 4.9 a comparison of the electron-neutral collision frequency with the local magnetic nozzle field strength via an electron Hall parameter analysis for three magnetic field settings. We also show on these plots a dotted line coincident with the sonic condition for the ions, i.e. the so-called sonic transition. Significantly, we see that with increasing magnetic field strength this line shifts further downstream and coincides with Hall parameter values of $70 - 200$ - values that are indicative of a magnetized electron fluid. Fundamentally, these plots show opposite trends between Hall parameter and the throat location; as the nozzle field strength increases the Hall parameter increases within the near-field while the ion sonic transition moves further downstream. For clarity, this trend is illustrated in Figure 4.10, where the centerline Hall parameter is compared to the centerline ion Mach number. Physically, this trend shows that as the magnetic field increases the electrons in the near-field plume are becoming more magnetized closer to the source exit plane. The fact that this trend is counter to the downstream movement of the throat suggests that, while electron de-magnetization may play a role in the delayed ion acceleration, it is likely not a dominant mechanism.

While electron-neutral elastic collisions may not be a dominant mechanism to explain the downstream throat, it is interesting to note that the electrons appear to be magnetized upstream of the ion sonic line. This is consistent with the analogy of a de Laval nozzle where the gas is accelerated through a converging section to sonic velocity — the electrons should be effectively magnetized at the sonic point. In

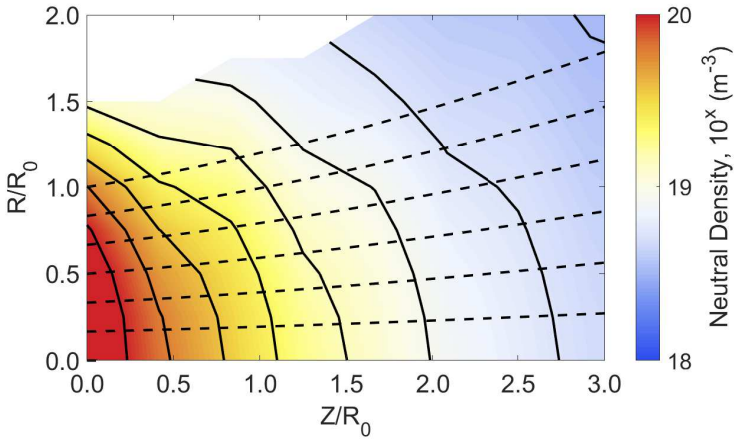

Figure 4.8: A spatial map of the neutral density (contour and solid black curves) with an overlay of the magnetic nozzle field lines (dashed black curves) for the 400 G, $\sim$ 170 W net deposited power, and 3 mg/s xenon propellant flow rate source operating condition.

keeping with this analogy, the electrons must be magnetized for some extent upstream of the sonic line to be compressed and accelerated to the sonic condition at the throat; the Hall parameter values of $70 - 200$ provides evidence that this criterion is met.

4.3.2 Ion-Neutral Collisions

A high density neutral population in the near-field region may also lead to frequent ion-neutral charge exchange collisions (CEX). These collisions act as a drag term on the ion fluid, preventing the ions from reaching sonic speeds until downstream of the high neutral pressure region, resulting in the throat shifting downstream into the plume. To assess the possible impact of this drag term the CEX mean free path (λ_{CEX}) can be compared to the characteristic length scale of ion acceleration. Since the ion acceleration appears to be governed by electrostatic acceleration (see Section 4.2) the relevant characteristic length scale for acceleration can be written as $(-\nabla\phi/\phi)^{-1}$. The ratio of CEX mean free path to acceleration length is then $-\lambda_{CEX}\nabla\phi/\phi$. If the CEX mean free path is shorter than the acceleration length scale ($-\lambda_{CEX}\nabla\phi/\phi < 1$) the ions are experiencing a drag force through frequent CEX

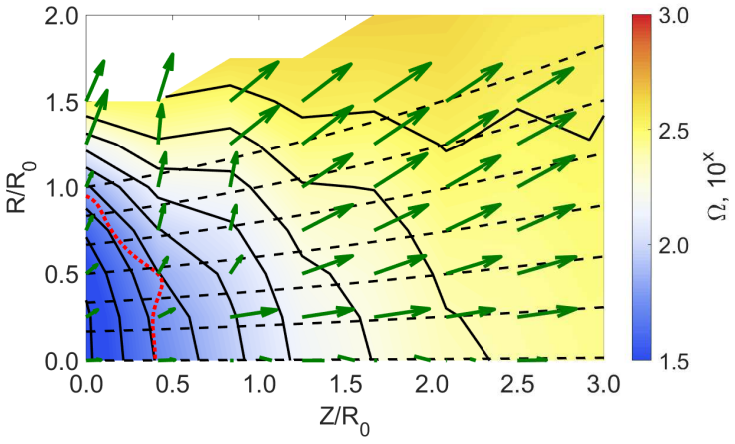

(a)

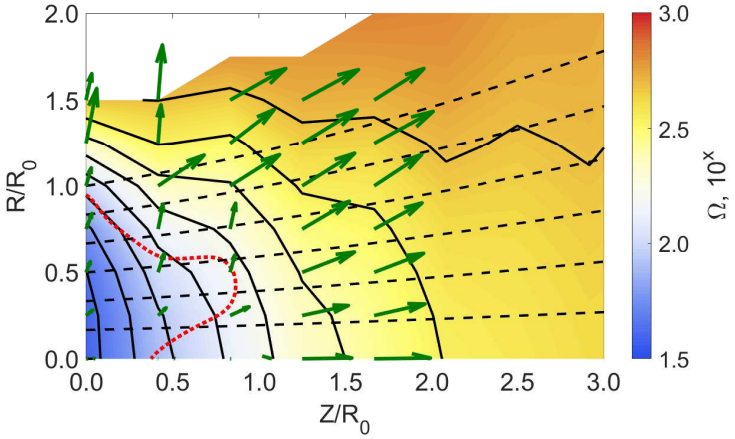

(b)

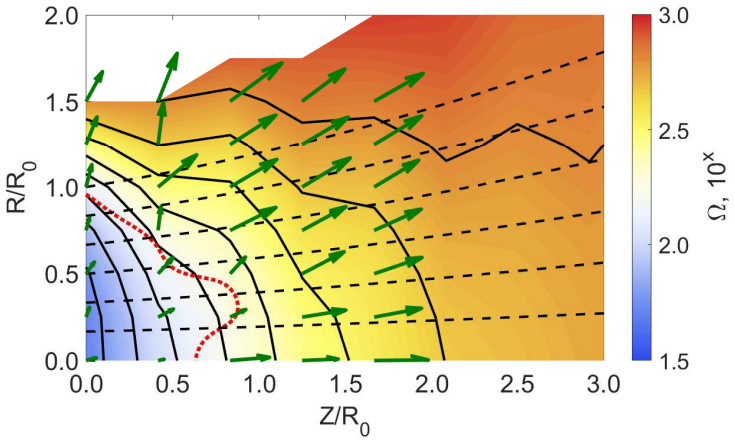

(c)

Figure 4.9: The electron-neutral Hall parameter (contour and solid curves) overlain with the magnetic nozzle (dashed curves) and ion sonic line (dotted curves) for the a) 200 G, b) 300 G, and c) 400 G source operating condition. For all conditions the net deposited power is $\sim$ 170 W and the propellant flow rate is 3 mg/s xenon.

collisions. Conversely, if $-\lambda_{CEX}\nabla\phi/\phi > 1$ the ion acceleration is not significantly impeded by these collisions. To quantify the role of CEX collisions within our low power test article, we track the centerline evolution of this ratio across four magnetic field conditions (see Figure 4.10). By tracking this parameter, we see that as the magnetic field increases the axial location at which the CEX mean free path becomes equal to the acceleration length scale ($-\lambda_{CEX}\nabla\phi/\phi = 1$) shifts downstream. This trend is influenced by two primary factors: 1) as the magnetic field increased the measured plasma density decreased. With a constant propellant flow rate across all device operating conditions, this necessitates a corresponding slight increase in the un-ionized neutral density in the near-field. This acts to decrease the CEX mean free path. 2) As the magnetic field increased we observed a decrease in the overall potential drop from source exit plane to the nozzle detachment plane. This acts to increase the characteristic acceleration length. Both of these effects act to shift the location of $-\lambda_{CEX}\nabla\phi/\phi = 1$ downstream. Significantly, this trend in $-\lambda_{CEX}\nabla\phi/\phi$ qualitatively matches the downstream movement of the ion sonic transition line with increasing magnetic field. This correlational evidence suggests that ion-neutral CEX collisions may play an important role in shifting the effective nozzle throat downstream. The collision-induced drag on the ions may delay the acceleration of the subsonic ions, resulting in the sonic condition being met at the downstream throat location.

4.3.3 Ionization within the Plume

In addition to the collisional processes discussed above, ionization may also play a role in pushing the ion sonic line downstream. The volumetric rate of ionization within the near-field plume region can be estimated from a control volume continuity analysis that balances ionization with the plasma flux out of the volume. Leveraging axisymmetry, assuming steady flow, and bounding the control volume to the region with LIF measurements (refer to Figure 4.2), this takes the form

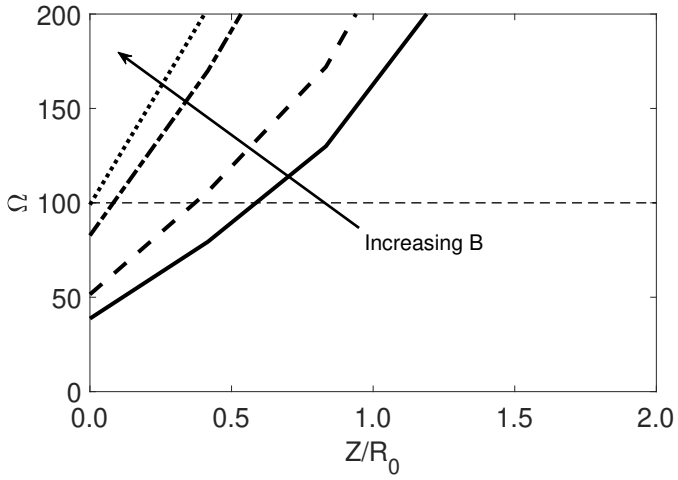

(a)

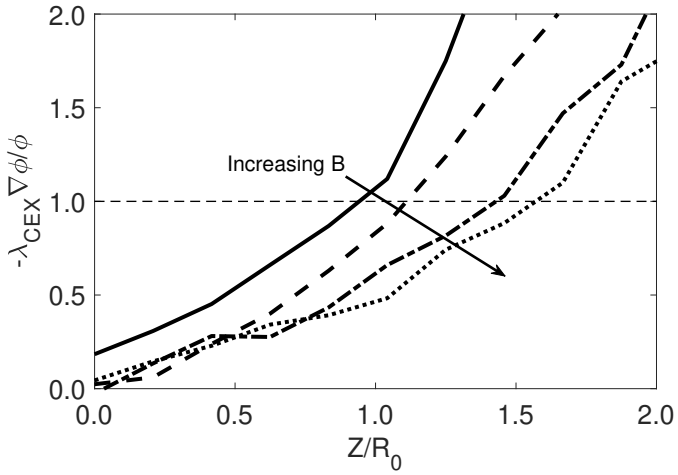

(b)

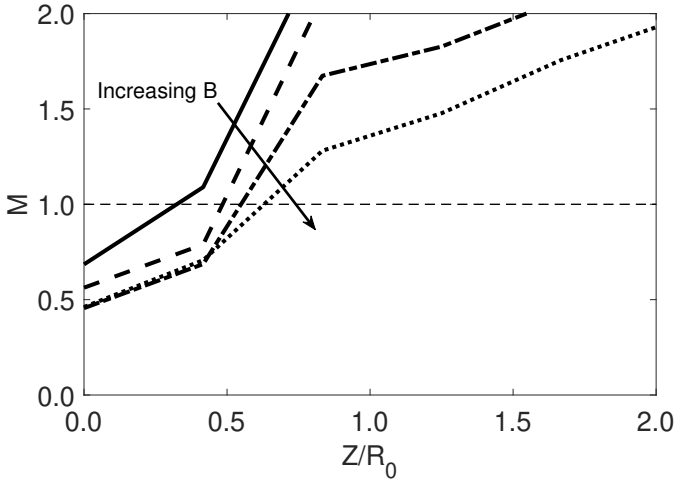

(c)

Figure 4.10: The centerline evolution of the a) electron-neutral Hall parameter, b) the ratio of the charge exchange mean free path and characteristic ion acceleration length scale, and c) the ion Mach number for the $300 - 600$ G operating conditions. For all operating conditions the net deposited power is ~ 170 W and propellant flow rate is 3 mg/s xenon.

$$K_{iz,p} = \frac{2\pi\Gamma_r R\ell + \pi\Gamma_a R^2 - \pi\Gamma_0 R_0^2}{\pi\bar{n}_g\bar{n}_e R^2\ell}, \tag{4.2}$$

where R is the radius of the cylindrical control volume, ℓ is the length of the control volume, and Γ_r, Γ_a, and Γ_0 are the particle fluxes through the radial, axial, and source exit plane boundaries, respectively. This volumetric ionization rate can be compared to the estimated ionization rate within the source tube — the location where the RF power is intended to be applied to the propellant. As shown in Figure 4.11, in the magnetic field conditions that exhibit a downstream throat the volumetric ionization rate within the near-field plume region is $15 - 35\%$ of the ionization rate within the source tube. This indicates that the RF power may be leaking into the near-field plume region. This behavior is consistent with numerical results for magnetically enhanced inductively coupled plasma processing units - devices with similar power coupling architectures and magnetic topologies - that also predict power coupling downstream of the primary ionization and heating region [165, 166]. While there is no clear trend in ionization rate within the plume compared to the magnetic field operating condition, the source conditions in which we observe a downstream effective throat location exhibit significant levels of ionization. This correlation suggests that it may play an important role in the near-field region, and, subsequently, the ion acceleration in that region. The ions that are born in the near-field plume region fall through a smaller potential drop than the ions born in the source tube - except, possibly, those ions that have undergone CEX collisions. This newly-ionized population may significantly reduce the mean ion speed within the fluid, thereby acting as an effective drag term on the ions. This phenomenon is discussed in further detail in a forthcoming paper by Wachs and Jorns [206].

The ultimate implication from the above discussion is that the low ionization fraction and corresponding high neutral density seems like a plausible explanation for the movement in the effective throat of the magnetic nozzle. This is evidence in

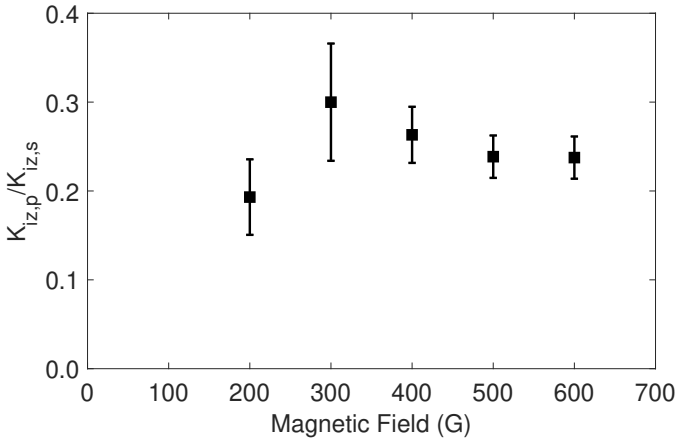

(a)

Figure 4.11: The ratio of the volumetric ionization rate in the near-field plume region (as bounded by the LIF measurements) and the volumetric ionization rate within the source region. For all magnetic field conditions the net deposited power is $\sim$ 170 W and propellant flow rate is 3 mg/s xenon.

support of the idea that modeling treatments of these systems at low power must be more nuanced, taking into consideration more than singly-charged, fully-ionized plasma. With that said, we recognize that three processes discussed here may not be the only or dominant driving factors, and their interactions with the plume expansion may vary between devices. Other near-field detachment processes have been recently identified [119] which may also have an effect here. The relationships we see, particularly with the charge exchange process, are compelling but correlational at this point.

4.4 Summary

In summary, the 2D plasma properties of an experimental low power magnetic nozzle plasma source operating at various magnetic fields have been measured using electrostatic probes and LIF. In all of the operating conditions, a high neutral density region is observed in the near-field. The ions initially leave the source region subsonically and the axial ion acceleration region is pushed downstream in high magnetic

field cases. The impact of this downstream movement of the throat on thrust performance is estimated using spatial plasma property maps to predict the thrust and specific impulse performance of the source. The measurement-inferred performance is compared to the expected performance of an ideal, fully attached nozzle operating at the same conditions; the performance of the low power device is $\sim 50-70\%$ of the ideal performance. This measured performance deficit is attributed to the reduced ion acceleration due to the effective shortening of the magnetic nozzle and the throat being pushed downstream. By adjusting the model initial conditions to match the empirical downstream throat properties, the predicted performance agrees with the results inferred from plume measurements. This finding is consistent with the recent work performed by Correyero, et. al. [113], though for a low power ECR source compared to our low power inductive source.

Three potential mechanisms that drive the ion sonic transition downstream are explored: electron-neutral collisions, ion-neutral collisions, and ionization within the plume. The electron-neutral collision mechanism is evaluated using a Hall parameter analysis. This indicates that the electrons become more magnetized closer to the source exit plane as the magnetic field strength increases. This runs counter to the measurement-inferred trend of the effective nozzle throat moving further downstream with increasing magnetic field, suggesting that this mechanism may not be directly responsible for the shift in the throat location. The impact of ion-neutral collisions, effectively a drag term on the ion fluid, is explored by comparing the CEX mean free path to the characteristic electrostatic acceleration length scale. On device centerline the trend in the downstream movement of the throat location and this parameter are positively correlated, suggesting that this mechanism plays an important role in the near-field expansion and ion acceleration. Finally, in the magnetic field cases that exhibit a downstream throat, the volumetric ionization rate in the near-field plume region is estimated to be $15-35\%$ of the ionization rate within the source. This

presence of ionization within the plume is correlated with the downstream shift in the effective nozzle throat. This suggests that ionization in the near-field may also play a role in the plasma-nozzle interaction. Overall, it is observed that in a low power magnetic nozzle test article a mechanism exists that shifts the nozzle throat downstream, effectively reducing thrust performance compared to ideal model predictions. As the research and development trends in the field shift toward developing low power versions of these devices, this finding suggests that it is necessary to include these low-ionization fraction effects in future models and iterations of these devices.

CHAPTER V

Impact of a Ring Discharge on Thrust Performance

5.1 Introduction

In this chapter we examine the performance of the low power magnetic nozzle test article operating in a "ring discharge" mode. It is our intent to examine how a "ring discharge," and the associated non-monotonic radial dependence of the plasma profiles, affects efficiency performance. This question is of particular interest because, to date, existing magnetic nozzle predictive models assume that plasma density is peaked on device centerline and rapidly decays toward the radial walls of the source region [84, 92, 94, 149, 152]. It is unclear if a deviation from this assumption significantly impacts the device performance.

To explore this question, we configure the plasma source and set the operating conditions such that a "ring discharge" structure develops. In Section 5.2 we provide a qualitative definition of a "ring discharge" structure using photographs and light intensity profiles. In Section 5.3 we present spatially-resolved plume maps of the exhaust structures and radially-resolved density measurements at the nozzle throat. Both data sets were obtained using the suite of electrostatic probes described in Chapter III. Using these experimental results, we are able to confirm that the test

article is accelerating the plasma, and apply the source and divergence efficiency architectures derived in Chapter II to determine both the measured and expected performance. We discover that the performance of the device is significantly lower than the predicted performance and quantify a radial-outwards shift in the plasma density with increasing magnetic field strength within the source region. We posit that this radial shift is a primary contributor to the observed performance discrepancy. In Section 5.4 we show that the power deposition within the test article is not radially uniform in any of our operating conditions, suggesting that the test article is operating in a true "ring discharge" mode as observed in plasma processing devices. This correlation allows us to conclude, as is done for plasma processing units, that there is a critical magnetic field threshold above which a "ring discharge" structure should form in our low power magnetic nozzle test configuration. We summarize our results and discuss the ramifications of these findings in Section 5.5.

5.2 Qualitative Results

To clarify what we mean by the "ring discharge" mode, we start with providing a qualitative description using axially-aligned photographs of the test article during operation and the corresponding light intensity profiles. When the source was operated with a 3-turn solenoidal antenna with a net deposited power of $\sim$ 170 W and a propellant flow rate of 0.5 mg/s of xenon, the visible structure within the source region changed as the magnetic nozzle strength was increased. Typically, for xenon, the light spectrum visible to the human eye is comprised of primarily excited neutral lines and a few ion lines [207]. However, assuming a moderately uniform neutral density within the source region, the light intensity may be correlated to the local power deposition because the region of maximum power deposition would result in a higher fraction of electrons exceeding the minimum energy threshold for excitation collisions.

At very low magnetic fields, the highest light intensity was peaked at the centerline, as shown in Figure 5.1 for the 40 G case. As the magnetic field strength was increased, the peak light intensity shifted radially toward the walls of the source tube and an intensity deficit began to appear on centerline, as illustrated by the 100 G and 400 G cases in Figures 5.2 and 5.3, respectively. These qualitative results are consistent with the description of "ring discharges" in magnetically-enhanced inductively coupled plasmas (MEICPs) found within the literature [165, 166, 208], hence our adoption of that naming convention.

5.3 Quantitative Experimental Results

In this section we present the measurements of the plasma properties necessary to evaluate the measured and model predictions for the source and divergence efficiency performance. The source was operated in the 1.9 cm OD solenoidal antenna configuration detailed in Chapter III. Refer to Figure 3.2 for a notional diagram of this configuration. These data were taken with the nozzle operating at $\sim$ 170 W combined deposited power into the transmission line and plasma source and 0.5 mg/s xenon propellant flow rate. We took measurements for magnetic field settings of 40, 100, and 400 G.

5.3.1 Probe Results

5.3.1.1 Plasma Properties

At each operating condition, we spatially mapped the plasma density, electron temperature, plasma potential, and axial ion current density from the nozzle throat to beyond the detachment location. We are able to confirm that the nozzle is accelerating the plasma and estimate both the source and divergence efficiency using these property maps. From the electron temperature maps in Figure 5.4, it is clear

(a)

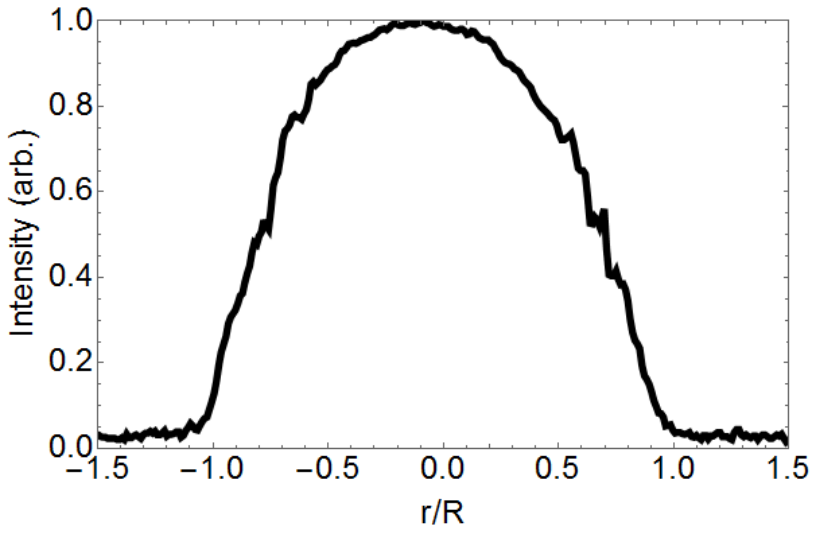

(b)

Figure 5.1: (a) A photograph (1/3000 s exposure) of the test article operating at $\sim$ 170 W, 0.5 mg/s of xenon, and a magnetic nozzle throat strength of 40 G. (b) The corresponding intensity of the visible spectrum axial light intensity of the discharge.

(a)

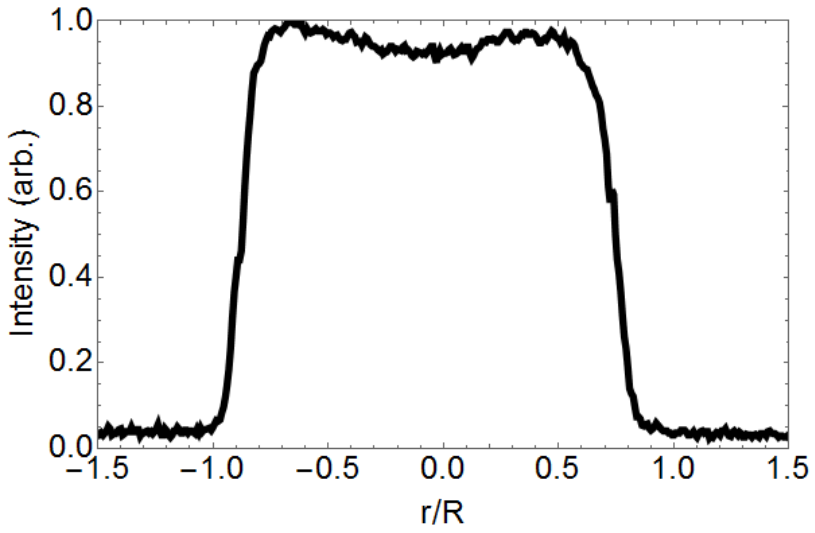

(b)

Figure 5.2: (a) A photograph (1/3000 s exposure) of the test article operating at $\sim$ 170 W, 0.5 mg/s of xenon, and a magnetic nozzle throat strength of 100 G. (b) The corresponding intensity of the visible spectrum axial light intensity of the discharge.

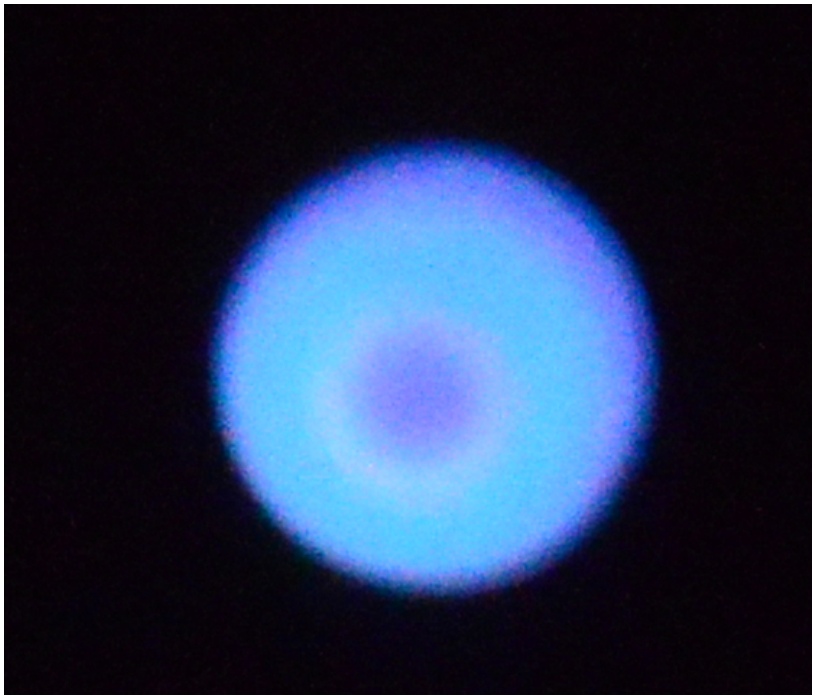

(a)

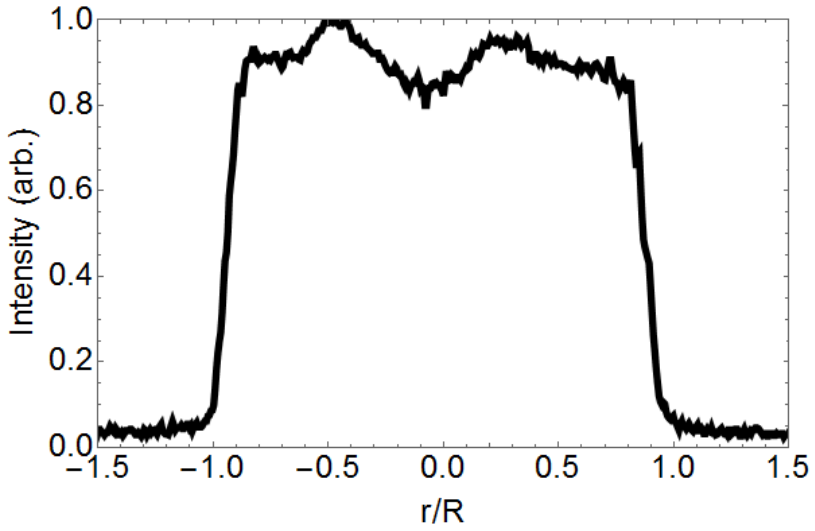

(b)

Figure 5.3: (a) A photograph (1/3000 s exposure) of the test article operating at $\sim$ 170 W, 0.5 mg/s of xenon, and a magnetic nozzle throat strength of 400 G. (b) The corresponding intensity of the visible spectrum axial light intensity of the discharge.

that the plasma is cooling, as it expands in the diverging nozzle section in all three operating conditions. This indicates that the plasma is not isothermal and is losing thermal energy during the expansion. Additionally, this cooling process is correlated with a decrease in the plasma potential as the distance from the exit plane increases, as indicated by Figure 5.5. This decrease in the plasma potential establishes an ion-accelerating electrostatic field. The plasma density profiles (Figure 5.6) provide further evidence of expansion - both axially and radially - in the diverging nozzle section; the highest density is concentrated at the source tube exit plane and decreases with increasing distance from this plane. This density decrease downstream is consistent with a decrease in the plasma pressure during the expansion through the nozzle. The convolution of the plasma density and the axial ion acceleration is captured in the current density maps in Figure 5.7.

There are a few interesting features within these spatial plasma maps. Firstly, in both the 100 and 400 G operating conditions, the electron temperature profiles exhibit a peak off of device centerline (refer to Figure 5.4). Secondly, we do not observe the formation of a potential well near the vacuum interface line. This potential well structure is often observed in magnetically confined plasmas [83, 201, 202, 203] and acts to counter finite transverse ion energies at the nozzle edges [83, 201]. Considering that the ions appear to be diverging faster than the nozzle field lines in Figures 5.6 and 5.7 — therefore the ions have finite transverse energy — the absence of this structure suggests that the magnetic nozzle may not be of sufficient strength the confine the expanding plasma. Finally, note that the highest plasma density and axial ion current density is located radially away from the device centerline. Interestingly these features - namely a centerline-peaked plasma potential accompanied by an off-center peaked electron temperature and plasma density profiles — are observed in at least one other magnetic nozzle device in the literature [88]. In the literature these structures are primarily attributed to the heating of the electrons via the skin

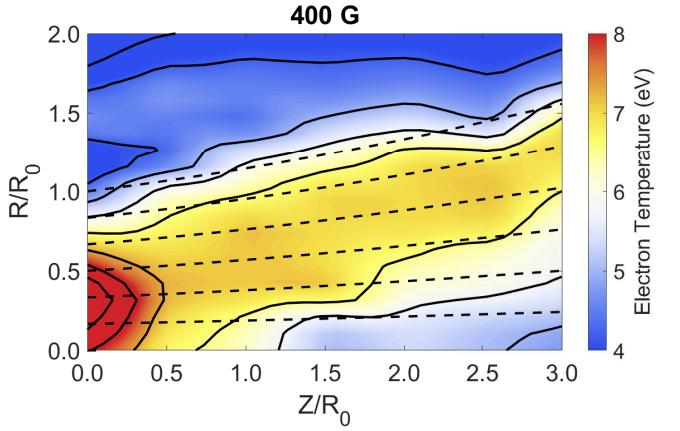

(a)

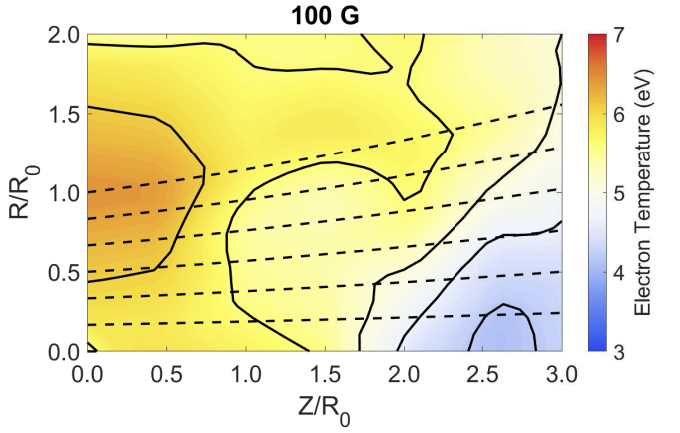

(b)

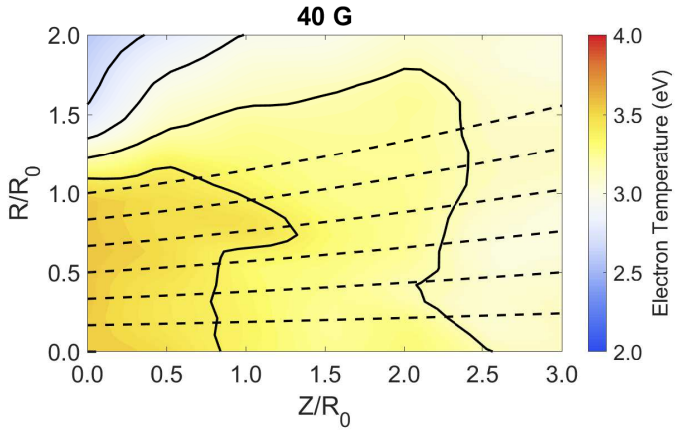

(c)

Figure 5.4: The electron temperature measurements for the a) 400 G, b) 100 G, and c) 40 G conditions (contour and solid curves), overlain by the magnetic nozzle field lines (dashed curves). Note that the source was operated at $\sim$ 170 W net deposited power and 0.5 mg/s of xenon

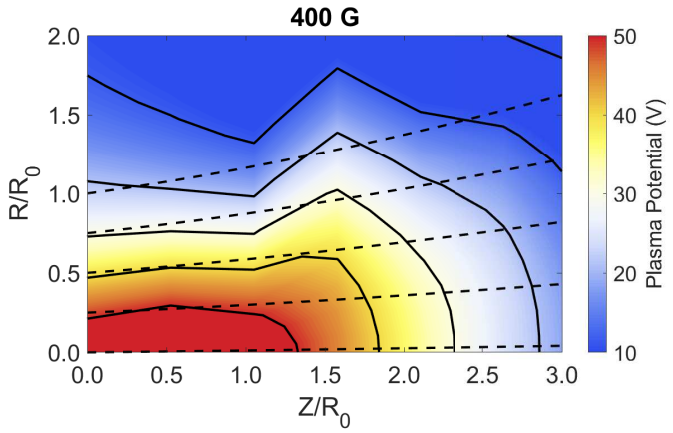

(a)

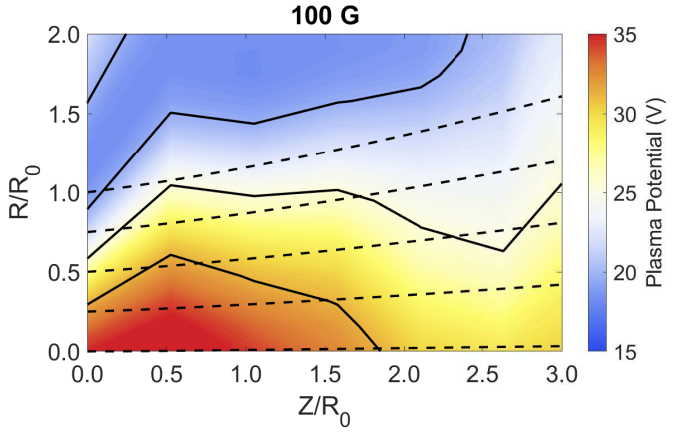

(b)

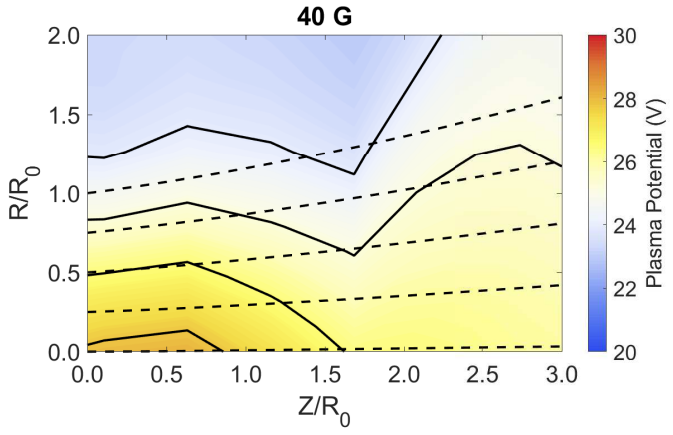

(c)

Figure 5.5: The plasma potential measurements for the a) 400 G, b) 100 G, and c) 40 G conditions (contour and solid curves), overlain by the magnetic nozzle field lines (dashed curves). Note that the source was operated at $\sim$ 170 W net deposited power and 0.5 mg/s of xenon

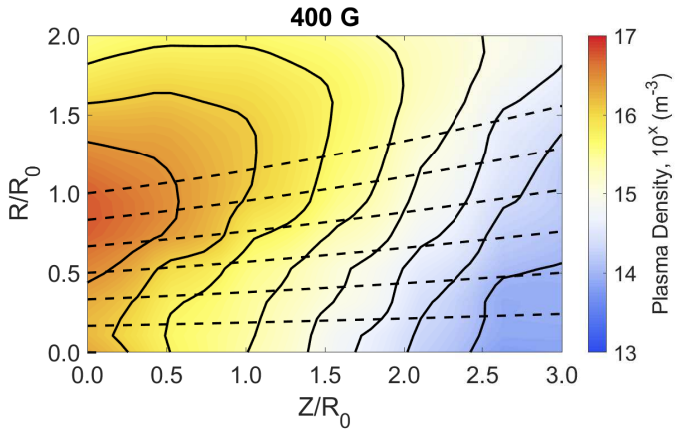

(a)

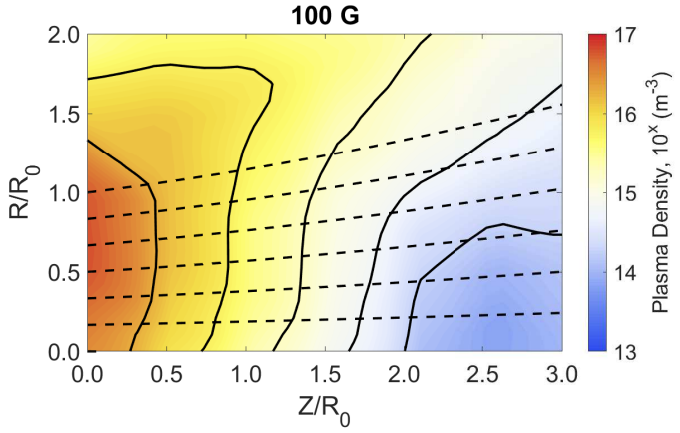

(b)

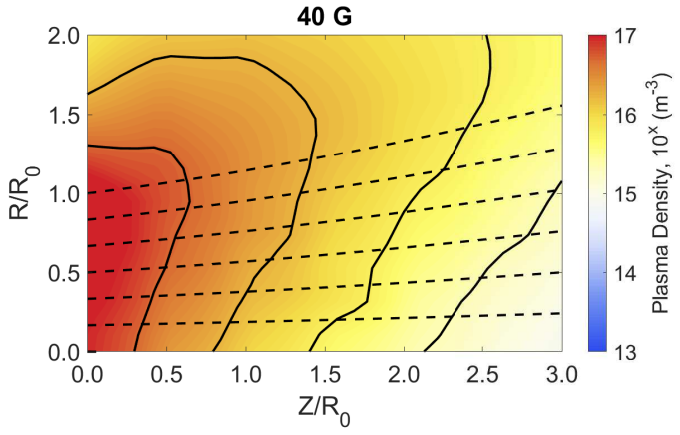

(c)

Figure 5.6: The plasma density measurements for the a) 400 G, b) 100 G, and c) 40 G conditions (contour and solid curves), overlain by the magnetic nozzle field lines (dashed curves). Note that the source was operated at $\sim$ 170 W net deposited power and 0.5 mg/s of xenon

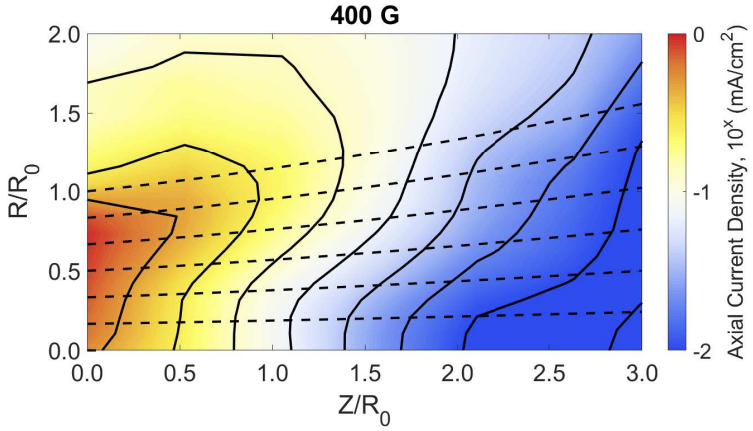

(a)

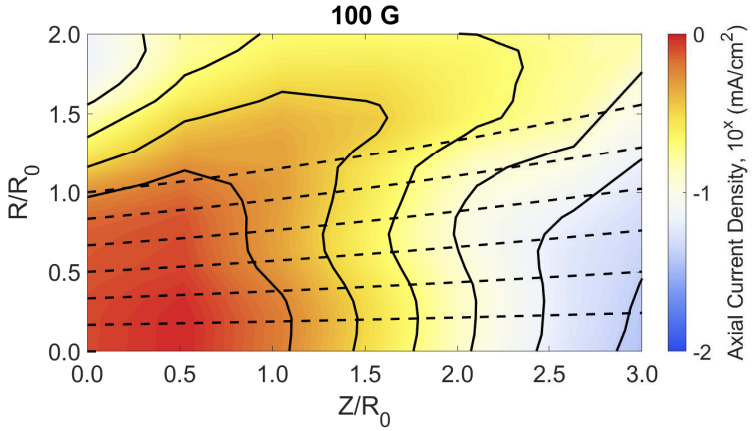

(b)

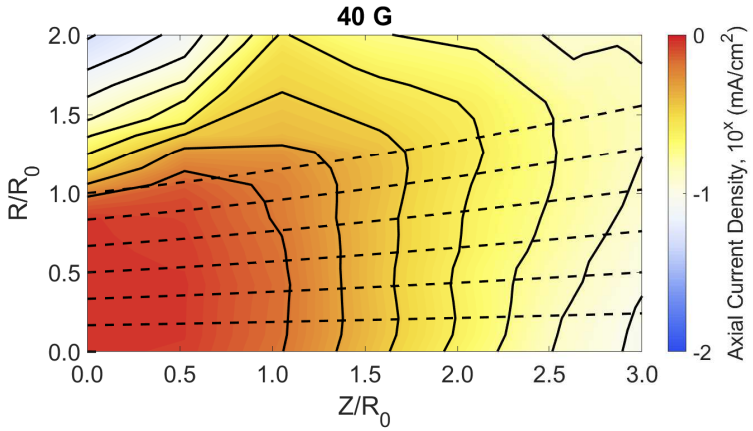

(c)

Figure 5.7: The axial Faraday probe measurements for the a) 400 G, b) 100 G, and c) 40 G conditions (contour and solid curves), overlain by the magnetic nozzle field lines (dashed curves). Note that the source was operated at $\sim$ 170 W net deposited power and 0.5 mg/s of xenon

effect [88]. Additionally, these structures may be enhanced by non-uniform power deposition within the plasma liner [165, 166]. To further corroborate this claim the skin depth can be estimated. For these conditions the skin depth decreases from ~ 1 cm to ~ 1 mm with our increasing magnetic field conditions, further suggesting that this structure is arises from the power coupling.

5.3.1.2 Polytropic Cooling

As indicated by the forms of the heat conduction power term ($P_Q \propto (5/3 - \gamma)/(\gamma - 1)$) and the the local sound speed ($c_s = \sqrt{\gamma q T_e / m_i}$) it is clear that the polytropic cooling index is an important parameter to quantify. We do so using the spatial electron temperature and plasma potential maps in Figures 5.4 and 5.5; since $d\phi/dT_e = \gamma/(\gamma - 1)$ we use linear regression of the plasma potential versus electron temperature [164, 204]. The linear regression fitting accounts for the error associated with the measurements and the error in the polytropic cooling index can be estimated by fitting to the extremes of the data, including error. The linear regression fitting for all three operating conditions can be found in Figure 5.8. The resulting polytropic index values derived from the measurements made along the device centerline can be found in Figure 5.9. For comparison, we also show the polytropic index in the adiabatic and isothermal limits. From these data $\sim 1.07 \leq \gamma \leq 1.17$. These results are within the range of measured values for electric propulsion devices operating on xenon [99, 114, 204, 205], and between the adiabatic ($\gamma = 5/3$) and isothermal ($\gamma = 1$) limits. By coupling these measurement-driven polytropic indices with our spatial plasma property maps, we are now able to estimate the heat conduction and local sound speed.

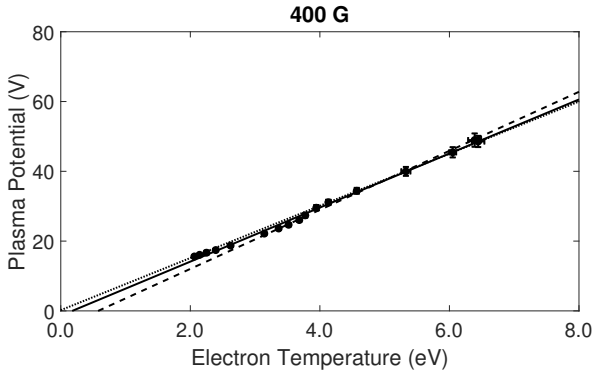

(a)

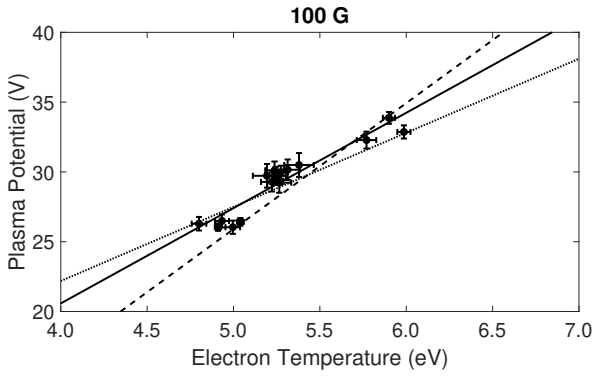

(b)

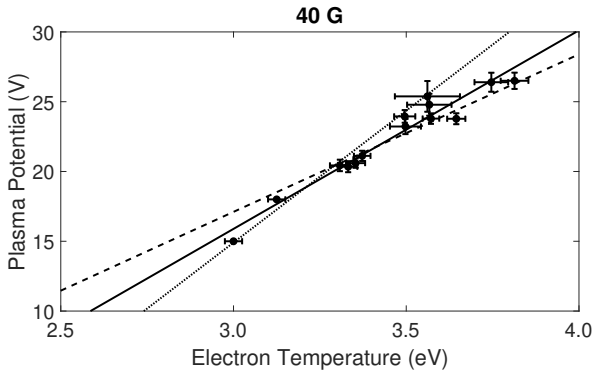

(c)

Figure 5.8: The polytropic index linear regression for the a) 400 G, b) 100 G, and c) 40 G conditions. The solid line is the best fit, while the dashed and dotted lines quantify the error. Note that the source was operated at $\sim$ 170 W net deposited power and 0.5 mg/s of xenon.

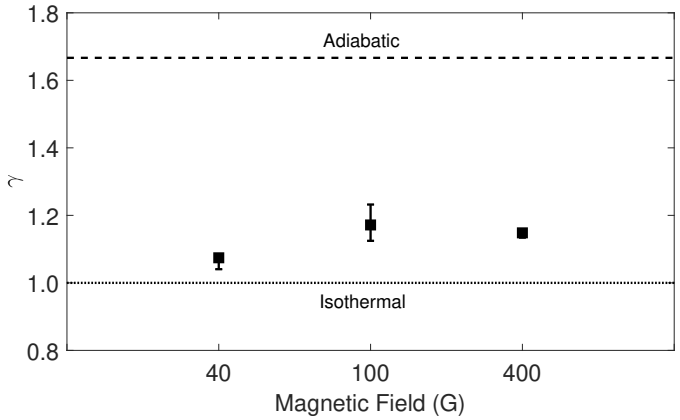

Figure 5.9: The value for the polytropic index at each operating condition. The dashed line in this figure denotes the adiabatic limit while the dotted line represents the isothermal limit.

5.3.1.3 Ion Acceleration

In most magnetic nozzle models, including our performance framework outlined in Chapter II, the plasma is assumed to be sonic at the location of peak magnetic field strength - the nozzle throat [83, 84, 85, 86, 92, 94, 96, 98, 114, 147, 149, 152, 164]. To confirm that our device is conforming to this assumption we can assume that the ions are singly charged and deconvolve the plasma density and axial ion current density data in Figures 5.6 and 5.7, respectively, to yield the local ion velocity (via $j = qn_e u$). The singly charged ion fluid assumption is typically satisfied for low temperature magnetic nozzle devices [83, 88, 94, 151]. We can combine the inferred ion velocity maps with the local sound speed (that, in turn, requires the polytropic index - Figure 5.9 - and electron temperature map - Figure 5.4) to ascertain the local axial ion Mach number. Given that the ion velocity is also assumed to be axial at the nozzle throat plane, this axial ion Mach number should be approximately sonic at that plane. As we show in Figure 5.10, the ions are sonic at the nozzle throat (located at $R/R_0 = 0$) and the axial Mach number increases as the plasma expands downstream, for all operating conditions. This confirms that our second test article configuration (1.9 cm diameter liner) is notionally behaving as expected of a magnetic nozzle: the ions are

accelerated to sonic at the nozzle throat and continue to accelerate as they expand throughout the plume. This contrasts with the first test configuration described in Chapter IV. The more ideal behavior in this configuration — the presence of sonic ions at the peak magnetic field location — is due to the reduced propellant flow rate required for operation, which is facilitated by improved power coupling.

Note that the axial ion Mach number, while an important parameter throughout the plume, can be misleading in terms of ion acceleration. Due to the polytropic cooling of the electrons as they expand in the plume - the electron temperature decreases - the local sound speed decreases, and the Mach number correspondingly increases, even if the ion velocity remains constant. This effect requires us to examine the ion velocity directly to determine the downstream axial plane at which the ions are no longer accelerated. Like we did in Chapter IV, the location at which the ion velocity plateaus can be used as a proxy for the detachment location. The diverging nozzle section accelerates the ions, so the location at which the ions cease being accelerated should indicate that the nozzle is no longer influencing the ion fluid - therefore the ions are effectively "detached" from the nozzle at this location. As shown in Figure 5.11, the ion velocity appears to have plateaued at $(Z/R_0) \sim 8$. This effective detachment plane holds across all test article operating conditions. We can now combine this effective detachment plane with the axial ion current density map to track the spatial evolution of the plume current and, thereby, estimate the divergence efficiency using the techniques outlined in Chapter III.

5.3.1.4 Exit Plane Density

To complement the divergence efficiency analysis that is enabled by the identification of the effective detachment plane, we can also estimate the source efficiency using the plasma measurements at the nozzle throat, if we assume that the profiles are self-similar throughout the source region. For clarity, we separately plot the nor-

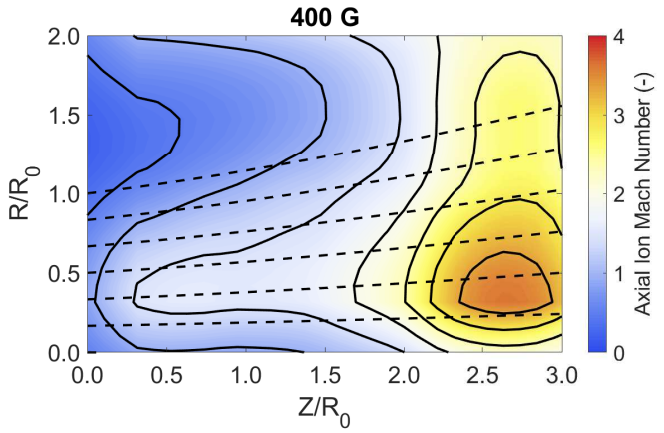

(a)

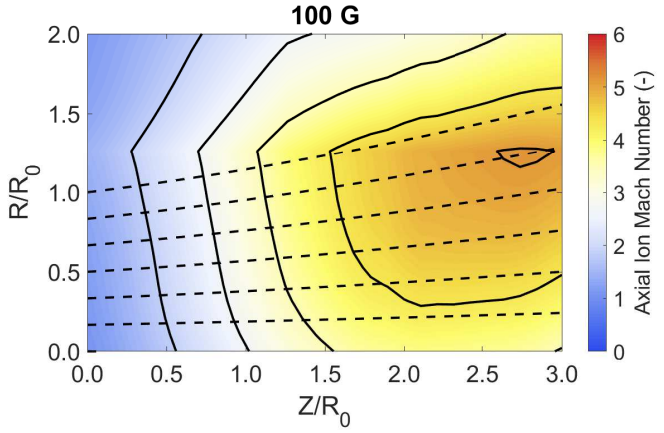

(b)

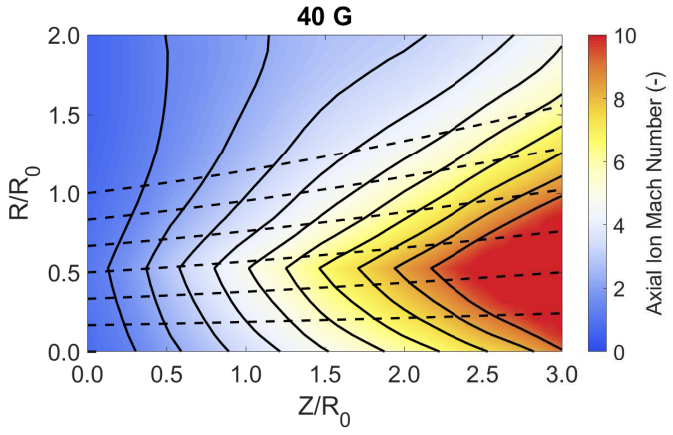

(c)

Figure 5.10: The axial ion Mach number for the a) 400 G, b) 100 G, and c) 40 G conditions (contour and solid curves), overlain by the magnetic nozzle field lines (dashed curves). Note that the source was operated at $\sim$ 170 W net deposited power and 0.5 mg/s of xenon

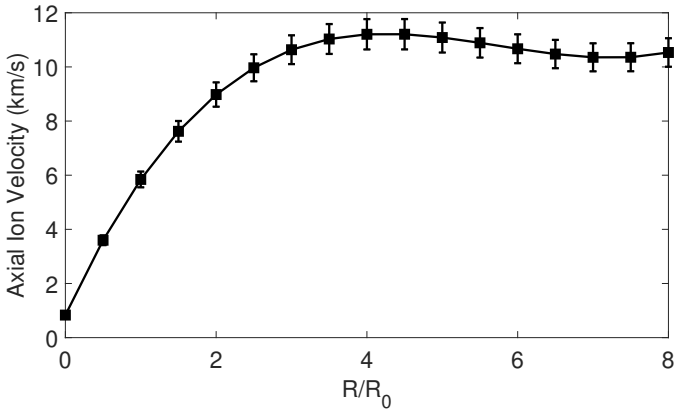

Figure 5.11: The axial evolution of the centerline ion velocity for the 100 G condition. In this condition the net deposited power is $\sim$ 170 W and propellant flow rate is 3 mg/s xenon.

malized plasma density at the nozzle throat in Figure 5.12. From these results it is clear that the plasma density displays a non-monotonic radial dependence, with the peak density measured radially away from the device centerline. This is in direct contradiction to the center-peaked plasma density profiles that are measured [83, 94] and assumed within the 2D moderate-power magnetic nozzle performance models [147, 152]. However, we reiterate that this is not the only device to observe this non-monotonic radial density dependence - Takahashi et. al. have also observed this trend [88].

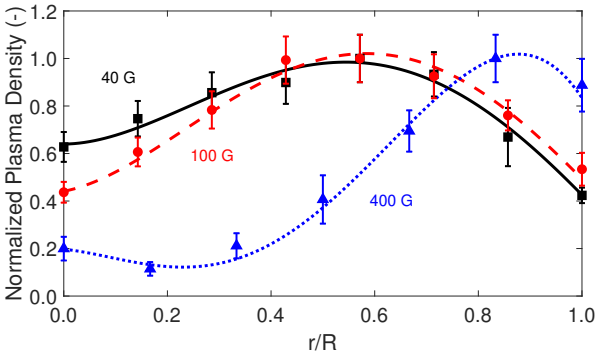

Figure 5.12: The measured plasma density and the associated polynomial fit at the nozzle throat for the 40 G (squares/solid curve), 100 G (circles/dashed curve), and 400 G (triangles/dotted curve). Note that the source was operated at $\sim$ 170 W net deposited power and 0.5 mg/s of xenon at each magnetic field condition.

In the literature two plasma density profiles at the throat have been commonly used: a profile that can be described by the sheath edge-to-center density ratio [94] and a non-uniform jet profile [147, 152]. The sheath edge-to-center profile [94] takes the form of

$$n_{sdr}(\rho) = \left[1 - \left(1 - h_R^{1/6}\right)\rho^2\right]^6, \tag{5.1}$$

where h_R is sheath edge-to-center density ratio defined as

$$h_R \approx \frac{0.4}{\sqrt{1 + 0.68(R_0/r_{ci})^2}}. \tag{5.2}$$

Here ρ is the non-dimensional radius (r/R_0) and r_{ci} is the ion cylcotron radius. Note that r_{ci} is dependent on the magnetic field strength. At high magnetic field strengths h_R diminishes, and the density profile becomes more pronouncedly center-peaked. In contrast, the non-uniform jet profile is generally independent of the magnetic field strength and takes the form [147, 152]

$$n_{nuj}(\rho) = J_0(a_0\sigma\rho), \tag{5.3}$$

where J_0 is the Bessel function of the first kind, a_0 is the first zero of J_0 ($a_o \approx 2.405$), and σ is a parameter that measures the radial non-uniformity of the plasma density. Like the sheath edge-to-center density profile, the non-uniform jet profile exhibits a strong peak along device centerline, especially with the commonly used $\sigma = 0.99$. To contrast our measured plasma density profiles (Figure 5.12) at the nozzle throat with these expected profiles, we plot the sheath edge-to-center density and non-uniform jet profiles in Figure 5.13. For the sheath edge-to-center density profiles, we use our magnetic field operating conditions (40, 100, and 400 G). For the non-uniform jet profile we use $\sigma = 0.99$. It is clear from the differences between our measurements (Figure 5.12) and the expected profiles (Figure 5.13), there may be

mechanisms present within the source tube region that are not commonly observed within the magnetic nozzle literature nor are accounted for in prominent magnetic nozzle performance models. We reserve a discussion regarding a physical mechanism that may explain this behavior for Section 5.4.

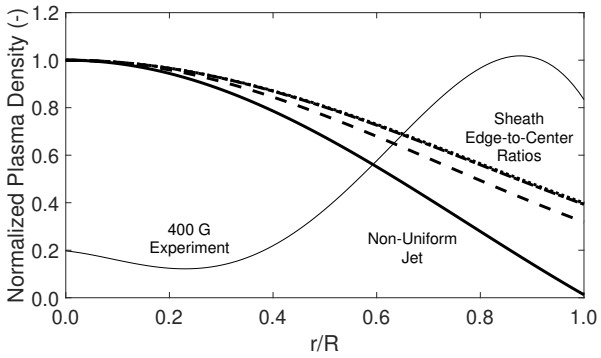

Figure 5.13: The expected plasma density profiles at the nozzle throat according to the non-uniform jet model [147] with $\sigma = 0.99$ (solid curve), or the sheath edge-to-center fitting proposed by Lafleur [94] for a 400 G (dashed curve), 100 G (dot-dashed curve), and 40 G (dotted curve) nozzle throat strength. Note that the latter two conditions are nearly identical due to the low magnetic field strength. For comparison, the measured density profile for the 400 G condition is included (thin solid curve).

5.3.2 Device Performance Metrics

5.3.2.1 Source Efficiency

If we assume that the plasma profiles that we measure at the throat are self-similar throughout the source region, we can use the measurements presented in the previous section to calculate the source efficiency. To this end we calculate the power incident on all of the surfaces of the cylindrical plasma liner using the framework described in Chapter II. As part of the process of determining the source efficiency we analyze the power flowing into the diverging nozzle section. The energy stored in the four modes of the plasma - the ion kinetic energy, electron pressure, heat conduction, and ion production cost - is summarized in Figure 5.14. Across all operating conditions, the most power is trapped within the ion production cost term. This is due to

the relatively low electron temperatures (a maximum of $T_e \sim 8$ eV for the 400 G condition), which results in an ion production cost of ~ 70 eV/ion. It is important to note that ion production costs are effectively "frozen flow" losses - the energy stored within this mode cannot be converted into directed kinetic energy by the diverging nozzle section, so it is advantageous to minimize this term. Operating the test article at the higher magnetic field conditions increases the electron temperature, which accordingly reduces the ion production cost (refer to Eq. 2.40). However, the increase in electron temperature with increasing magnetic field is not predicted by a global 0D power balance; within the global model an increase in the magnetic field strength at the radial walls is expected to reduce plasma recombination at the walls. In the global model a reduction in the radial losses results in a lower electron temperature required to balance these losses. The opposite trend in our measurements suggests that the assumption underpinning the global power model that power is uniformly deposited throughout the volume may be violated within our test article - namely that non-uniform power deposition may play a significant role.

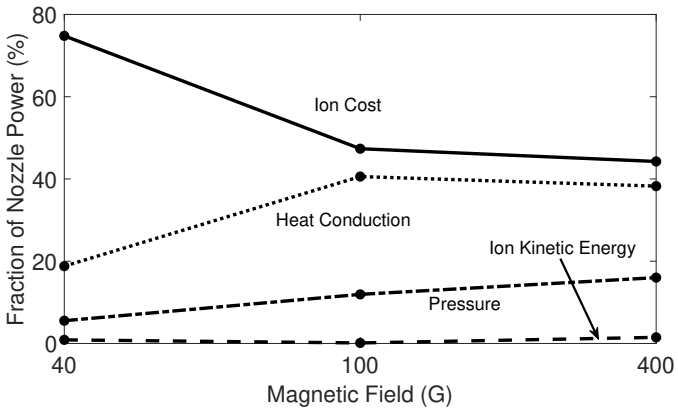

Figure 5.14: The percentage of the power flowing into the nozzle that stored in various energy modes of the plasma. Note that for all conditions the source was operated at ~ 170 W net deposited power and 0.5 mg/s of xenon.

In addition to the power entering the nozzle, we can estimate the power incident on the radial walls of the plasma liner. Due to the reduced propellant flow rate —

and associated lower neutral density in the source tube — in this analysis we assume that the electrons are fully magnetized, but the ions are not magnetized. In the test article the ion gyroradius exceeds the plasma liner radius ($r_{L,i} > R_0$), so the latter assumption should be valid. These assumptions state that the ion fluid is the species impinging on the radial walls, so we estimate the radial ion kinetic energy and the ion production cost that is lost when ions recombine at the wall. The spatial plasma maps can be combined with the radial ion momentum equation to allow for estimation of the radial ion velocity across the throat plane. Armed with the radial ion velocity and the plasma properties adjacent to the liner walls, we can estimate the power lost to the radial wall. These results are summarized in Figure 5.15. We can estimate the source efficiency for the test article by combining the results from the nozzle power analysis and the radial wall losses - this efficiency can be found in Figure 5.16. For comparison, we calculate the source efficiency using the sheath edge-to-center and non-uniform jet profiles, assuming that only the density profile is changed. Across all of the test article operating conditions $\eta_{loss} \leq 30\%$. This states that the maximum efficiency of the device is less than 30%. From the results in Figure 5.16 it is clear that the radial losses of the test article are much higher than predicted, primarily due to the enhanced plasma density adjacent to the source walls. We discuss a possible explanation for this behavior in Section 5.4.

5.3.2.2 Divergence Efficiency

We can determine the divergence efficiency of the test article by tracking the current density evolution throughout the plume (refer to Figure 5.7). The calculated divergence efficiency across the test conditions can be seen Figure 5.17. We also show the predicted divergence efficiency of the device by assuming that the density profile at the throat can be described by the sheath edge-to-center [94] or the jet [147, 152] models and that the ion fluid follows the nozzle streamlines from the nozzle throat

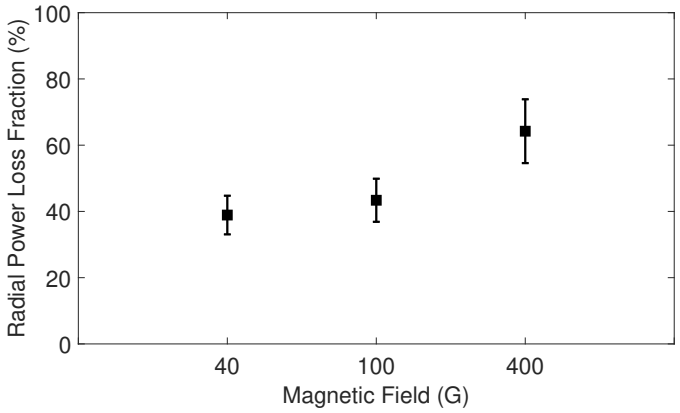

Figure 5.15: The percentage of the total absorbed power that is lost to the radial walls. Note that for all conditions the source was operated at ~ 170 W net deposited power and 0.5 mg/s of xenon.

to the far-field detachment plane. From the Faraday probe results in 5.17, this latter assumption appears to be dubious — the ions appear to diverge outwards more rapidly than the nozzle lines — but without a simple, self-consistent expansion model that includes detachment, it is difficult to accurately predict the ion streamlines. In any case, the divergence efficiency of the test article is low ($\leq 65\%$). This low divergence efficiency may be due to a combination of the high off-axis density at the nozzle throat (see Figure 5.12) and the enhanced cross-field transport arising from the pressure and potential gradients (refer to Figures 5.4 - 5.6) within the diverging plume. It is clear from plotting the divergence efficiency using the predicted plasma density profile shapes at the nozzle throat that the divergence efficiency performance is degraded with increasing plasma density along the vacuum interface line. Due to the compact nature of the test article the discrepancy in the divergence efficiency for the sheath edge-to-center and jet profiles is $\sim 1\%$. This small difference is primarily due to the minimal divergence of the nozzle field lines — the coordinates of the vacuum interface line at the detachment plane are $(Z/R_0, R/R_0) = (8, 3)$ — rather than differences in the plasma density at the wall. In a thruster with a different geometry, the effect of an enhanced plasma density at the radial wall may have a more pronounced effect on

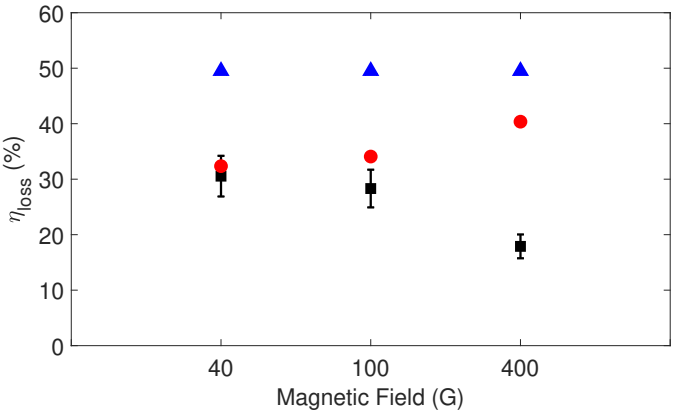

Figure 5.16: The measurement-driven source efficiency of the test article (squares) compared to the predicted efficiency if the density adhered to the sheath edge-to-center profile [94] (circles) or the non-uniform jet profile with $\sigma = 0.99$ [147] (triangles). For the experimental values the source was operated at ~ 170 W net deposited power and 0.5 mg/s of xenon across all magnetic field conditions.

the divergence efficiency. We discuss this possible impact further in Section 5.4.

5.4 Discussion

In this section we further examine the possibility of non-uniformly deposited power within the test device. Until now we have provided qualitative and correlational evidence that the power is being non-uniformly deposited. In this section we strive to quantitatively show that this is the case, and attempt to correlate the peak power deposition with the radially outward shift in the peak in the throat density profile. We follow this with a discussion of the dependence of efficiency performance on device design — particularly source geometry — in light of this non-uniform power deposition effect.

5.4.1 Radial Power Deposition

To quantitatively discuss non-uniform power deposition we combine the theoretical framework outlined in Section 2.4 and the plasma measurements at the nozzle throat in Section 5.3. Our approach splits the cylindrical source region into many

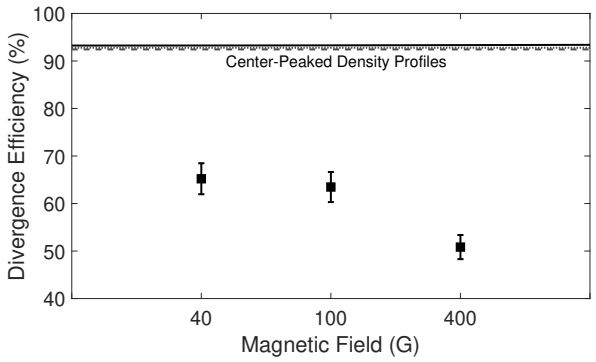

Figure 5.17: The measured divergence efficiency (squares) compared to the predicted values if the throat density profile followed the Lafleur [94] model (solid curve), the uniform jet (dashed line), and the non-uniform jet (dotted line). The latter two profiles use the Bessel function form proposed by Ahedo and Merino [147]. Note that in all of the predicted models the testbed nozzle topography is used; only the throat density profile is changed.

cylindrical shells and estimates the power deposited into each shell through a control volume analysis. This analysis balances the energy incident on all control volume surfaces, including the radial flow of energy into other shells, with the power deposited into the shell. The resulting fraction of the total power deposited as a function of the normalized source radius is shown in Figure 5.18. From these results it is clear that as the magnetic field within the source region increases the location of the peak power deposition shifts radially outward. In the lowest magnetic field case the power deposition is peaked close to the device centerline, while for the highest magnetic field case the maximum deposition is adjacent to the source walls. Through a comparison of these results with the plasma density profiles at the nozzle throat (refer to Figure 5.12), it becomes immediately apparent that the locations of increased power deposition and the peak in the density profile are correlated. The differences in the locations of maximum power deposition and density may be due to collision-induced cross-field transport within the source region and enhanced high energy tails within the electron energy distribution leading to locally higher rates of ionization. Interestingly, Kinder and Kushner [165, 166] note that non-uniform power deposition within

magnetically-enhanced inductively-coupled plasma processing units is driven by the antenna geometry and radiation pattern, plasma species, and magnetic field topography. So, given the correlation between non-uniform power deposition and the radial shift in the peak density at the nozzle throat for our solenoidal antenna-driven test article, coupled with the corresponding degradation of the device efficiency performance, it is clear that this effect must be considered at all stages of the thruster design process to avoid low efficiency performance. Due to the complex nature of power coupling to a plasma in the presence of a magnetic field incorporating a model that can accurately predict power deposition into the early design phases is recommended.

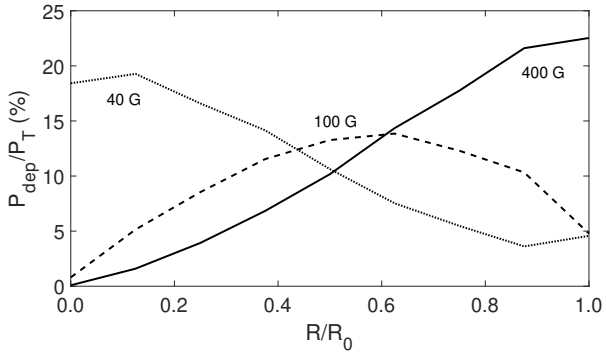

Figure 5.18: The percentage of the total absorbed power as a function of radial position for the 400 G (solid), 100 G (dashed), and 40 G (dotted) operating conditions. For all magnetic field conditions the net deposited power is $\sim$ 170 W and propellant flow rate is 3 mg/s xenon.

5.4.2 Design Considerations

Within this work we have correlated an increase in the plasma density adjacent to the source wall with decreased source efficiency and degraded divergence efficiency. However, we have tested in only one device configuration, with a single source aspect ratio ($R_0/L_S = 0.5$). If we assume that the power deposition and plasma density profiles do not change while increasing the radius of the source tube we can gain insight into approximate trend in efficiency performance relates to the device geometry.

Under these assumptions, the trend in the source efficiency is outlined in Figure 5.19. It is clear that for increasing source tube radius the source efficiency is increased. This is physically due to the smaller fraction of the total absorbed power that is lost to the radial walls of the source tube; the surface area of the radial walls is a smaller fraction of the total surface area of the control volume. Even with improved source aspect ratio the efficiency remains low ($< 50\%$) across values that may be suitable for microsatellite propulsion devices. This suggests that the aspect ratio of the source tube of a magnetic nozzle should generally be as high as possible to reduce the fraction of the power that is lost to the radial walls, but may be limited by the volume constraints of the device.

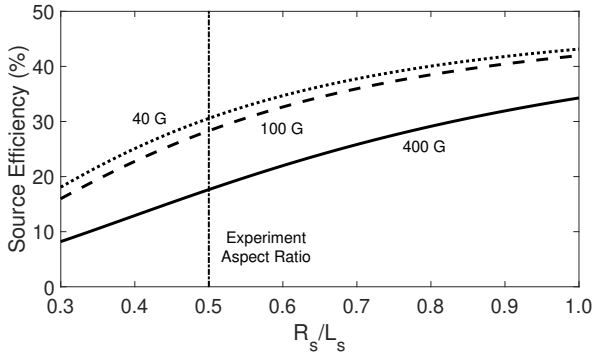

Figure 5.19: The source efficiency as a function of the plasma liner aspect ratio (R_S/L_S) assuming that the 400 (solid curve), 100 (dashed curve), and 40 G (dotted curve) power density and plasma density profile shape does not change. The test article aspect ratio is 0.5, and is denoted by the dot-dashed vertical line.

Using the above assumptions regarding power deposition and density profile, we can also examine the trend in the divergence efficiency with changing source aspect ratio. In Figure 5.20 we show this trend for the 400 G experimental and sheath edge-to-center, and the $\sigma = 0.99$ non-uniform jet profiles. To close the analysis we have further assumed that the ion fluid remains attached to the diverging nozzle section from the nozzle throat to the detachment plane, the ion speed is uniform across the nozzle section, and that the detachment plane remains fixed at $(Z/R_0) = 8$. From

these results it is clear that the divergence efficiency is improved with decreasing source aspect ratio. This is largely due to the slow divergence of the magnetic field lines within the nozzle core compared to those near the nozzle edges, as notionally illustrated in Figure 5.21. For profiles with enhanced density near the nozzle edges — adjacent to the source walls — a larger fraction of the plasma momentum is turned radially by the magnetic field lines. This results in a reduction in the divergence efficiency. When combined with the source efficiency trend above, this suggests that there is an optimal geometry that maximizes the product of these two efficiency terms. For the 400 G operating condition of our test article, and under the assumptions listed, a doubling in the source aspect ratio from 0.5 to 1 yields an increase in the source efficiency from $\sim 18\%$ to $\sim 34\%$ while divergence efficiency decreases from $\sim 92\%$ to $\sim 67\%$. As shown in Figure 5.22, this trade would result in a convolved maximum efficiency increase from $\sim 16\%$ to $\sim 23\%$. The peak in Figure 5.22 suggests that there is an optimal source aspect ratio for the convolved divergence and source efficiency terms. Note that this is for the product of the source and divergence efficiency terms only, but due to the nature of the total efficiency expression this indicates a maximum total efficiency value. From these possible efficiency gains it is clear that these types of considerations must be accounted for during the design of a thruster to yield maximum performance.

5.5 Summary

In summary, the 2D plasma properties of an experimental low power magnetic nozzle plasma source operating with a solenoidal antenna at three magnetic field conditions have been mapped using electrostatic probes. In all three conditions a radially outward shift in the plasma density profile peak is both qualitatively and quantitatively observed at the nozzle throat. This density profile shape is not commonly observed in other experimental devices or used in existing 2D nozzle models.

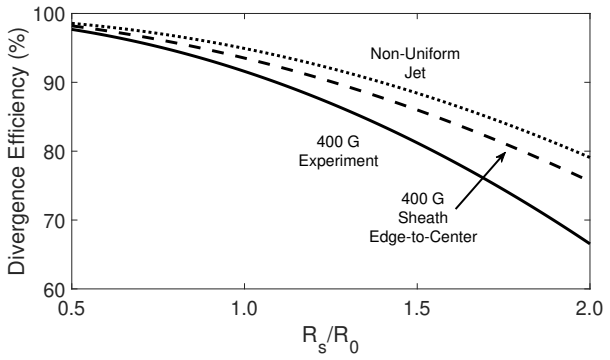

Figure 5.20: The divergence efficiency as a function of the source radius (R_S/R_0), using the measured 400 G (solid curve), 400 G sheath edge-to-center [94] (dashed curve), and the $\sigma = 0.99$ non-uniform jet [147, 152] (dotted curve) plasma density profiles.

Instead, the commonly used density profiles at the nozzle throat predict a peak density on device centerline and a monotonic decay with increasing radial distance from that axis. The measured enhanced density adjacent to the source tube walls leads to increased radial wall losses and a corresponding decrease in the source efficiency compared to the predicted values using the center-peaked density profiles. The radial outward shift in the peak density also results in a reduced divergence efficiency due to enhanced radial momentum losses caused by the turning of the plasma by the highly divergent magnetic field lines at the magnetic nozzle edges.

We posit that the non-monotonic radial dependence of the measured throat density profile arises from non-uniform power deposition within the source tube. We show that power is non-uniformly deposited within our test device by combining measurements of the properties at the throat with a control volume analysis that decomposes the cylindrical source tube region into discrete cylindrical shells. The estimated power deposition profiles in our device are correlated with the plasma density profiles; regions of high density correlate with high power deposition. In the power deposition and plasma density profiles an increase in magnetic field results in a radially outward shift in the peak of both profiles for our test article. This suggests that the enhanced

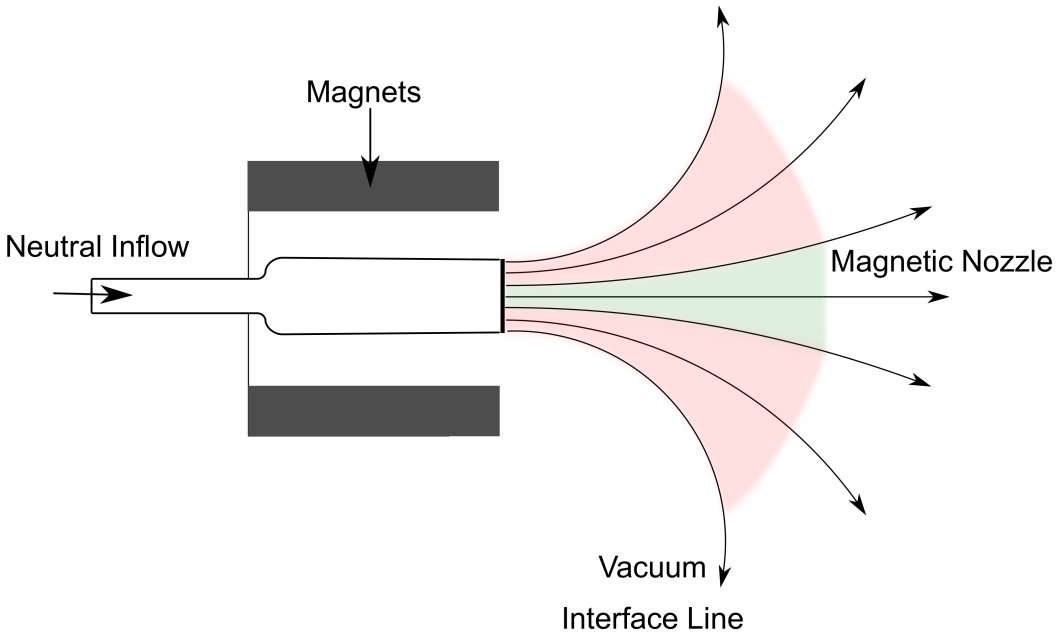

Figure 5.21: A notional magnetic nozzle depicting the enhanced divergence of the nozzle field lines away from device centerline (red shaded region) compared to the relatively low divergence of the nozzle core (green shaded region). A clustering of the plasma density inside the red region results in degraded divergence efficiency performance.

plasma density adjacent to the source walls is caused by power deposition effects arising from an interaction of the magnetic field and antenna-plasma coupling. This finding is consistent with observations in magnetically-enhanced inductively-coupled plasma processing devices that operate in configurations similar to magnetic nozzles [165, 166].

Leveraging this insight we explore the dependence of the source and divergence efficiencies on device geometry. Assuming that the power deposition and density profile shapes do not change, we vary the aspect ratio of the source tube by increasing the radius and examine the impact on these efficiency terms. We find that as the aspect ratio is increased an increase in the source efficiency is predicted. This is

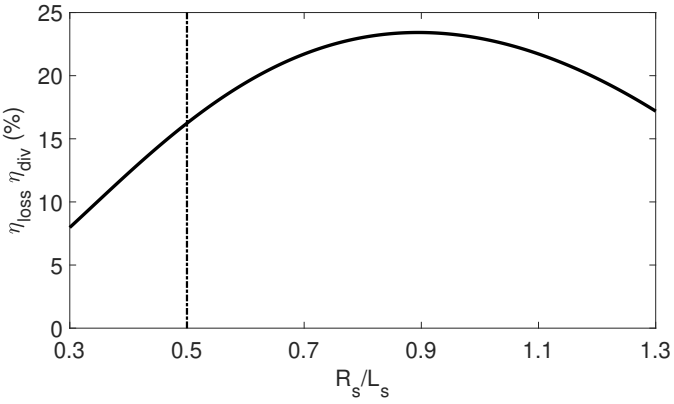

Figure 5.22: The product of the divergence and source efficiency terms as a function of the source aspect ratio (R_S/L_S) for the measured 400 G operating condition. The test article aspect ratio is 0.5, and is denoted by the dot-dashed vertical line.

balanced by a predicted decrease in the divergence efficiency with increasing aspect ratio. Overall, the trade between these two terms suggests that there is an optimal geometry design that results in a maximum efficiency performance. As the research and development trends in the field continue to shift toward developing new thrusters with improved performance, these findings suggest that it is necessary that future design tools and predictive performance models include robust power deposition models to aid in design decision-making and to maximize device efficiency.

CHAPTER VI

Estimated Performance of a Device Incorporating Lessons Learned

6.1 Introduction

In this Chapter we demonstrate that the performance of a low power magnetic nozzle can be improved by adjusting the design of the device and selecting appropriate operating conditions. This exercise is of interest because it materially demonstrates that these effects can be minimized or eliminated by incorporating the design recommendations arising from our findings in Chapters IV and V. To accomplish this end, we have implemented a refined test article with features intended to mitigate the non-ideal effects identified in the previous chapters. This is largely accomplished by employing a planar RF heating scheme instead of solenoid configuration. In the following, we examine both the exhaust structures present within the diverging nozzle section and the properties at the nozzle throat. Using these results we are able to confirm that the nozzle is accelerating the plasma and quantify the thrust and efficiency performance terms.

We discover that our modified design yields modest gains in the thrust and many of the efficiency terms. In Section 6.3 we demonstrate that the power deposition is uniform across 70% of the source tube radius in this new configuration, resulting

in improved source efficiency performance. In Section 6.4 we briefly examine the inferred ion streamlines compared to the nozzle field lines and show that the ions appear to exhibit outward separation. We posit that this arises from the transverse plasma potential and pressure gradients, and the decay in the magnetic field strength. In Section 6.5 we suggest design refinements that can be made to further improve performance. We summarize our results and discuss the ramifications of these findings in Section 6.6.

6.2 Results

In this section we present the plasma properties measurements required to estimate the thrust and component efficiency performance of the device. The source was operated in the 3.8 cm planar antenna configuration detailed in Chapter III. Refer to Figure 3.5 for a notional diagram of this configuration. These data were taken with the nozzle operating at $\sim$ 170 W combined deposited power into the transmission line and plasma source, 0.25 mg/s xenon propellant flow rate, and a peak magnetic field strength of 600 G.

6.2.1 Plume Properties

6.2.1.1 Plasma Properties

At this operating condition, we map plasma density, electron temperature, and plasma potential throughout the diverging nozzle section. It is clear from Figure 6.1a that the electron temperature decreases as the plasma expands through the nozzle. This indicates that the electron fluid is losing thermal energy during the expansion process, as expected of a nozzle. The electron temperature, and the associated cooling effect, is correlated with a reduction in the plasma potential as the plasma expands, as shown in Figure 6.1b. This potential structure in the diverging nozzle section gives

rise to an electrostatic acceleration of the ions. The plasma density map in Figure 6.1c provides additional evidence of expansion in the diverging nozzle section. In our test configuration, the highest density is observed at the source tube exit plane and decreases throughout the diverging nozzle section. This density trend is consistent with the expected decrease in the plasma pressure during the expansion process in the nozzle.

There are several interesting features present within these property maps. From the plasma density map in Figure 6.1c, the expanding plasma qualitatively follows the magnetic nozzle field lines more closely than in the operating conditions described in Chapters IV and V. This is a qualitative indication that the test article is operating differently, and is closer to the expansion behavior observed in moderate power magnetic nozzle thrusters. Note that there is an apparent decrease in the plasma density along the device centerline. This density depression region corresponds to the center hole of the planar antenna, which facilitates the propellant injection on device centerline through the backplane of the plasma liner. Due to this antenna geometry it is possible that significant power is not being deposited on centerline. This effect may be complemented by reduced cross-field diffusion within the plasma liner due to the high magnetic field strength, resulting in the observed density depression on centerline. We also measure lower electron temperatures on centerline, as shown in Figure 6.1a. This may also be a consequence of reduced power deposition and limited cross-field diffusion within the liner. Finally, in the plume near-field we observe a peak in the plasma potential along the device centerline, accompanied by a gradient that exhibits a large cross-field component. From an electrostatic perspective, the resulting electric field may lead to transverse ion motion. However, farther downstream the potential gradient rotates to become approximately colinear with the local magnetic field lines, as demonstrated by the locally near-perpendicular nature of the contour curves in that region of the plume. This suggests that the ions may be accelerated

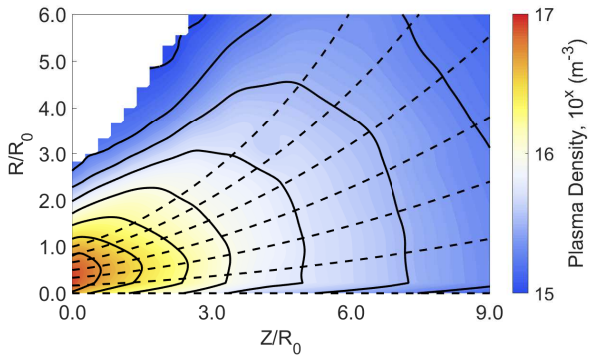

(a)

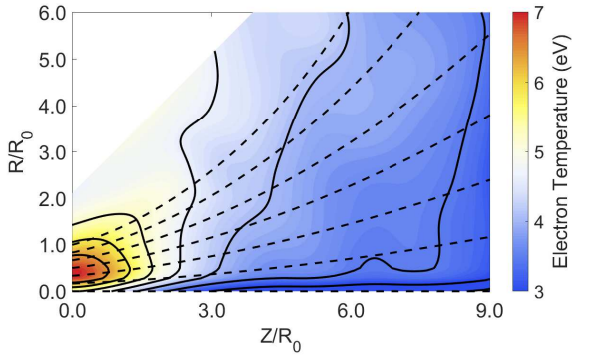

(b)

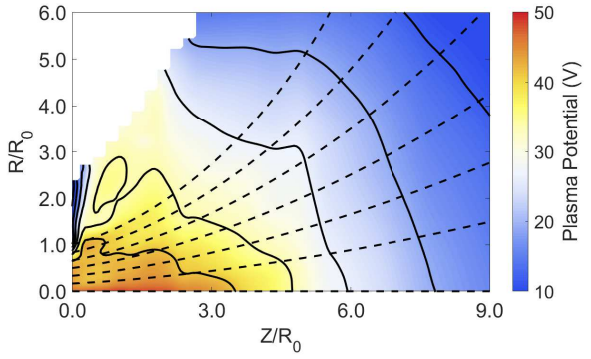

(c)

Figure 6.1: Spatial maps of the a) electron temperature, b) plasma potential, and c) plasma density (contours and solid curves) overlain with the magnetic nozzle field lines (dashed curves). The source was operated at 600 G, and $\sim$ 170 W net deposited power, and 0.25 mg/s of xenon.

along the field lines in that region of the nozzle.

6.2.1.2 Polytropic Cooling

The polytropic cooling index is required to calculate the power stored with electron heat conduction and the the local sound speed throughout the plume. To this end we use the spatial electron temperature and plasma potential maps in Figures 6.1a and 6.1b, and leverage the linear relationship between these two properties in polytropically expanding plasmas. As in Sections 4.2 and 5.3, we use linear regression fitting to estimate the polytropic cooling index and account for the error associated with the measurements. This linear regression fitting for for the test condition can be found in Figure 6.2. From this process the estimated polytropic index is $\gamma = 1.15 \pm 0.07$. This result is within the range of measured values for electric propulsion devices operating on xenon [99, 114, 204, 205], and between the adiabatic ($\gamma = 5/3$) and isothermal ($\gamma = 1$) limits.

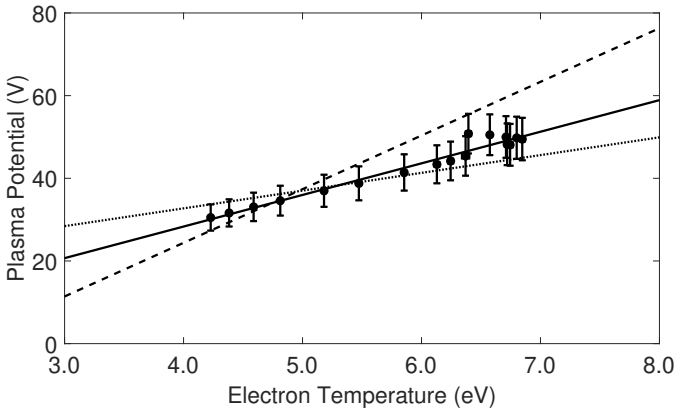

Figure 6.2: The polytropic index linear regression for the planar antenna configuration. The solid line is the best fit, while the dashed and dotted lines quantify the error. Note that the source was operated at 600 G, and $\sim$ 170 W net deposited power, and 0.25 mg/s of xenon.

6.2.1.3 Ion Acceleration

We also use a Faraday probe to spatially map the ion current density throughout the plume; the resulting current density profile map can be found in Figure 6.3a. Noting that the ion current density is a combination of the incident ion speed and the local plasma density ($j = qnu$), we can infer the ion speed by deconvolving these two terms. As in Sections 4.2 and 5.3, we assume that the ions are singly charged and use the plasma density map from Figure 6.1c. To examine the acceleration in the plume we normalize the ion speed by the local ion acoustic speed to yield the ion Mach number map found in Figure 6.3b. It is clear from these results the ions are supersonic immediately downstream of the nozzle throat. This suggests that our test article configuration successfully avoids the delayed onset of the ion sonic transition due to the neutral effects in the near-field plume. These ion Mach number results also confirm that the ions are being accelerated. While the ion acoustic speed decreases due to the electron cooling (near the throat $c_s \sim 2.4$ km/s, while in the far-field $c_s \sim 1.7$ km/s), this effect is insufficient to explain the far-field ion Mach number values — ion acceleration is required to achieve the far-field value of $M \sim 4.2$.

A detachment plane must be designated to calculate the thrust and efficiency of the test condition. As in Sections 4.2 and 5.3, we choose to define the detachment plane as the location at which the ions are no longer accelerated — where the ion speed is approximately constant. For our test article, the ion velocity plateaus at $(Z/R_0) \sim 7$, so we designate this as the detachment plane. Armed with this definition and the above spatial plasma maps, we can now estimate the device performance.

6.2.2 Performance

Using the performance framework in Chapter II and the above plasma measurements, we can estimate that various components of the device performance. Using Eq. 2.6 and assuming that the ambient pressure is negligible, the predicted thrust is

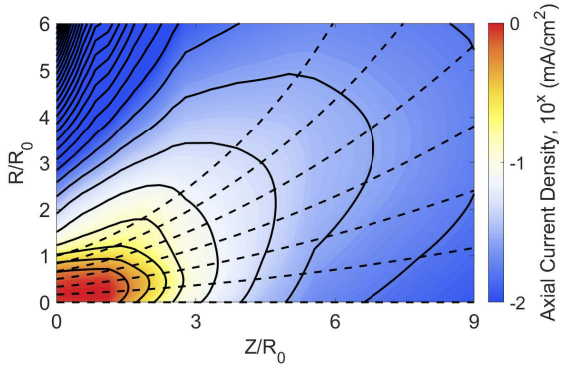

(a)

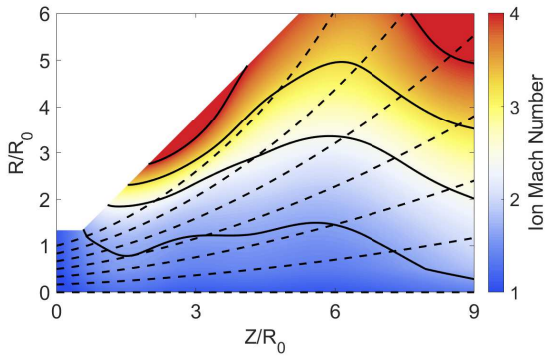

(b)

Figure 6.3: The a) axial ion current density and b) the ion Mach number spatial maps (contours and solid curves) overlain with the magnetic nozzle field lines (dashed curves). Note that the source was operated at 600 G, and $\sim$ 170 W net deposited power, and 0.25 mg/s of xenon.

330 ± 25 μN. Combining this thrust value with the propellant mass flow rate through Eq. 2.19 we calculate the specific impulse as 135 ± 10 seconds.

Turning to the component efficiency terms, we can calculate the mass utilization efficiency by combining the device geometry, the density and ion velocity measurements (to yield ion mass flow rate using Eq. 2.26), and Eq. 2.27. For the test condition the estimated mass utilization efficiency is 0.16 ± 0.02. Using the power deposition model in Section 2.4 and the plasma measurements at the throat we estimate that the source efficiency is 0.39 ± 0.03. By using the plasma measurements at the throat we can determine the power flowing into the diverging nozzle section using Eqs. 2.36 - 2.39. By combining this value, the estimated thrust, and the calculated ion mass flow rate and leveraging Eq. 2.34 we predict that the nozzle efficiency is 0.50 ± 0.04. We can estimate that the divergence efficiency is 0.54 ± 0.04 by combining the ion current density map with the Faraday probe analysis outlined in Section 3.3.5. The RF coupling efficiency is estimated to be 0.02 ± 0.005. This value combines the results from the power deposition model (Section 2.4) with the measured deposited power into the transmission lines and test article. Finally, the product of these efficiency terms indicate that the estimated total efficiency is $(0.03 \pm 0.01) \times 10^{-2}$. These performance results are summarized in Table 6.1.

For reference, other key parameters are included in Table 6.1. These parameters include the operating conditions, polytropic cooling index, ion acoustic speed at the throat, ion fraction, and CEX mean free path. The neutral density within the source tube is estimated assuming that the injected neutral propellant uniformly fills the plasma liner. This allows for the estimation of the ion fraction (0.03 ± 0.01) and CEX mean free path (10 ± 0.2 Z/R_0). The ion fraction, in particular is low. However, despite this low ion fraction, the CEX mean free path suggests that CEX collisions do not play a significant role in our device. This is further evidence that the test configuration overcomes the neutral effects described in Chapter IV.

Table 6.1: A summary of the performance parameters for the planar antenna configuration of the test article.

Parameter	Value
Magnetic Field (G)	600
Propellant Flow Rate (mg/s)	0.25
RF Power (W)	170
Ion Acoustic Speed (km/s)	2.4 ± 0.2
Polytropic Index	1.15 ± 0.07
Ion Fraction	0.03 ± 0.01
Charge Exchange Mean Free Path (λ_{CEX}/R_0)	10 ± 0.2
Thrust (μN)	330 ± 25
Specific Impulse (s)	135 ± 10
RF Coupling Efficiency	0.02 ± 0.005
Mass Utilization Efficiency	0.16 ± 0.02
Source Efficiency	0.39 ± 0.03
Nozzle Efficiency	0.50 ± 0.04
Divergence Efficiency	0.54 ± 0.04
Total Efficiency	$(0.03 \pm 0.01) \times 10^{-2}$

Three of the component efficiencies listed have been emphasized and directly impacted by neutral effects and non-uniform power deposition — the nozzle, source, and divergence efficiencies. The nozzle efficiency of the planar antenna test configuration shows significant improvement over the solenoidal antenna configuration used to study the neutral effects ($\eta_{noz} \sim 0.50$ for the planar antenna configuration compared to $\eta_{noz} < 0.1$ for the solenoidal antenna configuration). Due to the large CEX mean free path, this increase in nozzle efficiency may be explained by the absence of the ion-neutral collisional effects that impede ion acceleration. Similarly, the source efficiency term also exhibits a significant improvement ($\eta_{loss} \sim 0.39$ for the planar antenna configuration compared to $\eta_{loss} \sim 0.18$ for the highest magnetic field case in the solenoidal antenna configuration). This increase in source efficiency reflects the more uniform power deposition, and the subsequent reduction in radial wall losses, in the planar antenna configuration — this will be discussed further in the next section.

Finally, the estimated divergence efficiency of this test configuration is comparable to the measured divergence efficiency of the 400 G "ring discharge" configuration. Interestingly, the increased source radius of the planar antenna configuration results in a significant increase in the divergence of the vacuum interface nozzle line, but this appears to be balanced by the increased plasma density near the device centerline (as compared to the 400 G "ring discharge" case). Given the impact of increasing magnetic field strength on the divergence efficiency of the "ring discharge" configuration, it is reasonable to predict that the planar antenna configuration exhibits improved divergence efficiency performance at a peak field strength of 600 G. Noting that all of the test configurations are operated at the same input power, from these comparisons it appears that the planar antenna configuration exhibits an overall improvement in performance compared to the devices examined in Chapters IV and V.

6.3 Power Deposition

As in Section 5.4, we can quantitatively examine the power deposition uniformity using the multiple control volume analysis outlined in Section 2.4 and the measured plasma properties at the source exit plane. In contrast to the highly non-uniform power deposition in the solenoidal antenna configuration examined in Chapter V, this planar test condition exhibited relatively uniform power deposition, as shown in Figure 6.4. With the exception of near the centerline $R/R_0 \leq 0.3$, the fraction of total deposited power approximately constant ($P_{dep}/P_T \sim 7 \pm 2\%$) across the radius of the device. The centerline depression in the power deposition is correlated to the gas injection tube passing through the center of the planar spiral antenna on centerline — geometrically, the injection tube corresponds to $0 \leq R/R_0 \leq 0.2$. Depending on the antenna radiation pattern and its interaction with the DC magnetic field present within the source tube, the power deposition may be small on centerline. This can be confirmed with future work to fuse a model of the antenna-plasma coupling with

experimental measurements inside the source tube. Despite the lack of these measurements and an accompanying model, it is clear that this test configuration avoids the enhanced power deposition along the radial walls at an even higher magnetic field strength (600 G compared to the solenoidal antenna configuration with 400 G). This improvement gives rise to the improved in the source efficiency listed in Table 6.1.

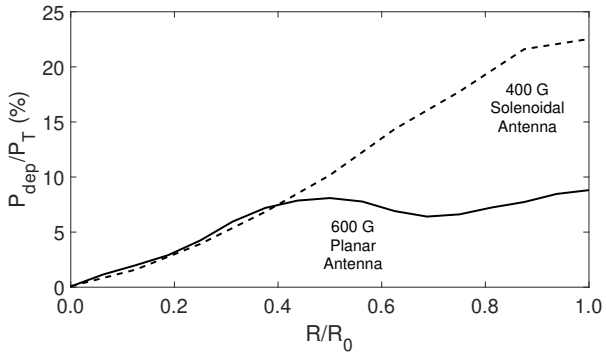

Figure 6.4: The estimated percentage of the total absorbed power as a function of radial position (solid curve). Note that the source was operated at 600 G, and ~ 170 W net deposited power, and 0.25 mg/s of xenon. For comparison, the estimated percentage of the total absorbed power as a function of radial position for the 400 G solenoidal antenna test configuration (refer to Chapter V is included (dashed curve).

6.4 Ion Detachment

For moderate power magnetic nozzles it has been found that device performance exhibits a strong dependence on the divergence efficiency; the minimization of ion radial momentum losses requires a collimated plume. Fundamentally, these divergence losses are linked to the detachment of the plasma exhaust from the diverging nozzle section. While the identification of the physical mechanisms underlying plasma detachment from magnetic field lines is an open topic of research [83, 84, 86, 96, 97, 98, 147, 149, 152, 167], there have been numerical models and results of experimental investigations reported in the literature. Numerical models have shown that under the correct conditions ions may separate from the nozzle inwards or outwards [84, 149] -

i.e. the ion streamlines diverge more slowly or rapidly than the magnetic field lines, respectively. Experimental investigations have also reported similar results. Using Mach probes to measure the 3D ion velocity vector, Terasaka et. al. demonstrated that the ion streamlines detached inwards [209]. A similar conclusion was reached by Deline et. al. [99] and Cox et. al. [210] by tracking the spatial evolution of the half-width, half-maximum of the radial density profile. This inward ion detachment was also observed by Olsen et. al. [101] through Faraday probe measurements when employing the secondary ion heating stage of VASIMR. More recently, using Faraday probes Little [83] observed this ion detachment behavior for high magnetic field operating conditions.

Conversely, outward ion detachment has also been reported in the literature. Olsen et. al. [101] reports that the ions detached outwards when the second stage ion heating was not used. Similarly, Little [83] measured outward separation for low magnetic field operating conditions. While these models and experiments provide insight into plasma detachment, the limited operating regimes and scope of the studies have not yet yielded a self-consistent description of this phenomenon and it underlying mechanisms.

Here, we would like to add another data set to the literature, albeit a small one. Using the techniques employed by Olsen et. al. [101] and Little [83], we can infer the ion streamlines for our test condition from Faraday probe measurements. Namely, we track the spatial evolution of various fractions of the total ion current - connecting the location of a given fraction of the ion current at discrete measurement planes throughout the plume yields an estimate of the ion streamline. These ion streamlines can be compared to the magnetic nozzle streamlines to qualitatively determine the type of ion detachment (inwards or outwards). First, the total ion current is calculated from the Faraday probe measurements at the source exit plane. We then track the spatial evolution of the $I/I_T = [0.10, 0.30, 0.50, 0.70, 0.85]$ current fractions, with the

results in the inferred ion streamlines shown in Figure 6.5.

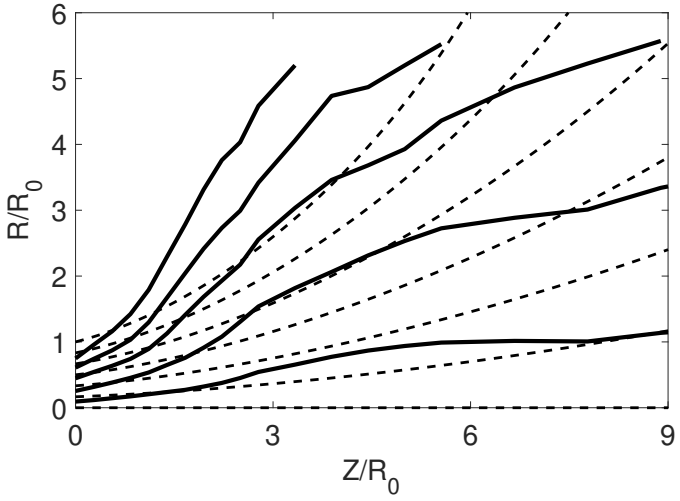

Figure 6.5: The inferred ion streamlines (solid curves) compared to the magnetic nozzle field lines (dashed curves). Note that the source was operated at 600 G, and $\sim$ 170 W net deposited power, and 0.25 mg/s of xenon.

These ion streamline results show several interesting characteristics. At the exit plane as the radius approaches the source radius the ion streamlines exhibit significant outward separation. This is contrasted by the ion streamlines near the centerline locally following the magnetic field lines. As the plasma expands in the region $Z/R_0 \leq 3$ all of the streamlines exhibit outward separation. This is followed by a decrease in the ion streamline divergence in the region of $3 \leq Z/R_0 \leq 6$ — all but the $I/I_T = 0.85$ streamline appear to deflect locally inwards. For $Z/R_0 \geq 6$ the ion streamlines approximately straighten. These ballistic trajectories, coupled with the plateauing of the ion speed at $Z/R_0 \sim 7$, suggest that the ions have detached from the magnetic magnetic nozzles. This indicates that our approximation of the detachment plane location through the proxy of ion speed may be valid.

From these results, the ion streamlines appear to exhibit net outward detachment. Interestingly, the ion streamline behavior appears to closely follow the electric field arising from the plasma potential gradients throughout the plume (refer to Figure 6.1c). This suggests that, for our low power test condition, the ion streamlines and

plume divergence can be predicted if the electric field can be accurately modeled. Due to our limited data set and the lack of measurement techniques that can directly interrogate the electron dynamics it is unclear what underlying mechanisms give rise to the electric field. However, this finding warrants further study examining a broader range of operating conditions in the low power regime to identify critical scaling parameters that may provide insight into these mechanisms.

6.5 Design Recommendations

While this test configuration has demonstrated a significant recovery of performance by mitigating neutral collisional and non-uniform power deposition effects, there is room for improvement. Upon examination of the device performance there are three clear areas to improve: the ion fraction, mass utilization efficiency, and RF power coupling efficiency. Fortunately, all three are linked. Due to the fact that the test article was not intended for flight testing, the design of the power matching circuit was not emphasized; available laboratory matching equipment intended for higher power operation was paired with a hand-made bare antenna. The low RF coupling efficiency ($\sim 2\%$) can be improved by designing a dedicated matching circuit and circuit-antenna interface that can minimize the transmission line lengths. Proper design could result in $\eta_{RF} \geq 50\%$. While power deposition has been demonstrated to be more complicated than can be described by a 0D global model, such models demonstrate that the first order effect of increasing power input into the plasma results in a plasma density increase. This resulting plasma density increase raises the ion fraction (recall that ion fraction is the ratio of the plasma density to neutral density). Additionally, assuming that an increase in the plasma density does not significantly alter the ion acceleration the mass utilization efficiency increases. So, these three underperforming parameters may be solved with a redesign of the power train.

While redesigning the power transmission circuitry should improve the device performance, the total efficiency is likely to remain low. Recall, from Figure 1.7 the maximum total efficiency depends on the electron temperature. For our device the electron temperature is ~ 7 eV. For this electron temperature, the nozzle efficiency, which is the basis for Figure 1.7, reaches the maximum expected value of $\sim 50\%$. This maximum arises from the frozen flow losses trapped within the ion production cost term (the cost to produce each ion is ~ 50 eV), due to the relatively low electron temperature. To achieve higher maximum performance, the electron temperature must be increased by and order of magnitude [83]. Unfortunately, for inductively-coupled plasma sources — a typical operating mode of a spiral planar antenna-driven device — the desired electron temperature increase ($T_e \geq 10$ eV) is not possible [165, 166, 211, 212, 213, 214, 215]. It is important to note that this performance curve assumes that the electrons are Maxwellian. In this context this assumption states that the energy of the bulk electron population dictates the plasma expansion physics. The low electron temperature capabilities of inductively-coupled devices suggests that a different power coupling scheme is required to achieve the desired electron temperatures. Recent developments in electron cyclotron resonance power coupling show promise, with electron temperatures exceeding 30 eV [114]. While our general findings — that efficient performance requires mitigating neutral collisional and non-uniform power deposition effects — hold regardless of power coupling mechanism, the presence of 3D electron resonance zones that provide the bulk of the heating in this device architecture suggests that an accurate, complicated power coupling model is a requisite tool to maximize efficiency.

6.6 Summary

In summary, the 2D plasma properties of an experimental low power magnetic nozzle plasma source designed to mitigate neutral collisional and non-uniform power

deposition effect by operating in a planar antenna configuration has been mapped using electrostatic probes. Qualitatively, the plasma measurements, particularly the plasma density, appear to follow the diverging magnetic nozzle field lines more closely than the test configurations described in Chapters IV and V. The thrust and efficiency performance of the test article is estimated by coupling the spatial plasma measurements with the theoretical framework described in Chapter II. The estimated performance demonstrates a significant recovery in performance, compared to these other configurations: the nozzle efficiency is ~ 0.50, the source efficiency is ~ 0.39, and the divergence efficiency is ~ 0.54. This is compared to $\eta_{noz} < 0.1$, $\eta_{loss} \sim 0.18$, and comparable divergence efficiency in the configurations described in the previous Chapters. In addition to this efficiency performance the predicted thrust is ~ 330 μN and the specific impulse is ~ 135 seconds. These estimated values are combined to yield an estimated total efficiency of $\sim 0.03 \times 10^{-2}$.

An analysis of power deposition within the source tube shows that the power is approximately uniformly deposited, except on the device centerline. This power deposition deficit is correlated with the location of the propellant injection on centerline through the backplane of the source tube. This improved power deposition uniformity reduces the plasma density at the radial wall, resulting in an increase in the source efficiency. The improvement in the nozzle efficiency is attributed to the avoidance of ion-neutral collisional effects — the charge exchange mean free path is ($\sim 10\ Z/R_0$) and the neutral density is an order of magnitude lower in the source tube in this configuration compared to the results in Section 4.2. This result is corroborated by measurements that indicate that the ions are sonic at the location of peak magnetic field, the nozzle throat. The combination of these results suggests that neutral collisional effects are successfully mitigated in this test configuration.

In addition to confirming that the test article does mitigate these effects, we are also able to infer the ion streamlines throughout the plume. It is found that these

streamlines diverge more quickly than the nozzle field lines, starting at $Z/R_0 \sim 1$. At $Z/R_0 \sim 7$ the ion trajectories appear to become ballistic. This corresponds to our chosen detachment plane, based on the criterion of a plateauing in the ion speed. The correlation of these two results suggest that the ion speed criterion can be used as a proxy to determine detachment for our device, in lieu of a self-consistent description of detachment.

The primary finding of this work is that the test configuration exhibited improved performance due to the mitigation performance degrading effects via an improved design. This finding highlights the importance of a comprehensive performance model that can capture the plasma expansion, neutral species, and power deposition physics to aid in the design process. As interest in low power magnetic nozzle thrusters continues to increase, it is critical that engineers have access to such a tool to quickly iterate in the design space to achieve efficient thrust production.

CHAPTER VII

Summary

In this dissertation, we have highlighted the major findings of our investigation into the performance of low power magnetic nozzle thrusters. These devices derive much of their heritage from their moderate power counterparts, which have an extensive body of literature that explores the physical plasma processes in magnetic nozzles and identifies key parameters that influence performance scaling [83, 84, 85, 86, 92, 94, 96, 97, 98, 147, 149, 152, 167]. Despite this body of research, less work has been done to confirm that low power devices conform to the performance models and exhibit the same dominant physical processes [40, 113, 114, 115, 116, 117, 118, 119, 151]. During our investigation into how low power operation differs from moderate power devices we focused on two primary questions:

1. *What underlying mechanisms adversely affect low power magnetic nozzle thrust performance?*

2. *Can these mechanisms explain the discrepancies between predicted and measured performance when using conventional moderate power magnetic nozzle models to evaluate low power devices?*

In the course of answering these questions we coupled a theoretical framework with experimental measurements to quantify the thrust and efficiency performance

and identify underlying physical mechanisms that influence low power magnetic nozzle operation. The major findings of our investigation are summarized in Section 7.1. We conclude the dissertation in Section 7.2 with a discussion of possible future research avenues.

7.1 Summary of Major Findings

In the development of our theoretical performance framework, we created a simple tool to that can be combined with experimental measurements to predict the thrust and various efficiency terms of the device. In particular, with knowledge of the plasma properties across the nozzle throat, the source, nozzle, and divergence efficiency terms can be predicted and compared to experimental measurements. We coupled this model with detailed plasma measurements of a versatile low power magnetic nozzle source to predict device performance and identify plasma mechanisms that reduce low power nozzle performance.

We used measurements of the plasma density, electron temperature, plasma potential, and ion velocity to confirm that the plasma cooling during expansion through the nozzle can be accurately described by a polytropic cooling law. The matching of our nozzle efficiency model predictions — which relies on the assumption of polytropic cooling — with experimental results, using the correct nozzle throat properties, further corroborated that the plasma cools polytropically. With this finding we showed that low power nozzles operate in a similar manner to their moderate power counterparts, in this way. The polytropic cooling of the electrons also suggested that electron heat conduction plays a role in the expansion process.

Using our low power test article, we investigated the how the presence of the neutral population in a low ion fraction device affects performance. We demonstrated that a quasi-1D model of the plume expansion processes does not accurately predict nozzle efficiency and thrust if the nozzle throat is assumed to be collocated at the location of

peak magnetic field strength. Using LIF and electrostatic probe measurements in a low ion fraction operating condition, we showed that the ion sonic transition location is pushed downstream, resulting in reduced performance. Upon relocating the throat plane to the experimentally determined ion sonic location we were able to match the model and experimental results for nozzle efficiency. This suggested that the quasi-1D expansion model was suitable for predicting performance if the nozzle throat was correctly assigned as the location where ions achieve sonic speed. We proceeded to correlate the delay in the ion acceleration to ion-neutral charge exchange collisions and ionization in the near-field plume. This correlation implied that the neutral density plays a significant role in the plasma expansion and overall device performance. Additionally, future low power magnetic nozzle thrusters must be designed to maximize the ion fraction, thereby mitigating these neutral-collisional effects, for efficient thrust production.

In a second configuration of our low power test article, we investigated the impact of power deposition uniformity on device efficiency performance. Using plasma density measurements at the device exit plane, we showed that the plasma density peak shifted radially outward as the magnetic field strength increased. We showed that this enhanced density at the radial wall resulted in degraded source and divergence efficiency. By splitting the source tube region into multiple control volumes we showed that the power deposited into the plasma was not radially uniform. The peak in the non-uniform power deposition was correlated with the peak in the measured plasma density profile. This was attributed to complex antenna-plasma coupling interactions that are dictated by the source geometry and operating conditions. Additionally, we showed that source efficiency improved with an increase in source tube aspect ratio, while the divergence efficiency decreased. This suggested that there is an optimal device geometry for efficient operation. From the combination of these two findings, it is apparent that power coupling must be accurately modeled and the appropriate

geometry design trades must be considered during early stages of the thruster design cycle to maximize performance.

Finally, in a third configuration of the test article, we showed that performance can be recovered by mitigating neutral-collisional and non-uniform power deposition effects. This device achieved improved performance through design choices, including the change from a solenoidal to a planar antenna to improve power deposition uniformity and ion fraction, and an increase in the source tube aspect ratio to reduce radial wall losses. Using detailed experimental measurements of the plasma density, electron temperature, plasma potential, and ion velocity we showed that this design successfully mitigated the neutral-collisional and power deposition effects. Overall, this finding demonstrates that, with an understanding of the the underlying physical mechanism that influence performance, thrusters can be designed around these low power effects to yield improved performance.

7.2 Recommendations for Future Work

Our investigation of low power magnetic nozzle operation has yielded new insights, but questions remain. The results in Chapter IV suggest that neutral propellant may play a significant role in the expansion physics and the overall device performance in the low power regime. However, models designed to predict the performance of moderate power devices often neglect the neutral species [84, 92, 94, 149, 152]. To highlight this gap, our model also did not self-consistently account for the neutral species. Rather, we relied on empirical findings to match the model results with our experimental measurements. The incorporation of the neutral species into future models would allow for comprehensive study of the physical mechanisms influenced by this species, and allow for an accurate prediction of the ion acceleration and device performance of low power magnetic nozzles. Such a model would also aid in the identification of operating conditions and thruster configurations conducive to

detrimental neutral-collisional effects, and indicate design changes that would improve performance through mitigation of these effects. This type of model could also allw designers to account for facility effects, where the ingestion of neutrals may significantly impact measured performance, and allow for the accurate prediction of in-space operations.

Based on our results in Chapters V and VI, showing that non-uniform power deposition and low overall RF coupling degrades efficiency performance, plasma-antenna coupling interactions constitute another avenue of research that merits attention. There is a large body of work that focuses on modeling plasma processing units, some of which are configured similarly to magnetic nozzle architectures [165, 166]. However, this body of work has not been leveraged within the magnetic nozzle propulsion community. The fusion of the existing magnetic nozzle expansion and plasma processing power coupling models may yield a self-consistent, comprehensive model of a magnetic nozzle thruster. This type of model would allow for the identification of additional plasma processes that play a critical role in determining thrust performance.

Throughout our work we have shown that the low electron temperature within our test article has resulted in large ionization losses. The low overall performance of moderate power magnetic nozzle thrusters has been attributed to these ionization losses [85, 92, 94, 152]. Given that ionization losses decrease with increasing electron temperature, research into plasma heating schemes that improve electron temperature would improve performance. One promising candidate is the ECR, with measured electron temperatures exceeding 30 eV [114]. Currently, there are several efforts to develop low power magnetic nozzle ECR thrusters [40, 113, 114, 115, 116, 117, 118, 119], but these devices have not yet demonstrated efficient thrust production. Additionally, these development efforts have relied on laboratory microwave power transmission technologies; it is unclear if comparable performance can be achieved with standalone devices packaged within SmallSat constraint. Given the promise of

these devices, further modeling of the power coupling and plasma expansion, and development of low power microwave power processing units may yet be fruitful.

Finally, when estimating the nozzle efficiency and thrust performance of our test configurations, we relied on the ion velocity measurements to predict the detachment location. A self-consistent description of detachment would eliminate the need for experimental measurements and yield further insight into the performance scaling of magnetic nozzles. The detachment problem is an ongoing area of study [83, 84, 86, 96, 97, 98, 147, 149, 152, 167], with a number of proposed theories. However, low power magnetic nozzle test devices, by virtue of their compact construction, provide a unique opportunity to experimentally characterize detachment across a range operating regimes. By pairing these compact designs with large vacuum test facilities — such as the 6 m by 9 m Large Vacuum Test Facility at the University of Michigan — these characterization experiments can be performed with enhanced confidence that facility effects play a negligible role. This combination of small test article and large facility would enable detailed non-invasive and electrostatic measurements of the plume near-field to the magnetic nozzle turning point to be made. These measurements can be coupled with the existing detachment theories [83, 84, 86, 96, 97, 98, 147, 149, 152, 167] to provide validation or identify additional dominant effects that must be incorporated into the model. Overall, the closure of the detachment problem would be a major step toward the creation of a self-consistent model that can accurately predict magnetic nozzle performance.

BIBLIOGRAPHY

[1] G. Richardson, K. Schmitt, M. Covert, and C. Rogers. Small satellite trends 2009-2013. 2015.

[2] F. G. Klotz. *Space, commerce, and national security*. Council on Foreign Relations New York, 1998.

[3] Federal Communications Commission. Fcc grants oneweb access to u.s. market for its proposed new broadband satellite constellation, 2017.

[4] Federal Communications Commission. Space exploration holdings, llc, application for approval for orbital deployment and operating authority for the spacex ngso satellite system, 2018.

[5] C. Norton, S. Pellegrino, and M. Johnson. Findings of the keck institute for space studies program on small satellites: A revolution in space science. 2013.

[6] D. Marmie, J.and Foreman, J. Hanson, V. Kuroda, S. Sawyer, E. Pencil, and T. Smith. Pathfinder technology demonstrator: Demonstrating novel cubesat technologies in low earth orbit. 2016.

[7] M. Swartwout. University-class satellites: From marginal utility to'disruptive'research platforms. 2004.

[8] K. Woellert, P. Ehrenfreund, A. J. Ricco, and H. Hertzfeld. Cubesats: Cost-effective science and technology platforms for emerging and developing nations. *Advances in Space Research*, 47(4):663–684, 2011.

[9] J. Mueller, J. Ziemer, R. Hofer, R. Wirz, and T. ODonnell. A survey of micro-thrust propulsion options for microspacecraft and formation flying missions. In *5th Annual CubeSat Developers Workshop San Luis Obispo, CA*, 2008.

[10] M. Tsay, J. Frongillo, K. Hohman, and B. K. Malphrus. Lunarcube: A deep space 6u cubesat with mission enabling ion propulsion technology. 2015.

[11] D. Folta, D. Dichmann, P. Clark, A. Haapala, and K. Howell. Lunar cube transfer trajectory options. In *25th AAS/AIAA Space Flight Mechanics Meeting*.

[12] P. Clark, B. Malphrus, D. Reuter, R. MacDowall, D. Folta, T. Hurford, C. Brambora, and W. Farrell. Lunar ice cube: Birches payload and the search for volatiles with a first generation deep space cubesat. 2016.

[13] M. Dearborn, B. Isch, T. Johnson, A. MacDonald, E. Peek, C. Lomanno, C. Sheffield, and E. Swenson. Falconsat-7a deployable solar telescope. 2014.

[14] M. Iuzzolino, D. Accardo, G. Rufino, E. Oliva, and A. Tozzi. Multi-band sensor for exoplanet detection to be installed onboard cubesat. 2016.

[15] A. Klesh and J. Krajewski. Marco: Cubesats to mars in 2016. 2015.

[16] W. Blackwell, G. Allen, C. Galbraith, T. Hancock, R. Leslie, I. Osaretin, L. Retherford, M. Scarito, C. Semisch, and M. Shields. Nanosatellites for earth environmental monitoring: The micromas project. In *Geoscience and Remote Sensing Symposium (IGARSS), 2012 IEEE International*, pages 206–209. IEEE, 2012.

[17] H. Carreno-Luengo, A. Camps, P. Via, J. F. Munoz, A. Cortiella, D. Vidal, J. Jane, N. Catarino, M. Hagenfeldt, P. Palomo, and S. Cornara. 3cat-2 - an experimental nanosatellite for gnss-r earth observation: Mission concept and analysis. *IEEE Journal of Selected Topics in Applied Earth Observations and Remote Sensing*, PP(99):1–12, 2016.

[18] D. Selva and D. Krejci. A survey and assessment of the capabilities of cubesats for earth observation. *Acta Astronautica*, 74:50–68, 2012.

[19] R. M. Robinson and T. Moretto. Small satellites for space weather research. *Space Weather*, 6(5), 2008.

[20] S. C. Reising, T. C. Gaier, C. D. Kummerow, V. Chandrasekar, S. T. Brown, S. Padmanabhan, B. H. Lim, S. C. van den Heever, T. S. L'Ecuyer, and C. S. Ruf. Overview of temporal experiment for storms and tropical systems (tempest) cubesat constellation mission. In *Microwave Symposium (IMS), 2015 IEEE MTT-S International*, pages 1–4. IEEE, 2015.

[21] F. Pranajaya, R. Zee, S. Grocott, T. Rodic, D. Matko, K. Otir, M. Peljhan, A. Urbas, H. Frhlich, and S. Blaic. Nemo-hd: high-resolution microsatellite for earth monitoring and observation. 2012.

[22] P. Platzer, C. Wake, and L. Gould. Smaller satellites, smarter forecasts: Gps-ro goes mainstream. 2015.

[23] S. Padmanabhan, S. Brown, P. Kangaslahti, R. Cofield, D. Russell, R. Stachnik, J. Steinkraus, and B. Lim. A 6u cubesat constellation for atmospheric temperature and humidity sounding. 2013.

[24] T. Moretto. Cubesat mission to investigate ionospheric irregularities. *Space Weather*, 6(11), 2008.

[25] D. Klumpar, L. Springer, E. Mosleh, K. Mashburn, S. Berardinelli, A. Gunderson, M. Handley, N. Ryhajlo, H. Spence, and S. Smith. Flight system technologies enabling the twin-cubesat firebird-ii scientific mission. 2015.

[26] N. A. Miller, R. B. Norman, H. L. Soto, V. A. Stewart, M. L. Jones, M. C. Kowalski, A. B. Shabat, K. M. Gough, R. L. Stavely, and A. C. Shim. The rapid response radiation survey (r3s) mission using the hisat conformal satellite architecture. 2015.

[27] T. Hiramatsu, S. Yamaura, H. Akiyama, N. Sato, K. Morita, T. Otani, K. Miyata, T. Kouyama, S. Kato, and M. Ito. Early results of a wildfire monitoring microsatellite uniform-1. 2015.

[28] W. Holemans, R. G. Moore, and J. Kang. Counting down to the launch of popacs (polar orbiting passive atmospheric calibration spheres). 2012.

[29] V. Hernandez, P. Gankidi, A. Chandra, A. Miller, P. Scowen, H. Barnaby, E. Adamson, E. Asphaug, and J. Thangavelautham. Swimsat: Space weather and meteor impact monitoring using a low-cost 6u cubesat. 2016.

[30] S. Stirone. The real cost of nasa missions. *Popular Science*, 2015.

[31] L. Dyrud, S. Slagowski, J. Fentzke, W. Wiscombe, B. Gunter, K. Cahoy, G. Bust, A. Rogers, B. Erlandson, and L. Paxton. Small-sat science constellations: Why and how. 2013.

[32] N. J. Boll. *Small Satellites: Applications in Resiliency and Redundancy*, page 5304. 2016.

[33] C. Kitts and M. Rasay. A university-based distributed satellite mission control network for operating professional space missions. *Acta Astronautica*, 2015.

[34] M. W. Smith, D. W. Miller, and S. Seager. Enhancing undergraduate education in aerospace engineering and planetary sciences at mit through the development of a cubesat mission. In *SPIE Optical Engineering+ Applications*, pages 81460S–81460S–12. International Society for Optics and Photonics, 2011.

[35] G. Bonin, N. Roth, S. Armitage, J. Newman, B. Risi, and R. E. Zee. Canx4 and canx5 precision formation flight: Mission accomplished! 2015.

[36] J. Bouwmeester and J. Guo. Survey of worldwide pico-and nanosatellite missions, distributions and subsystem technology. *Acta Astronautica*, 67(7):854–862, 2010.

[37] M. U. Siddiqui, C. Cretel, J. Synowiec, A. G. Hsu, J. A. Young, and R. Specktor. First performance measurements of the phase four rf thruster. *Proc. 35th IEPC (Atlanta, USA, 2017), IEPC-2017-431*, 2017.

[38] M. U. Siddiqui and C. Cretel. *Updated Performance Measurements and Analysis of the Phase Four RF Thruster*. AIAA Propulsion and Energy Forum. American Institute of Aeronautics and Astronautics, 2018. doi:10.2514/6.2018-4817.

[39] T. A. Collard and J. P. Sheehan. *Preliminary Measurements of an Integrated Prototype of the CubeSat Ambipolar Thruster*. AIAA Propulsion and Energy Forum. American Institute of Aeronautics and Astronautics, 2016. doi:10.2514/6.2016-5042.

[40] T. Vialis, J. Jarrige, and D. Packan. Geometry optimization and effect of gas propellant in an electron cyclotron resonance plasma thruster. *Proc. 35th IEPC (Atlanta, USA, 2017), IEPC-2017-378*, 2017.

[41] J. Ziemer. Performance of electrospray thrusters. *Proc. 31st IEPC (Ann Arbor, MI, USA, 2009), IEPC-2009-242*, 2009.

[42] D. Courtney, S. Dandavino, and H. Shea. *Performance and Applications of Ionic Electrospray Micro-Propulsion Prototypes*. AIAA SPACE Forum. American Institute of Aeronautics and Astronautics, 2015. doi:10.2514/6.2015-4672.

[43] C. Marrese-Reading. *Microfluidic Electrospray Propulsion(MEP) Thruster Performance with Microfabricated Emitter Arrays for Indium Propellant*. AIAA Propulsion and Energy Forum. American Institute of Aeronautics and Astronautics, 2016. doi:10.2514/6.2016-4738.

[44] A. Cervone, B. Zandbergen, D. C. Guerrieri, M. De Athayde Costa e Silva, I. Krusharev, and H. van Zeijl. Green micro-resistojet research at delft university of technology: new options for cubesat propulsion. *CEAS Space Journal*, pages 1–15, 2016.

[45] S. Ciaralli, M. Coletti, and S. B. Gabriel. Performance and lifetime testing of a pulsed plasma thruster for cubesat applications. *Aerospace Science and Technology*, 2015.

[46] M. Coletti, S. Ciaralli, and S. B. Gabriel. Ppt development for nanosatellite applications: Experimental results. *Plasma Science, IEEE Transactions on*, 43 (1):218–225, 2015.

[47] M. Coletti, F. Guarducci, and S. B. Gabriel. A micro ppt for cubesat application: Design and preliminary experimental results. *Acta Astronautica*, 69(3): 200–208, 2011.

[48] A. Dinardi and M. Persson. High performance green propulsion (hpgp): a flight-proven capability and cost game-changer for small and secondary satellites, 2012.

[49] V. Hruby. High isp cubesat propulsion. In *Interplanetary Cubesat Conference*, 2012.

[50] T. K. Imken, T. H. Stevenson, and E. G. Lightsey. Design and testing of a cold gas thruster for an interplanetary cubesat mission. 2015.

[51] V. J. Lappas, T. Harle, A. Knoll, P. Shaw, P. Bianco, and M. Perren. Micro electric propulsion technology for small satellites: Design, testing and in-orbit operations. 2013.

[52] R. K. Masse, R. A. Spores, M. Allen, S. Kimbrel, and C. McLean. Enabling high performance green propulsion for smallsats. 2015.

[53] C. Scharlemann, M. Tajmar, I. Vasiljevich, N. Buldrini, D. Krejci, and B. Seifert. Propulsion for nanosatellites. In *The 32nd International Electric Propulsion Conference*, pages 11–15, 2011.

[54] M. Tsay, J. Frongillo, D. Lafko, and J. Zwahlen. Development status and 1u cubesat application of buseks 0.5 n green monopropellant thruster. 2014.

[55] M. Tsay, D. Lafko, J. Zwahlen, and W. Costa. Development of busek 0.5 n green monopropellant thruster. 2013.

[56] D. Williams. Propulsion solutions for cubesats and applications. In *CubeSat Developers Workshop, Logan, UT*, 2012.

[57] K. Zondervan, J. Fuller, D. Rowen, B. Hardy, C. Kobel, S. Chen, P. Morrison, T. Smith, and A. Kremer. Cubesat solid rocket motor propulsion systems providing delta-vs greater than 500 m/s. In *Small Satellite Conference*.

[58] F. Trezzolani, A. L. Fabris, D. Pavarin, A. Selmo, and M. Manente. Low power radio-frequency plasma thruster development and testing. In *33rd International Electric Propulsion Conference*.

[59] D. Spence, E. Ehrbar, N. Rosenblad, N. Demmons, T. Roy, S. Hoffman, D. Williams, V. Hruby, and C. Tocci. Electrospray propulsion systems for small satellites. In *Small Satellite Conference*.

[60] J. P. Sheehan, T. A. Collard, B. W. Longmier, and I. Reese. *New Low-Power Plasma Thruster for Nanosatellites*. Propulsion and Energy Forum. American Institute of Aeronautics and Astronautics, 2014. doi:10.2514/6.2014-3914.

[61] A. Shashurin and T. Keidar, M.and Zhuang. Comparative analysis of micro-cathode arc thruster performance. In *33rd International Electric Propulsion Conference*.

[62] D. T. Schmuland, C. Carpenter, and R. K. Masse. Mission applications of the mrs-142 cubesat high-impulse adaptable monopropellant propulsion system (champs). *AIAA Paper*, (2012-4269), 2012.

[63] D. Schmuland, R. Masse, and C. Sota. Hydrazine propulsion module for cube-sats. In *Small Satellite Conference*.

[64] M. S. Rhee, C. M. Zakrzwski, and M. A. Thomas. Highlights of nanosatellite propulsion development program at nasa-goddard space flight center. In *Small Satellite Conference*.

[65] D. Platt. A monopropellant milli-newton thruster system for attitude control of nanosatellites. In *Small Satellite Conference*.

[66] D. Morris and R. Noble. Cubesat advanced technology propulsion system concept. In *Small Satellite Conference*.

[67] F. Martel, L. Perna, and P. Lozano. Miniature ion electrospray thrusters and performance test on cubesats. In *Small Satellite Conference*.

[68] I. Kronhaus, K. Schilling, S. Jayakumar, A. Kramer, M. Pietzka, and J. Schein. Design of the uwe-4 picosatellite orbit control system using vacuum-arc-thrusters. In *Proceedings of the 33rd International Electric Propulsion Conference*, pages 2013–195.

[69] A. D. Ketsdever, R. H. Lee, and T. C. Lilly. Performance testing of a microfabricated propulsion system for nanosatellite applications. *Journal of Micromechanics and Microengineering*, 15(12):2254, 2005.

[70] M. Keidar, S. Haque, T. Zhuang, A. Shashurin, D. Chiu, G. Teel, E. Agasid, O. Tintore, and E. Uribe. Micro-cathode arc thruster for phonesat propulsion. In *Small Satellite Conference*.

[71] S. Fuchikami, M. Nakamoto, K. Toyoda, and M. Cho. Development of vacuum arc thruster for nano-satellite. In *33rd International Electric Propulsion Conference, Washington DC, USA*, 2013.

[72] J. Dyer, A. Dinardi, and K. Anflo. First implementation of high performance green propulsion in a constellation of small satellites. In *Small Satellite Conference*.

[73] A. Bertino-Reibstein and A. Wuerl. Development of a warm-gas butane system for microsatellite propulsion. In *Small Satellite Conference*, 2013.

[74] A. Tummala and A. Dutta. An overview of cube-satellite propulsion technologies and trends. *Aerospace*, 4(4):58, 2017.

[75] J. P. Sheehan, T. A. Collard, M. E. Ostermann, E. T. Dale, B. N. Wachs, and B. W. Longmier. Initial operation of the cubesat ambipolar thruster. In *Plasma Sciences (ICOPS), 2015 IEEE International Conference on*, pages 1–1. IEEE, 2015.

[76] K. Takahashi, T. Lafleur, C. Charles, P. Alexander, R. W. Boswell, M. Perren, R. Laine, S. Pottinger, V. Lappas, and T. Harle. Direct thrust measurement of a permanent magnet helicon double layer thruster. *Applied Physics Letters*, 98 (14):141503, 2011.

[77] K. Takahashi, C. Charles, R. W. Boswell, and A. Ando. Performance improvement of a permanent magnet helicon plasma thruster. *Journal of Physics D: Applied Physics*, 46(35):352001, 2013.

[78] C. Charles and R. W. Boswell. Laboratory evidence of a supersonic ion beam generated by a current-free helicon double-layer. *Physics of Plasmas (1994-present)*, 11(4):1706–1714, 2004.

[79] C. Charles and R. W. Boswell. Current-free double-layer formation in a high-density helicon discharge. *Applied Physics Letters*, 82:1356, 2003.

[80] L. T. Williams and M. L. R. Walker. Thrust measurements of a radio frequency plasma source. *Journal of Propulsion and Power*, 29(3):520–527, 2013.

[81] L. T. Williams and M. L. R. Walker. Plume structure and ion acceleration of a helicon plasma source. *Plasma Science, IEEE Transactions on*, 43(5): 1694–1705, 2015.

[82] L. T. Williams and M. L. R. Walker. Thrust measurements of a helicon plasma source. In *AIAA/ASME/SAE/ASEE Joint Propulsion Conference & Exhibit*, 2011.

[83] J. M. Little. *Performance Scaling of Magnetic Nozzles for Electric Propulsion*. PhD thesis, Princeton University, 2015.

[84] M. Merino and E. Ahedo. Plasma detachment in a propulsive magnetic nozzle via ion demagnetization. *Plasma Sources Science and Technology*, 23(3):032001, 2014.

[85] A. Fruchtman, K. Takahashi, C. Charles, and R. W. Boswell. A magnetic nozzle calculation of the force on a plasma. *Physics of Plasmas (1994-present)*, 19(3): 033507, 2012.

[86] E. Ahedo and M. Merino. On plasma detachment in propulsive magnetic nozzles. *Physics of Plasmas (1994-present)*, 18(5):053504, 2011.

[87] B. W. Longmier, J. P. Squire, L. D. Cassady, M. G. Ballenger, M. D. Carter, C. Olsen, A. V. Ilin, T. W. Glover, G. E. McCaskill, and F. R. C. Diaz. Vasimr vx-200 performance measurements and helicon throttle tables using argon and krypton. In *32nd International Electric Propulsion Conference*, 2011.

[88] K. Takahashi, H. Akahoshi, C. Charles, R. W. Boswell, and A. Ando. High temperature electrons exhausted from rf plasma sources along a magnetic nozzle. *Physics of Plasmas*, 24(8):084503, 2017.

[89] P. G. Hill and C. R. Peterson. *Mechanics and thermodynamics of propulsion (2nd revised and enlarged edition)*. 1992.

[90] I. G. Mikellides, I. Katz, Richard R. Hofer, and D. M. Goebel. Magnetic shielding of walls from the unmagnetized ion beam in a hall thruster. *Applied Physics Letters*, 102(2):023509, 2013.

[91] R. R. Hofer, D. M. Goebel, I. G. Mikellides, and I. Katz. Magnetic shielding of a laboratory hall thruster. ii. experiments. *Journal of Applied Physics*, 115(4): 043304, 2014.

[92] E. Ahedo and J. Navarro-Cavall. Helicon thruster plasma modeling: Two-dimensional fluid-dynamics and propulsive performances. *Physics of Plasmas (1994-present)*, 20(4):043512, 2013.

[93] G. R. Seikel. Generation of Thrust-Electromagnetic Thrustors. In *Electric Propulsion for Spacecraft*, volume 22 of *NASA Special Publication*, page 19, December 1962.

[94] T. Lafleur. Helicon plasma thruster discharge model. *Physics of Plasmas*, 21 (4):043507, 2014.

[95] T. Lafleur, K. Takahashi, C. Charles, and R. W. Boswell. Direct thrust measurements and modelling of a radio-frequency expanding plasma thruster. *Physics of Plasmas*, 18(8):080701, 2011.

[96] A. V. Arefiev and B. N. Breizman. Magnetohydrodynamic scenario of plasma detachment in a magnetic nozzle. *Physics of Plasmas (1994-present)*, 12(4): 043504, 2005.

[97] R. W. Moses, R. A. Gerwin, and K. F. Schoenberg. Resistive plasma detachment in nozzle based coaxial thrusters. *AIP Conference Proceedings*, 246(1):1293–1303, 1992.

[98] E. B. Hooper. Plasma detachment from a magnetic nozzle. *Journal of Propulsion and Power*, 9(5):757–763, 1993.

[99] C. A. Deline, R. D. Bengtson, B. N. Breizman, M. R. Tushentsov, J. E. Jones, D. G. Chavers, C. C. Dobson, and B. M. Schuettpelz. Plume detachment from a magnetic nozzle. *Physics of Plasmas (1994-present)*, 16(3):033502, 2009.

[100] B. N. Breizman, M. R. Tushentsov, and A. V. Arefiev. Magnetic nozzle and plasma detachment model for a steady-state flowa). *Physics of Plasmas (1994-present)*, 15(5):057103, 2008.

[101] C. S. Olsen, M. G. Ballenger, M. D. Carter, F. R. C. Diaz, M. Giambusso, T. W. Glover, A. V. Ilin, J. P. Squire, B. W. Longmier, and E. A. Bering. Investigation of plasma detachment from a magnetic nozzle in the plume of the vx-200 magnetoplasma thruster. *IEEE Transactions on Plasma Science*, 43(1): 252–268, 2015.

[102] M. Martinez-Sanchez and J. E. Pollard. Spacecraft electric propulsion-an overview. *Journal of Propulsion and Power*, 14(5):688–699, 1998.

[103] P. Grondein, T. Lafleur, P. Chabert, and A. Aanesland. Global model of an iodine gridded plasma thruster. *Physics of Plasmas (1994-present)*, 23(3):033514, 2016.

[104] J. Szabo, B. Pote, S. Paintal, M. Robin, A. Hillier, R. D. Branam, and R. E. Huffmann. Performance evaluation of an iodine-vapor hall thruster. *Journal of Propulsion and Power*, 28(4):848–857, 2012.

[105] J. Szabo, M. Robin, S. Paintal, B. Pote, V. Hruby, and C. Freeman. Iodine propellant space propulsion. In *Proceedings of the 33rd International Electric Propulsion Conference*, pages 2013–311, 2013.

[106] K. A. Polzin and S. Peeples. Iodine hall thruster propellant feed system for a cubesat. In *50th Joint Propulsion Conference, Cleveland, OH*, 2014.

[107] O. S. Tverdokhlebov and A. V. Semenkin. Iodine propellant for electric propulsionto be or not to be. 2001.

[108] G. W. Bethke and D. B. Miller. Cyclotron resonance thruster design techniques. *AIAA Journal*, 4(5):835–840, 1966.

[109] E. F. Gibbons and D. B. Miller. Experiments with an electron cyclotron resonance plasma accelerator. *AIAA Journal*, 2(1):35–41, 1964.

[110] H. Hendel and T. Reboul. *CONTINUOUS PLASMA ACCELERATION AT ELECTRON CYCLOTRON RESONANCE*. International Electric Propulsion Conference. American Institute of Aeronautics and Astronautics, 1963. doi:10.2514/6.1963-1.

[111] H. G. Kosmahl, D. B. Miller, and G. W. Bethke. Plasma acceleration with microwaves near cyclotron resonance. *Journal of Applied Physics*, 38(12):4576–4582, 1967.

[112] J. C. Sercel. *An experimental and theoretical study of the ECR plasma engine*. PhD thesis, 1993.

[113] S. Correyero, J. Jarrige, D. Packan, and E. Ahedo. Ion acceleration in the magnetic nozzle of an ecr thruster: Comparison of experimental measurements with a quasi 1d kinetic model. In *2018 Space Propulsion Conference*, 2018.

[114] T. Lafleur, F. Cannat, J. Jarrige, P. Q. Elias, and D. Packan. Electron dynamics and ion acceleration in expanding-plasma thrusters. *Plasma Sources Science and Technology*, 24(6):065013, 2015.

[115] J. Jarrige, P. Q. Elias, and D. Cannat, F.and Packan. Performance comparison of an ecr plasma thruster using argon and xenon as propellant gas. In *Proceedings of the 33rd International Electric Propulsion Conference*, pages 2013–420, 2013.

[116] J. Jarrige, S. Correyero-Plaza, P. Q. Elias, and D. Packan. Investigation on the ion velocity distribution in the magnetic nozzle of an ecr plasma thruster using lif measurements. Technical report, IEPC-2017-382, 2017.

[117] K. Diamant, T. Albright, B. Zeigler, and W. Cox. *Miniature Cyclotron Resonance Thruster*. Joint Propulsion Conferences. American Institute of Aeronautics and Astronautics, 2011. doi:10.2514/6.2011-5882.

[118] B. Wachs and B. Jorns. *Effect of Background Pressure on Ion Dynamics in an Electron Cyclotron Resonance Thruster*. AIAA Propulsion and Energy Forum. American Institute of Aeronautics and Astronautics, 2018. doi:10.2514/6.2018-4585.

[119] S. T. Hepner, B. N. Wachs, T. A. Collard, and B. A. Jorns. Observation of low frequency plasma oscillations in the plume of a partially magnetized magnetic nozzle. In *54th AIAA/SAE/ASEE Joint Propulsion Conference*, AIAA Propulsion and Energy Forum. American Institute of Aeronautics and Astronautics, 2018.

[120] R. G. Jahn. *Physics of Electric Propulsion*. 1968.

[121] R. W. Boswell. Very efficient plasma generation by whistler waves near the lower hybrid frequency. *Plasma Physics and Controlled Fusion*, 26(10):1147, 1984.

[122] M. A. Lieberman and A. J. Lichtenberg. Principles of plasma discharges and materials processing. *MRS Bulletin*, 30:899–901, 1994.

[123] M. Light and F. F. Chen. Helicon wave excitation with helical antennas. *Physics of Plasmas (1994-present)*, 2(4):1084–1093, 1995.

[124] David G. Miljak and F. F. Chen. Helicon wave excitation with rotating antenna fields. *Plasma Sources Science and Technology*, 7(1):61, 1998.

[125] Y. Stratakos, A. Zeniou, and E. Gogolides. Comparison of helical and helicon antennas as sources of plasma excitation using a full wave 3d electromagnetic analysis in vacuum. *Plasma Processes and Polymers*, 2016.

[126] Y. Stratakos, A. Zeniou, and E. Gogolides. Electromagnetic simulation of helicon plasma antennas for their electrostatic shield design. *Journal of Vacuum Science & Technology A*, 34(3):031307, 2016.

[127] J. E. Stevens, M. J. Sowa, and J. L. Cecchi. Helicon plasma source excited by a flat spiral coil. *Journal of Vacuum Science & Technology A*, 13(5):2476–2482, 1995.

[128] F. F. Chen. Experiments on helicon plasma sources. *Journal of Vacuum Science & Technology A*, 10(4):1389–1401, 1992.

[129] O. V. Batishchev. Minihelicon plasma thruster. *IEEE Transactions on Plasma Science*, 37(8):1563–1571, 2009.

[130] L. T. Williams. *Ion acceleration mechanisms of helicon thrusters*. PhD thesis, 2013.

[131] T. Matsuoka, I. Funaki, T. Nakamura, K. Yokoi, H. Nishida, T. S. Rudenko, K. P. Shamrai, T. Tanikawa, T. Hada, and S. Shinohara. Scaling laws of lissajous acceleration for electrodeless helicon plasma thruster. *Plasma and Fusion Research*, 6:2406103–2406103, 2011.

[132] C. Charles, R. W. Boswell, and M. A. Lieberman. Xenon ion beam characterization in a helicon double layer thruster. *Applied physics letters*, 89(26): 261503–261900, 2006.

[133] F. N. Gesto, B. D. Blackwell, C. Charles, and R. W. Boswell. Ion detachment in the helicon double-layer thruster exhaust beam. *Journal of propulsion and power*, 22(1):24–30, 2006.

[134] M. D. West, C. Charles, and R. W. Boswell. High density mode in xenon produced by a helicon double layer thruster. *Journal of Physics D: Applied Physics*, 42(24):245201, 2009.

[135] K. D. Diamant, J. E. Pollard, M. W. Crofton, M. J. Patterson, and G. C. Soulas. Thrust stand characterization of the nasa evolutionary xenon thruster. *Journal of Propulsion and Power*, 27(4):777–785, 2011.

[136] K. G. Xu and M. L. R. Walker. High-power, null-type, inverted pendulum thrust stand. *Review of Scientific Instruments*, 80(5):055103, 2009.

[137] J. E. Polk, A. Pancotti, T. Haag, S. King, M. Walker, J. Blakely, and J. Ziemer. Recommended practice for thrust measurement in electric propulsion testing. *Journal of Propulsion and Power*, pages 1–17, 2017.

[138] S. Pottinger, V. Lappas, C. Charles, and R. W. Boswell. Performance characterization of a helicon double layer thruster using direct thrust measurements. *Journal of Physics D: Applied Physics*, 44(23):235201, 2011.

[139] T. Harle, S. J. Pottinger, and V. J. Lappas. Helicon double layer thruster operation in a low magnetic field mode. *Plasma Sources Science and Technology*, 22(1):015015, 2012.

[140] A. Shabshelowitz and A. D. Gallimore. Performance and probe measurements of a radio-frequency plasma thruster. *Journal of Propulsion and Power*, 29(4): 919–929, 2013.

[141] K. Takahashi, C. Charles, R. Boswell, and A. Ando. Effect of magnetic and physical nozzles on plasma thruster performance. *Plasma Sources Science and Technology*, 23(4):044004, 2014.

[142] K. Takahashi, C. Charles, and R. W. Boswell. Approaching the theoretical limit of diamagnetic-induced momentum in a rapidly diverging magnetic nozzle. *Phys. Rev. Lett.*, 110:195003, May 2013. doi: 10.1103/PhysRevLett.110.195003. URL `https://link.aps.org/doi/10.1103/PhysRevLett.110.195003`.

[143] K. D. Diamant, R. Liang, and R. L. Corey. *The Effect of Background Pressure on SPT-100 Hall Thruster Performance*. AIAA Propulsion and Energy Forum. American Institute of Aeronautics and Astronautics, 2014. doi:10.2514/6.2014-3710.

[144] M. L. R. Walker. *Effects of facility backpressure on the performance and plume of a Hall thruster*. University of Michigan, 2005.

[145] A. Fruchtman. Electric field in a double layer and the imparted momentum. *Phys. Rev. Lett.*, 96:065002, Feb 2006. doi: 10.1103/PhysRevLett.96.065002. URL `https://link.aps.org/doi/10.1103/PhysRevLett.96.065002`.

[146] A. Fruchtman. The thrust of a collisional-plasma source. *IEEE Transactions on Plasma Science*, 39(1):530–539, 2011.

[147] E. Ahedo and M. Merino. Two-dimensional supersonic plasma acceleration in a magnetic nozzle. *Physics of Plasmas (1994-present)*, 17(7):073501, 2010.

[148] M. Merino and E. Ahedo. Influence of electron and ion thermodynamics on the magnetic nozzle plasma expansion. *IEEE Transactions on Plasma Science*, 43 (1):244–251, 2015.

[149] E. Ahedo and M. Merino. Two-dimensional plasma expansion in a magnetic nozzle: Separation due to electron inertia. *Physics of Plasmas*, 19(8):083501, 2012.

[150] T. A. Collard, J. P. Sheehan, and B. A. Jorns. *A Numerical Examination of the Performance of Small Magnetic Nozzle Thrusters*. AIAA Propulsion and Energy Forum. American Institute of Aeronautics and Astronautics, 2017. doi:10.2514/6.2017-4721.

[151] T. A. Collard, M. P. Byrne, S. T. Hepner, C. J. Durot, and B. A. Jorns. Investigation of detachment in a miniature magnetic nozzle source. In *35th International Electric Propulsion Conference, Atlanta, GA*, 2017.

[152] J. M. Little and E. Y. Choueiri. Thrust and efficiency model for electron-driven magnetic nozzles. *Physics of Plasmas (1994-present)*, 20(10):103501, 2013.

[153] Gordon C. Oates. *Aerothermodynamics of Gas Turbine and Rocket Propulsion*. AIAA Education Series. American Institute of Aeronautics and Astronautics, 1997. doi:10.2514/4.861345.

[154] D. M Goebel and I. Katz. *Fundamentals of electric propulsion: ion and Hall thrusters*, volume 1. John Wiley & Sons, 2008.

[155] D. L. Brown, C. W. Larson, B. E. Beal, and A. D. Gallimore. Methodology and historical perspective of a hall thruster efficiency analysis. *Journal of Propulsion and Power*, 25(6):1163–1177, 2009.

[156] S. A. Andersen, V. O. Jensen, P. Nielsen, and N. D'Angelo. Continuous supersonic plasma wind tunnel. *The Physics of Fluids*, 12(3):557–560, 1969.

[157] F. Gustrau. *RF and microwave engineering: fundamentals of wireless communications*. John Wiley & Sons, 2012.

[158] R. Sorrentino and G. Bianchi. *Microwave and RF engineering*, volume 1. John Wiley & Sons, 2010.

[159] K. Takahashi, D. Sato, K. Takaki, and A. Ando. Development of a compact magnetically expanding plasma source with a strong magnetic field. *Plasma Sources Science and Technology*, 22(5):055002, 2013.

[160] K. Takahashi, T. Lafleur, C. Charles, P. Alexander, and R. W. Boswell. Electron diamagnetic effect on axial force in an expanding plasma: Experiments and theory. *Phys. Rev. Lett.*, 107: 235001, Nov 2011. doi: 10.1103/PhysRevLett.107.235001. URL `https://link.aps.org/doi/10.1103/PhysRevLett.107.235001`.

[161] K. Takahashi, A. Chiba, A. Komuro, and A. Ando. Experimental identification of an azimuthal current in a magnetic nozzle of a radiofrequency plasma thruster. *Plasma Sources Science and Technology*, 25(5):055011, 2016.

[162] K. Takahashi and A. Ando. Enhancement of axial momentum lost to the radial wall by the upstream magnetic field in a helicon source. *Plasma Physics and Controlled Fusion*, 59(5):054007, 2017.

[163] J. M. Little and E. Y. Choueiri. Critical condition for plasma confinement in the source of a magnetic nozzle flow. *IEEE Transactions on Plasma Science*, 43(1):277–286, 2015.

[164] J. M. Little and E. Y. Choueiri. Electron cooling in a magnetically expanding plasma. *Physical Review Letters*, 117(22):225003, 2016. PRL.

[165] R. L. Kinder and M. J. Kushner. Wave propagation and power deposition in magnetically enhanced inductively coupled and helicon plasma sources. *Journal of Vacuum Science & Technology A: Vacuum, Surfaces, and Films*, 19(1):76–86, 2001.

[166] R. L. Kinder and M. J. Kushner. Noncollisional heating and electron energy distributions in magnetically enhanced inductively coupled and helicon plasma sources. *Journal of Applied Physics*, 90(8):3699–3712, 2001.

[167] S. A. Cohen and M. A. Paluszek. The grand challenge- a new plasma thruster. *Launchspace*, 3(6):46, 1998.

[168] J. M. Haas. *Low-perturbation interrogation of the internal and near-field plasma structure of a Hall thruster using a high-speed probe positioning system.* PhD thesis, 2001.

[169] J. F. Waymouth. Perturbation of a plasma by a probe. Technical report, DTIC Document, 1962.

[170] J. C. Simpson, J. E. Lane, C. D. Immer, and R. C. Youngquist. Simple analytic expressions for the magnetic field of a circular current loop. 2001.

[171] T. A. Collard and B. A. Jorns. The impact of non-idealities on low power magnetic nozzle thrust performance. In *54th AIAA/SAE/ASEE Joint Propulsion Conference*, AIAA Propulsion and Energy Forum. American Institute of Aeronautics and Astronautics, 2018.

[172] J. E. Foster and E. D. Gillman. A magnetically enhanced inductive discharge chamber for electric propulsion applications. *IEEE Transactions on Plasma Science*, 36(5):2130–2140, Oct 2008. ISSN 0093-3813. doi: 10.1109/TPS.2008.2001975.

[173] A. R. Ellingboe and R. W. Boswell. Capacitive, inductive and helicon-wave modes of operation of a helicon plasma source. *Physics of Plasmas (1994-present)*, 3(7):2797–2804, 1996.

[174] C. M. Franck, O. Grulke, and T. Klinger. Mode transitions in helicon discharges. *Physics of Plasmas (1994-present)*, 10(1):323–325, 2003.

[175] C. M. Franck, O. Grulke, A. Stark, T. Klinger, E. E. Scime, and G. Bonhomme. Measurements of spatial structures of different discharge modes in a helicon source. *Plasma Sources Science and Technology*, 14(2):226, 2005.

[176] I. D. Sudit and F. F. Chen. Discharge equilibrium of a helicon plasma. *Plasma Sources Science and Technology*, 5(1):43, 1996.

[177] R. Piejak, V. Godyak, and B. Alexandrovich. The electric field and current density in a low-pressure inductive discharge measured with different b-dot probes. *Journal of Applied Physics*, 81(8):3416–3421, 1997.

[178] J. Hopwood. Review of inductively coupled plasmas for plasma processing. *Plasma Sources Science and Technology*, 1(2):109, 1992.

[179] F. F. Chen. Langmuir probe analysis for high density plasmas. *Physics of Plasmas (1994-present)*, 8(6):3029–3041, 2001.

[180] F. F. Chen. Langmuir probe diagnostics. In *IEEE-ICOPS Meeting, Jeju, Korea*, 2003.

[181] I. D. Sudit and F. F. Chen. Rf compensated probes for high-density discharges. *Plasma Sources Science and Technology*, 3(2):162, 1994.

[182] V. A. Godyak, R. B. Piejak, and B. M. Alexandrovich. Probe diagnostics of non-maxwellian plasmas. *Journal of Applied Physics*, 73(8):3657–3663, 1993.

[183] V. A. Godyak, R. B. Piejak, and B. M. Alexandrovich. Measurement of electron energy distribution in low-pressure rf discharges. *Plasma sources science and technology*, 1(1):36, 1992.

[184] V. A. Godyak and V. I. Demidov. Probe measurements of electron-energy distributions in plasmas: what can we measure and how can we achieve reliable results? *Journal of Physics D: Applied Physics*, 44(23):233001, 2011.

[185] A. P. Paranjpe, J. P. McVittie, and S. A. Self. A tuned langmuir probe for measurements in rf glow discharges. *Journal of Applied Physics*, 67(11):6718–6727, 1990.

[186] B. A. Smith and L. J. Overzet. Improvements to the floating double probe for time-resolved measurements in pulsed rf plasmas. *Review of Scientific Instruments*, 69(3):1372–1377, 1998.

[187] F. F. Chen. Double-probe method for unstable plasmas. *Review of Scientific Instruments*, 35(9):1208–1212, 1964.

[188] E. Leveroni and E. Pfender. Electric probe diagnostics in thermal plasmas: Double probe theory and experimental results. *Review of Scientific Instruments*, 60(12):3744–3749, 1989.

[189] R. M. Castro, G. A. Cirino, P. Verdonck, H. S. Maciel, M. Massi, M. B. Pisani, and R. D. Mansano. A comparative study of single and double langmuir probe techniques for rf plasma characterization. *Contributions to Plasma Physics*, 39 (3):235–246, 1999.

[190] B. M. Oliver, R. M. Clements, and P. R. Smy. Radio-frequency floating double probe as a plasma diagnostic. *Journal of Applied Physics*, 41(5):2117–2122, 1970.

[191] M. Tuszewski and J. A. Tobin. The accuracy of langmuir probe ion density measurements in low-frequency rf discharges. *Plasma Sources Science and Technology*, 5(4):640, 1996.

[192] A. Brockhaus, C. Borchardt, and J. Engemann. Langmuir probe measurements in commercial plasma plants. *Plasma Sources Science and Technology*, 3(4): 539, 1994.

[193] J. D. Swift, M. J. R. Schwar, and John H. Keller. Electrical probes for plasma diagnostics. *Journal of The Electrochemical Society*, 118(3):94C, 1971.

[194] H. Amemiya. Measuring methods of plasma parameters by a differentiating and modulating double probe. *Japanese Journal of Applied Physics*, 27(Part 1, No. 4):694–695, 1988.

[195] J. P. Sheehan and N. Hershkowitz. Emissive probes. *Plasma Sources Science and Technology*, 20(6):063001, 2011.

[196] J. P. Sheehan, Y. Raitses, N. Hershkowitz, and M. McDonald. Recommended practice for use of emissive probes in electric propulsion testing. *Journal of Propulsion and Power*, pages 1–24, 2016.

[197] D. L. Brown, M. L. R. Walker, J. Szabo, W. Huang, and J. E. Foster. Recommended practice for use of faraday probes in electric propulsion testing. *Journal of Propulsion and Power*, 2016.

[198] I. H. Hutchinson. Principles of plasma diagnostics: Second edition. *Plasma Physics and Controlled Fusion*, 44(12):2603–2603, 2002.

[199] B. Jorns, C. A. Dodson, J. R. Anderson, D. M. Goebel, R. R. Hofer, M. J. Sekerak, A. Lopez Ortega, and I. G. Mikellides. *Mechanisms for Pole Piece Erosion in a 6-kW Magnetically-Shielded Hall Thruster*. AIAA Propulsion and Energy Forum. American Institute of Aeronautics and Astronautics, 2016. doi:10.2514/6.2016-4839.

[200] W. Huang, A. D. Gallimore, and R. R. Hofer. Neutral flow evolution in a six-kilowatt hall thruster. *Journal of Propulsion and Power*, 27(3):553–563, 2011.

[201] R. Bamford, K. J. Gibson, A. J. Thornton, J. Bradford, R. Bingham, L. Gargate, L. O. Silva, R. A. Fonseca, M. Hapgood, C. Norberg, T. Todd, and R. Stamper. The interaction of a flowing plasma with a dipole magnetic field: measurements and modelling of a diamagnetic cavity relevant to spacecraft protection. *Plasma Physics and Controlled Fusion*, 50(12):124025, 2008.

[202] H. Y. W. Tsui, A. J. Wootton, J. D. Bell, R. D. Bengston, D. Diebold, J. H. Harris, N. Hershkowitz, C. Hidalgo, J. C. Ingraham, S. J. Kilpatrick, G. X. Li, H. Lin, D. M. Manos, M. A. Meier, G. M. Miller, C. P. Munson, J. Pew, S. C. Prager, Ch P. Ritz, A. Rudyj, K. F. Schoenberg, J. Sorensen, T. Tanaka, T. Uckan, and P. G. Weber. A comparison of edge turbulence in tokamaks, stellarators, and reversed-field pinches*. *Physics of Fluids B: Plasma Physics*, 5(7):2491–2497, 1993.

[203] V. Antoni, D. Desideri, E. Martines, G. Serianni, and L. Tramontin. Plasma potential well and velocity shear layer at the edge of reversed field pinch plasmas. *Physical Review Letters*, 79(24):4814–4817, 1997. PRL.

[204] K. Dannenmayer and Mazouffre. S. Electron flow properties in the far-field plume of a hall thruster. *Plasma Sources Science and Technology*, 22(3):035004, 2013.

[205] Z. Zhang, H. Tang, M. Kong, Z. Zhang, and J. Ren. Electron temperature measurement in maxwellian non-isothermal beam plasma of an ion thruster. *Review of Scientific Instruments*, 86(2):023506, 2015.

[206] B. Wachs. Background pressure effects on ion dynamics on a low-power magnetic nozzle thruster. *Plasma Sources Science and Technology*, In Preparation, 2019.

[207] E. B. Saloman. Energy levels and observed spectral lines of xenon, xei through xeliv. *Journal of Physical and Chemical Reference Data*, 33(3):765–921, 2004.

[208] H. U. Eckert. Diffusion theory of the electrodeless ring discharge. *Journal of Applied Physics*, 33(9):2780–2788, 1962.

[209] K. Terasaka, S. Yoshimura, K. Ogiwara, M. Aramaki, and M. Y. Tanaka. Experimental studies on ion acceleration and stream line detachment in a diverging magnetic field. *Physics of Plasmas*, 17(7):072106, 2010.

[210] W. Cox, C. Charles, R. W. Boswell, and R. Hawkins. Spatial retarding field energy analyzer measurements downstream of a helicon double layer plasma. *Applied Physics Letters*, 93(7):071505, 2008.

[211] S. Ashida and M. A. Lieberman. Spatially averaged (global) model of time modulated high density chlorine plasmas. *Japanese Journal of Applied Physics*, 36(Part 1, No. 2):854–861, 1997.

[212] D. McCarren and E. Scime. Parametric scaling of neutral and ion excited state densities in an argon helicon source. *Plasma Sources Science and Technology*, 25(2):025001, 2016.

[213] F. F. Chen. Langmuir probe measurements in the intense rf field of a helicon discharge. *Plasma Sources Science and Technology*, 21(5):055013, 2012.

[214] C. Charles, R. Boswell, and K. Takahashi. Boltzmann expansion in a radiofrequency conical helicon thruster operating in xenon and argon. *Applied Physics Letters*, 102(22):223510, 2013.

[215] P. E. Masherov, V. A. Riaby, and V. A. Godyak. Integral electrical characteristics and local plasma parameters of a rf ion thruster. *Review of Scientific Instruments*, 87(2):02B926, 2016.